Missouri S&T Library and Learning Resources

Scholars' Mine

Doctoral Dissertations | Student Theses and Dissertations

Spring 2017

Acquisition of active multichannel analysis of surface waves (MASW) data in karst terrain

Ghassan Salem Alsulaimani

Follow this and additional works at: https://scholarsmine.mst.edu/doctoral_dissertations

 Part of the Geological Engineering Commons, and the Geophysics and Seismology Commons

Department: Geosciences and Geological and Petroleum Engineering

Recommended Citation

Alsulaimani, Ghassan Salem, "Acquisition of active multichannel analysis of surface waves (MASW) data in karst terrain" (2017). *Doctoral Dissertations*. 2735.
https://scholarsmine.mst.edu/doctoral_dissertations/2735

This thesis is brought to you by Scholars' Mine, a service of the Missouri S&T Library and Learning Resources. This work is protected by U. S. Copyright Law. Unauthorized use including reproduction for redistribution requires the permission of the copyright holder. For more information, please contact scholarsmine@mst.edu.

ACQUISITION OF ACTIVE MULTICHANNEL ANALYSIS OF SURFACE WAVES (MASW) DATA IN KARST TERRAIN

by

GHASSAN SALEM ALSULAIMANI

A DISSERTATION

Presented to the Faculty of the Graduate School of the

MISSOURI UNIVERSITY OF SCIENCE AND TECHNOLOGY

In Partial Fulfilment of the Requirements for the Degree

DOCTOR OF PHILOSOPHY

in

GEOLOGICAL ENGINEERING

2017

Approved by

Neil L. Anderson, Advisor
J. David Rogers
Kelly Liu
Stephen S. Gao
Jeffery D. Cawlfield

© 2017

Ghassan Salem Alsulaimani

All Rights Reserved

ABSTRACT

This study was designed to verify the effects and data reproducibility when the length of receiver array, receiver spacing, source offset and array orientation parameters are changed for data acquired using multichannel analysis of surface waves (MASW), at intended target depth of 30ft (9m), and to compare the results with electrical resistivity tomography (ERT) data obtained for the same study site.

The MASW data acquired for 34 sites, along four profiles for each site using variable source offsets of 10ft (3m) and 30ft (9.1m), and variable receiver spacings of 2.5ft (0.76m) and 5.0ft (0.76m), concurrently. Out of the 272 profiles studied, 136 profiles were oriented east-west, and 136 profiles were oriented north-south. The MASW data was used in conjunction with ERT data to ensure the accuracy of the ERT data.

The comparative analysis indicated the profile configuration measurements have significant influence on the quality of the data and that the best inversion analysis is obtained when the dispersion curves are created using the north-south oriented arrays.

The MASW survey study concluded that the most consistent and beneficial karst terrain dispersion images were those obtained from the predicted optimal acquisition, using receiver spacing (dx) = 2.5ft, source offset (X_1) =10ft and depth of investigation of about 30ft.

ACKNOWLEDGEMENTS

First of all, I dedicate everything to God Almighty, who made all things possible.

I sincerely extend my gratefulness to my advisor, Dr. Neil L. Anderson, for the guidance he provided as well as the understanding and patience. Through his mentorship, I have availed with a well-grounded experience with the consistency of my research objectives. He further provided me with encouragement not only to broaden my experimentalist approach, but also to harness my independent thought. The overwhelming contributions of my committee members, including Dr. J. David Rogers, Dr. Kelly H. Liu, Dr. Stephen S. Gao and Dr. Jeffery D. Cawlfield, are also greatly thanked for their generous support.

I would like to thank the Minister of Energy and Industry and Mineral Resources, Saudi Arabia, Mr. Khalid Al-Falih. I thank the Saudi Geological Survey President, Dr. Zohair Nawab, for his support as well.

I would like to extend my gratitude and eternal thanks to my father Salem, my mother Amnah, my sisters, and my brothers for instilling in me the ability to pursue my ambitions with their love and encouragement. I am also exceedingly grateful to my father-in-law, Khalid and mother-in-law, Hayat for their support and prayer.

This work is dedicated to my loving wife, Kholood. Without your love and sacrifice, I would not be achieving this milestone and encouragement throughout the whole period of my study, and also to my beloved kids, Salem and Juwan.

Finally, special thanks go to the efforts of Mr. Rafat Ghandoura and Dr. Adel Kerry. Without them, I would not have been able to complete the project successfully.

TABLE OF CONTENTS

Page

LIST OF ILLUSTRATIONS

Page

LIST OF TABLES

Page

1. INTRODUCTION

1.1. OVERVIEW

Subsurface imaging is very critical to study subsurface in complex karst terrain. Application of non-destructive geophysical methods is one of the effective ways to evaluate the subsurface conditions. A number of geophysical methods are currently used to imaging subsurface in karst terrain, including Electrical Resistivity Tomography (ERT), Self-potential (SP), Induced Polarization (IP), Ground Penetrating Radar (GPR), Seismic Refraction, Seismic Reflection, and Multichannel Analysis of Surface Waves (MASW).

The active Multichannel Analysis of Surface Waves (MASW) technique is typically used to generate 1-D shear-wave velocity profiles that extend to depths of approximately 100ft. (30.5m). The use of optimal acquisition parameters is vital to assuring the generation of the most accurate 1-D shear-wave velocity profiles. The identification of optimal acquisition parameters can be a challenging task, especially in complex karst terrain, because the acoustic properties of the subsurface can vary due to the complex and irregular nature of the bedrock surface, the presence of solution-widened joints, etc. In this research, four configurations are tested in order to develop optimum acquisition parameters to achieve better data resolution and the minimum investigation depth of 30ft. (9m).

1.2. RESEARCH OBJECTIVES

The primary objective of the study is to develop optimum MASW array configuration that can be used to image the subsurface in complex karst terrain. There is

an expectation that the use of optimum MASW array configuration will allow to image to a depth of 30ft., while providing a good data quality. The following are means to accomplish this objective:

- Acquire active MASW data along a 16 ERT traverses and using different array configurations,
- Evaluate quality of MASW data on the basis of overtone images,
- Process and interpret MASW and ERT data using bore hole data,
- Compare the MASW and ERT data interpretations in terms of estimating top of bedrock,
- Perform a statistical data analysis in order to develop an optimum MASW array configuration.

1.3. STRUCTURE OF THE DISSERTATION

Sections one contains an introduction to the dissertation. The main objective and significance of the research are discussed in this chapter. A critical review and analysis of the relevant literature is also provided.

Section two discusses geology of southwest Missouri, overview of geological and stratigraphic succession of Mississippian system, formation of karst features, overview of sinkhole formation process and karst in topography in Missouri and geophysical investigation in karst terrain.

Section three provides overviews of two geophysical methods – MASW and ERT. Basic concepts, data acquisition, data processing and data interpretation are discussed for each of the method.

Section four presents the experiments conducted in this research. The description of the study site is also provided in this chapter.

Section five contains comparative analysis of the data. Discussions with focus on the optimum MASW array configuration are presented in this chapter.

Section six provides the conclusions of the research.

Section seven summarizes recommendations for further studies.

The references that have been used during the study are listed at the end of the dissertation.

1.4. LITERATURE REVIEW

Geophysical exploration methods, such as Electrical Resistivity Tomography (ERT) and Multichannel Analysis of Surface Waves (MASW), have been used to study a wide range of targets within the ground from discovering the deep structure of the subsurface at thousands of meters to near surface structures and their properties at depths of a few tens of meters (Elkrry et al., 2015). These methods have been employed in various applications in engineering geology (Miller et al., 1999a, 1999b; Torgashov and Varnavina, 2016; Park et al., 1998, 1999b, 2000; Xia et al., 1998, 1999, 2000a, 2000b).

The MASW and ERT methods have different applications in geotechnical investigations. Each technique has its own advantages and drawbacks. To increase the accuracy of geophysical investigation, the combination of methods can be effectively used to constrain and verify the interpretations, especially for geophysical data collected in complex karst terrain environment. Although karst terrain is often manifested at the

subsurface, it is difficult to determine that without more detailed subsurface investigations.

The ERT method is used to estimate lateral and vertical variations in ground resistivity values and can be used to map geologic variations. It has been used for multiple geotechnical projects, including the imaging of the spatial distribution of moisture in pavement sections (Buettner et al., 1999), river terrace sand and gravel deposit reserve characterization and estimation using 3-D ERT arrays for bedrock surface detection (Chambers et al., 2013), imaging of the subsurface in karst terrain (Torgashov, 2012), and characterization of soils using ERT and geotechnical investigations (Sudha, 2009).

The MASW method is used to evaluate the shear-wave velocity distribution and arrangement of overburden soil deposits and the bedrock as well. A considerable amount of research has been published regarding the use of both geophysical methods in complex terrain environment (Doolittle et al., 1998; Kidanu et al., 2016; Miller et al., 2005; Thierry et al., 2005; He et al., 2006; Schrott and Sass, 2008). Since the method was introduced into the geophysical community in late 90s, it has been extensively used for various applications and researched for its data acquisition and processing strategies (Park et al., 1999). As noted by Park (2013), shear-wave velocity is a proper indicator of material stiffness, but for a specific rock types, such as carbonate rocks, shear-wave velocity is affected by its porosity and pore structure, as noted by Baechle et al., 2009. Shear-wave velocity can be used to differentiate various types of unconsolidated soils and bedrock (Odum et al., 2007), as typically bedrock exhibits higher velocities than soil, fractured rock, or karst terrain. Recent studies have shown that the instrumental

configurations used for field data acquisition and processing can affect the dispersion results obtained from surface wave seismic surveys. Attempts to obtain accurate or more efficient dispersion curves were established by selection of particular acquisition parameters and careful processing. The optimum parameters of MASW data acquisition, including the optimum distance between the source and receiver spread (source offset) and geophone array length, were discussed by Park, Miller, & Miura (2002), Park and Carnevale (2010), and by Anderson (2012). (Xu et al., 2006) demonstrated the possibility to develop optimum field parameters for particular MASW survey if preliminary information on the phase velocity range and interface depth is available. A successful attempt to develop a formula for quantitative evaluation of a layered homogeneous elastic model estimation using specific offset was performed by (Xu et al., 2006). Attempted to develop acquisition and processing parameters for MASW using 3-D ERT as control. In environmental studies, the MASW method was employed to generate 2-D shear-wave velocity fields calculated from inversion of Rayleigh-wave phase velocities, define top-of-rock and subsurface geological structures from 6 to 100 ft. (1.8 to 30 m) (Xia et al., 1998; Miller et al., 1999), and to determine a collapse feature in an extremely noisy environment (Xia et al., 2004a).

1.5. SIGNIFICANCE OF THE RESEARCH

The proposed study is not only significant for imaging in karst terrain in southwest Missouri, but it also has a broader impact on the social and economic lives of people at all areas. Some of the significant aspects of this research include:

- Developing optimum MASW data acquisition and processing parameters to enhance overall data quality and increase investigation depth.
- Verifying the efficiency of using integrated geophysical tools (MASW, ERT, and bore hole) to map complex subsurface systems in karts terrain.
- Improving reliability of geophysical data interpretation in complex karst terrain.
- Detecting probabilities for catastrophic collapse, and therefore, minimizing pollution and contamination of aquifers.

2. GEOLOGY OF SOUTHWEST MISSOURI

2.1. INTRODUCTION

Much of the Missouri state is underlain by carbonate rock (Fig. 2.1.), and most of it is exposed (Vandike, 1997). Karst-related features are formed in dolomite and limestone bedrocks in Missouri. The presence of clay and mud and shale with low permeability curbs downward movement of surface water and slows the advancement of solution cavities in the underlying carbonate rock. Hence, fewer sinkholes and caves are found in Northern Missouri compared to Southern and Central Missouri.

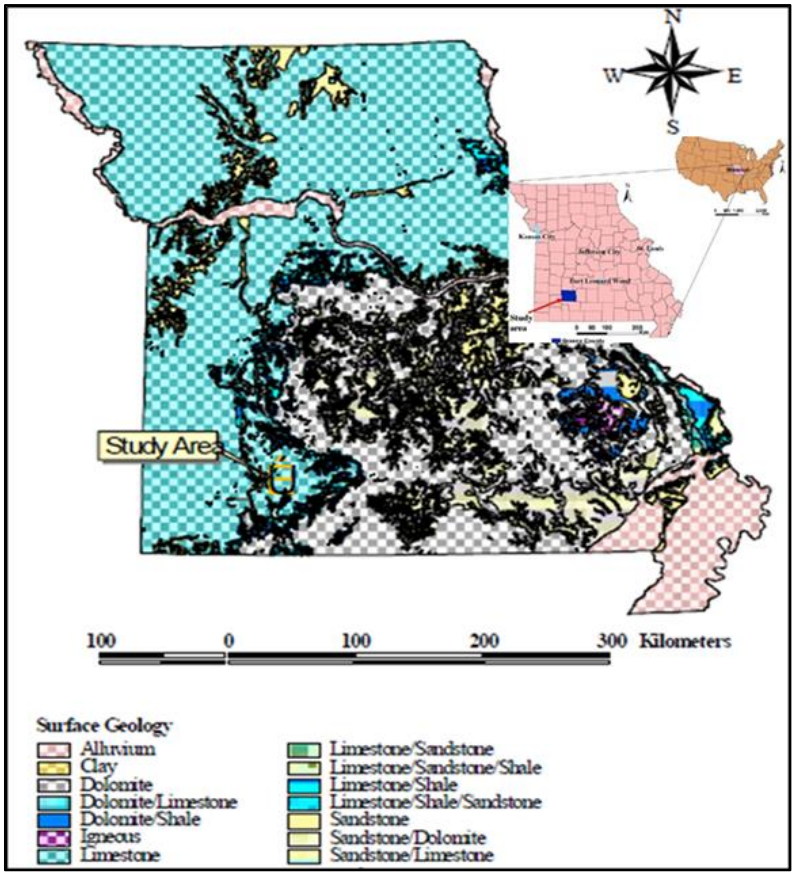

Figure 2.1. Surface Geology of Missouri (MSDIS, 2003). http://oewri.missouristate.edu/assets/OEWRI/KShade-Thesis.pdf.

2.2. OVERVIEW OF GEOLOGICAL AND STRATIGRAPHIC SUCCESSION OF MISSISSIPPIAN SYSTEM IN SOUTHWEST MISSOURI

The stratigraphic succession of rock units in the Mississippian System is not uniform throughout Missouri. Because of that, Missouri is divided into six zones: northwestern, east-central, southeastern, central, southwestern, and northwestern. Figure 2.2 highlights that southwest Missouri is located in the southwestern region to facilitate a description of Mississippian Age rocks.

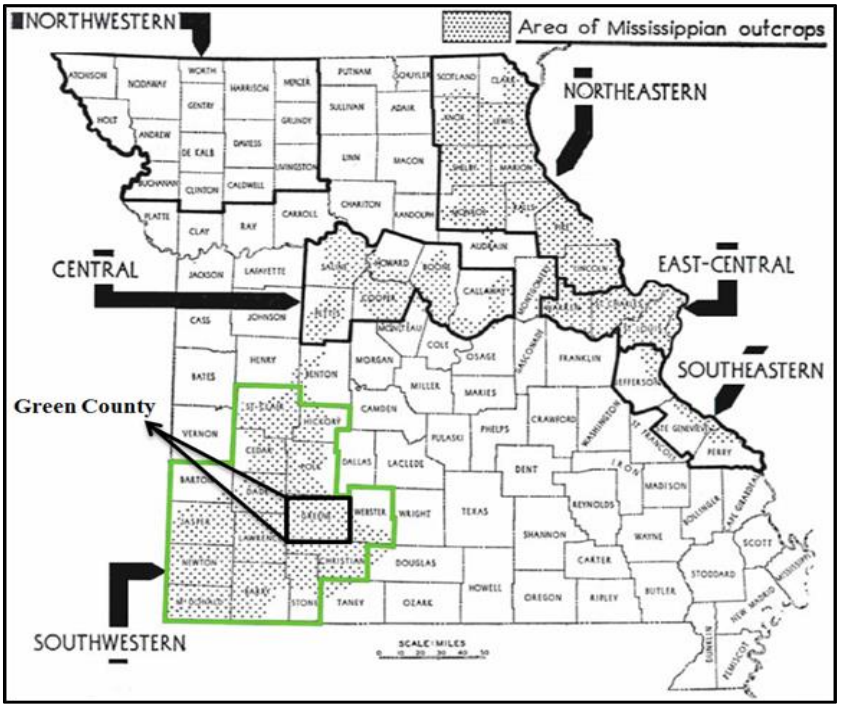

Figure 2.2. Regional Distribution of the Mississippian System in Missouri (Vineyard, 1992).

The geologic map and units in southwest Missouri are displayed in Figure 2.3. Each geologic rock unit has characteristics that need be addressed on a site-by-site basis. Most of the southwest Missouri is composed of Burlington-Keokuk Limestone (Mbk) a

material that is particularly prone to dissolve, thereby increasing the probability of catastrophic collapses, and through which surface water reaches the ground water supply.

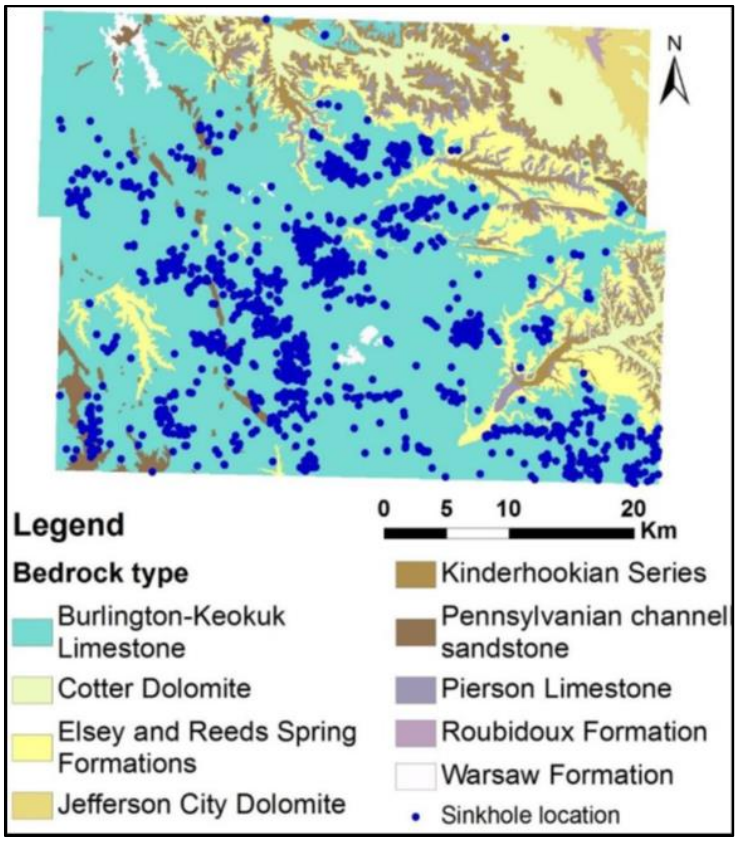

Figure 2.3. Geological Map of Southwest Missouri (ESRI data source: Missouri Geological Survey GEOSTRAT system, Sept 2015).

The Mississippian System is divided into two series: the Kinderhook and Osage. The Mississippian formations of the southwest Missouri are presented in Table 2.1. The total thickness of the Mississippian System in this part is about 640ft (195m), (Vineyard, 1992).

The Mississippian System starts with the Compton Formation, which has a thickness of less than 30ft (9m). The Compton Formation is overlain by the Northview Formation with an average thickness up to 80ft (24m). It is represented by brown siltstone and blue or bluish-green shale.

The Mississippian System continues with the deposition of the Pierson, Reeds Spring, and Elsey Formations. The total thickness of these three formations is about 260ft (79m). Cherty limestone is a dominant component in all three formations.

The deposition of the Mississippian System is finalized by the Burlington-Keokuk Formation. Further, the youngest exposed rock unit is in southwest Missouri. The thickness of this formation is approximately between 150 to 270ft (45 to 83m) and varies in thickness from place to place due to erosion. The majority of springs and caves in southwest Missouri are found in Burlington-Keokuk Limestone.

According to conventional geotechnical procedures, the collections of boreholes were drilled in southwest Missouri. The bedrock in the study location is intensely dissolved Burlington-Keokuk Limestone and can be characterized by the presence of pinnacles and cutters (Fellows, 1970), meaning that the depth in the bedrock varies significantly. Furthermore, even though the subsurface information obtained at a location is highly accurate, the interpolation between boreholes can sometimes be incorrect due to significant lateral variability in karst terrains.

In the study site, the shallow subsurface is mainly represented by rocks of the Osagean Series in the Mississippian System. The Mississippian System is represented Table 2.1, by the Pierson, Reeds-Spring, Elsey, and Burlington-Keokuk Formations. These four formations have similar lithologic characteristics, and they are sometimes difficult to differentiate.

Table 2.1. Geologic and Stratigraphic Units in southwest Missouri (Vandike, 1993).

System	Series	Group	Formation	Thickness (ft)
Mississippian	Osagean		Burlington- Keokuk Formation	150-270
			Elsey Formation	25-75
			Reeds Spring Formation	125
			Pierson Formation	90
	Kinderhookian	Chouteau	Northview Formation	5-80
			Compton Formation	30

The following sections discuss the late two collective units of Mississippian deposition system as shown in Figure 2.4.

2.2.1. Lower Mississippian of Lower Osagean. Lower Mississippian is Lower Osagean (Mlo) Elsey, Reeds Spring, and Pierson Formations. The Elsey Formation is light-gray, crystalline to micritic limestone with chert fragments and some crinoids. The Reeds Spring Formation is gray to brown; finely crystalline limestone with chert fragments. The Pierson Formation is brown to brown-gray and comprised of Magnesian limestone with chert nodules. The fine-grained matrix contains some fossil fragments (Muchaidze, 2008).

2.2.2. Lower Mississippian of Upper Osagean. Lower Mississippian is Upper Osagean (Muo) or (Mbk) Burlington, and Keokuk Formation, in southwest Missouri. The Burlington-Keokuk limestone is the most important formation in this research because the bedrock in the study site is from this formation. The Burlington Keokuk Formation is coarsely crystalline, light gray limestone with some fossiliferous limestone and chert

nodules. The limestone is comprised almost entirely of crinoid fragments. The Burlington-Keokuk Formation weathers to a red to reddish brown residual soil that contains a variable amount of chert fragments. It is almost entirely comprised of pure calcite. Thus, this formation is susceptible to weathering through the dissolution process. Uneven dissolution of this formation has resulted in a highly irregular bedrock-overburden interface (Fellows, 1970).

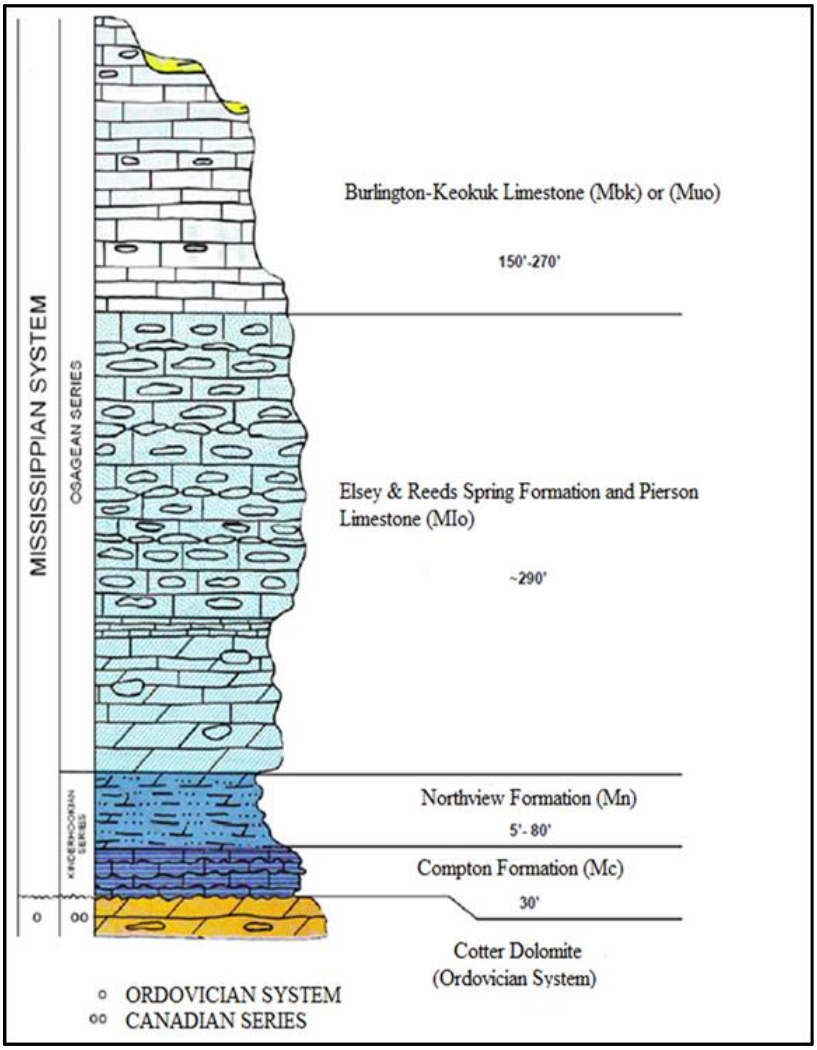

Figure 2.4. Stratigraphic Column for southwestern Mississippian System in southwest Missouri (Fellows, 1970).

2.2.3. Overview of Structure and Faulting Based on the Work of Coots (2007). The geologic structures in southwest Missouri are highly jointed with orientations that are trending N 20º W, and N 60º E and are approximately orthogonal to each other. Coots (2007) discussed three main fault types that are common in the area, namely, the Kinser Bridge fault, the Danforth Graben Fault, and the Pearson Creek Fault (Figure 2.5), all of which have a northwest – southeast trend with normal deracination. The Kinser Bridge Fault trends west-northwest with an average deracination of about 50ft (15m); the Danfort Graben Fault has a vertical deracination of about 70ft (21m), and trends northwestward; and the Pearson Creek Fault has a strike direction of N 55º W and a normal deracination of between 10 and 20 ft (3 and 6m).

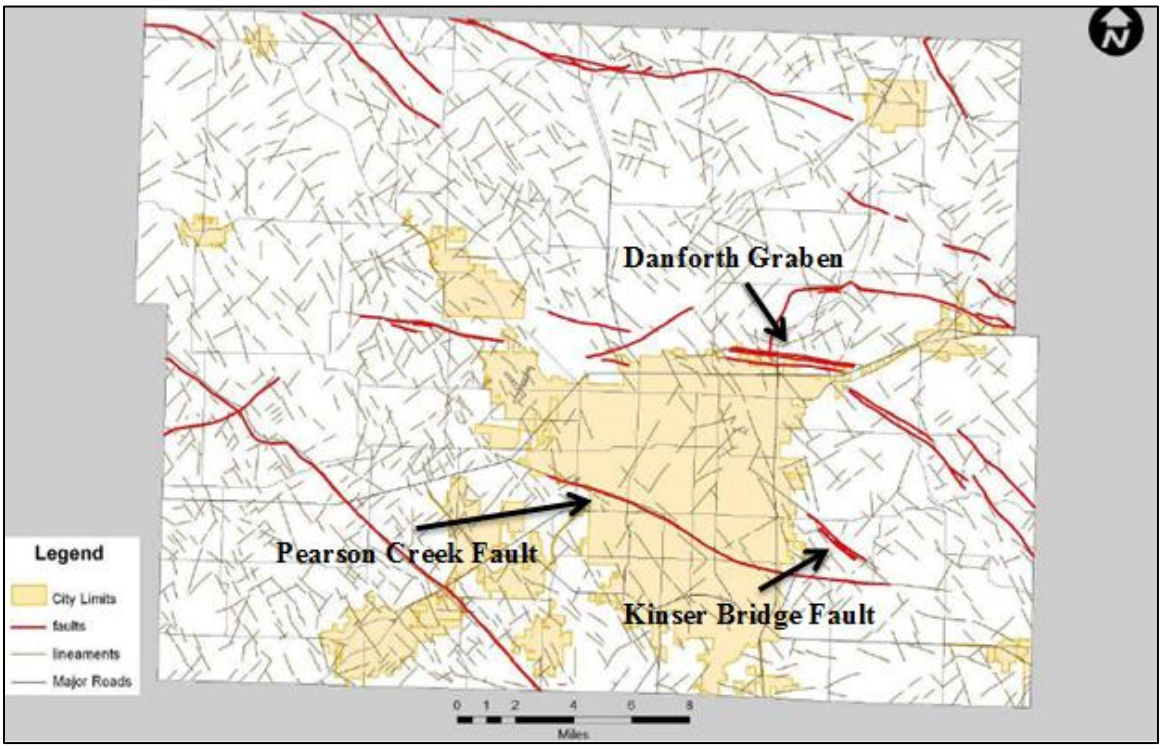

Figure 2.5. Faults and Lineament in Southwest Missouri (Coots, 2007).

2.3. FORMATION OF KARST FEATURES

According to the Missouri Department of Natural Resources dictionary, karst is "a type of topography that is formed on limestone, gypsum, and other rocks by dissolution, and is characterized by caves, sinkholes, and underground drainage". Karst terrain is characterized by the presence of springs, caves, sinkholes, and a unique hydrogeology (USGS, 2012). Karst is a term derived from the German form of the Slavic word "Kras" or "Krs," meaning a bleak waterless place (Monroe, 1970).

Features inherent in karst terrain are caves, sinkholes, springs, dry valleys, and loosening or disappearing streams and springs. The complex terrain results from the chemical weathering of carbonate and other soluble rocks, and the formation of karst features are controlled in part by pre-existing fractures within the bedrock (Ford & Williams, 2007). Sinkhole formation is also controlled by overburden thickness, fluctuation of the water table, soil type, and the presence of recharge or discharge zones (Denizman, 2003).

Karst is formed when rain falls and carbon dioxide in the atmosphere is dissolved making the rainwater acidic and consequently dissolving soluble rocks. It is worth noting that the acidic rainwater passes through dead plant materials/debris in the soil and even becomes more acidic as it percolates through cracks, consequently dissolving the bedrock (limestone, dolostone, marble, gypsum and salt). Dissolution continues as the water moves sidelong along bedding planes and joints and fractures in the rock, forming conduits in the rock.

The carbonate rocks, limestone, and dolostone are predominantly composed of calcite mineral (CaCO3) and dolomite mineral (CaMg (CO3)2), and both mainly calcite,

are susceptible to dissolution when slightly acidic water acts on them. Meteoric water absorbs carbon dioxide (CO2) from the atmosphere and thus becomes slightly acidic. After meteoric water saturates the ground, it passes through soil that may increase its CO2 concentration. At the point where water enters carbonate rock, it reacts with soluble minerals. Dissolved matter will be washed away, and as a result, features such as dissolution-widened fractures form. As erosion continues underground, caves get hollow enough and the roofs thin and eventually collapse to form a sink.

Karst terrain is characterized by caves, sinkholes, underground streams, and other features formed by the slow dissolution, rather than the mechanical eroding, of bedrock. People have discovered the difficulties (e.g., sinkhole collapse, sinkhole flooding, and easily polluted groundwater) of living on those terrains as the population has grown and expanded into those areas as shown in Figure 2.6, and therefore either serve as recharge or discharge areas depending on certain geological and hydrogeological factors.

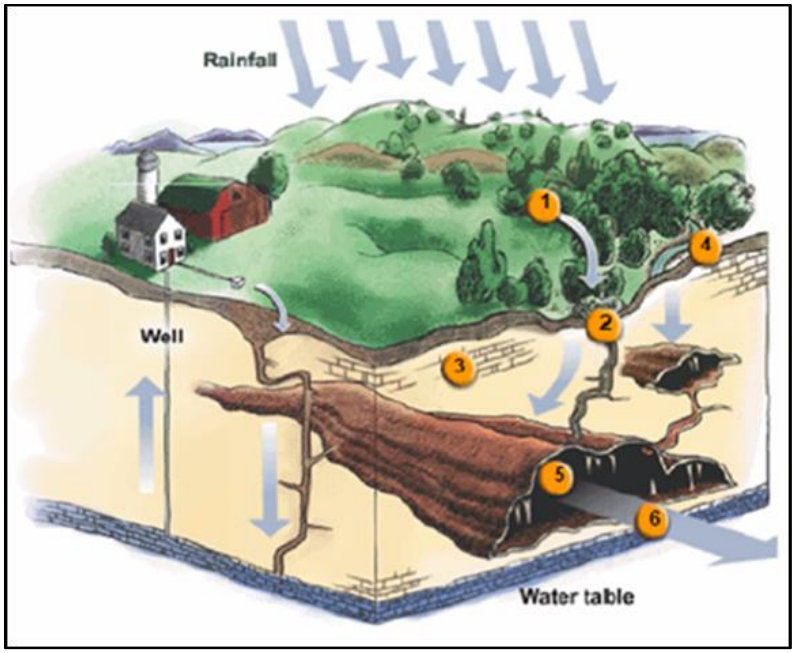

Figure 2.6. Figure Showing Karst Topography Features. (www.springfieldmo.gov/documentcenter/view/11091).

2.3.1. Groundwater Recharge. Groundwater recharge (also called deep drainage or deep percolation) is a hydrologic process where water moves downward from surface water to groundwater. Recharge is the primary method through which water enters an aquifer. This process usually occurs in the vadose zone below plant roots and is often expressed as a flux to the water table surface. Recharge occurs both naturally through the water cycle or through anthropogenic processes, such as rainwater, melting snow, or other surface water.

2.3.2. Sinkhole or Sink. A sinkhole or sink is a collapsed part of bedrock above a void. They may be a sheer vertical opening into a cave or a shallow depression of many acres. They can appear suddenly, creating havoc for Ozarks landowners or highway managers.

2.3.3. Soluble Bedrock. Soluble bedrock is characterized by underground drainage systems with sinkholes and caves. It has also been documented for weathering-

resistant rocks. Subterranean drainage may limit surface water with few to no rivers or lakes. However, in regions where the dissolved bedrock is covered (perhaps by debris) or confined by one or more superimposed insoluble rock strata, distinctive karst surface developments might be totally missing.

In Missouri, karst forms in limestone (calcium carbonate) and dolomite (magnesium calcium carbonate).

2.3.4. Natural Bridge or Tunnel. Natural bridges may be the remains of a cave that collapsed, with only a portion of the ceiling still standing. But while the entrance to caves can be mysterious or even foreboding, natural bridges are more inviting with the light at the end of the tunnel beckoning a visitor explore. Natural bridges are usually shorter than a tunnel and air-filled rather than filled partially with water.

2.3.5. Losing Stream. A losing stream is a stream or river that loses water as it flows downstream. The water infiltrates the ground, recharging the local groundwater because the water table is below the bottom of the stream channel. Losing streams are also common in regions of karst topography where the stream water may be completely captured by an underground cavern system and become a subterranean river.

2.3.6. Cave. A cave is a hollow place in the subsurface, or an air-filled underground void. A specifically, a cave is natural underground space large enough for a human to enter and often extends deep underground. The formation and development of a cave is known as speleogenesis. Caves are formed by various geologic processes and can be variable sizes. This may involve a combination of chemical processes, erosion from water, tectonic forces, microorganisms, pressure, and atmospheric influences.

2.3.7. Spring. A spring can be developed where surface water has infiltrated the Earth's surface (recharge area) due to karst topography, thereby becoming part of the area's groundwater. The underground water then penetrates through a network of cracks and fissure openings, ranging from intergranular spaces to large caves. The water emerges from below the surface in the form of a karst spring. A confined aquifer forces the spring to appear on the surface land.

2.4. OVERVIEW OF SINKHOLE FORMATION PROCESS

Sinkholes, also called dolines, form in the same manner that caves are formed (dissolution of soluble rocks by surface water and groundwater to create a void or an opening in the soil or rock). Sinkholes are the most diagnostic surface expression of karst landscapes. They are important near-surface indicators of active karst features such as dissolution-enlarged fractures, caves, and conduits. Sinkholes can vary from a few feet to hundreds of acres wide and from less than 1 to more than 100 feet deep. Some are rounded in shape, whereas others have vertical walls. Although most sinkholes drain rapidly, some have natural plugs and may hold water for many years. There are three types of sinkholes: Collapse Sinkholes, solution-sinkholes, and cover-subsidence sinkholes.

2.4.1. Collapse Sinkholes. Collapse Sinkholes are karst-related features that are not bound by a defined drainage area. Collapse sinkholes form as a void in the soil layer migrates toward the surface. A sudden collapse occurs when the roof of the cavity can no longer support its own weight and caves-in, creating an abrupt and dramatic sinkhole. A collapse sinkhole will commonly develop in the floor of an existing depression sinkhole.

Sinkhole collapses are very common in the Ozarks. On average, the southwest Missouri responds to over 30 reported collapses every year. A sinkhole of this type can be dangerous if someone were to fall in and should therefore be repaired or fenced off as soon as possible.

2.4.2. Solution-Sinkholes. Solution-sinkholes occur in areas where carbonate rocks like limestones and dolostones are exposed at land surface or are covered by thin layers of soil and permeable sand. Dissolution is most active at the limestone surface and along joints, fractures or other openings in the rock that permit water to move easily into the subsurface. When rain falls, surface water percolates through joints in the carbonate rock and the dissolved rock is carried away from the surface, forming a small depression. Further drainage of the carbonate surface accelerates the dissolution process and enlarges the depression. As more debris is carried into the developing sinkhole, water outflow may be plugged to form a pond and may hold water for years. Solution sinkholes tend to have gently sloping sides and seldom pose a hazard by collapsing.

2.4.3. Cover-Subsidence Sinkhole. Cover-Subsidence Sinkhole is one of the most dramatic forms of land subsidence is the collapse of the ground surface into natural underground caverns. The material can no longer support its own weight, and a sudden collapse forms this type of sinkhole. Heavy rainfall, drought, or mechanical loading can trigger this type of sinkhole. The collapse is generally abrupt and can be catastrophic. A sinkhole formed in this manner is often fairly circular with steeply sloping sides. The sinkhole that developed in Exeter, Missouri is pictured in Figure 2.7 and Figure 2.8.

Figure 2.7. Buildings collapse into a sinkhole at Disney World in, Florida. (http://www.csmonitor.com/Science/2013/0813/Sinkhole-Disney-World-visitors-walking-on-holey-ground).

Figure 2.8. Buildings collapse into a sinkhole at the Summer Bay Resort in Clermont, Florida. (http://www.amusingplanet.com/2013/09/disastrous-sinkholes).

In Missouri, this type of sinkhole is more common than the other types based on the mechanism of its formation and nature of overburden materials. In areas where limestone is buried beneath a sufficient thickness of unconsolidated material, few sinkholes generally occur. If the overburden is dense plastic clay, its low permeability may impede downward movement of surface water and slows the development of solution cavities in the underlying limestone.

2.5. KARST TOPOGRAPHY IN MISSOURI

Missouri is one of seven states with karst terrain. Approximately 59% of Missouri is covered by carbonate rock, most of which is exposed (Vandike, 1997). Major karst areas in Missouri occur in the Mississippian rocks.

Three of the four largest metropolitan areas in Missouri (St. Louis, Springfield, and Columbia) are located almost entirely on karst terrain. Most of the karst features in Missouri are advanced in the southwest Missouri and Salem plateaus. However, there are also karst features north of the Missouri River. Karst terrain is particularly susceptible to catastrophic collapse. Furthermore, contaminants can also become concentrated in karst depressions, so knowledge of the bedrock topography can be useful in remediation work (Vandike, 1997).

The Ozark Plateau Aquifer is a large system comprised of many smaller aquifers spread over a large geographic region across Oklahoma, Missouri, Kansas, and Arkansas. This system consists of Ozark aquifers, St. Francois aquifers, and the Springfield Plateau. It has been the most significant water source for southwest Missouri, northeastern Oklahoma, southeast Kansas, and northern Arkansas (Macfarlane et al., 2005).

The Ozark area is experiencing a significant population growth in southern Missouri regions; the population grew increased by 11% in 1990 and 27% in 2000, (Missouri Department of Conservation, 2005). According to the Missouri Department of Natural Resources, there are over 5,500 caves, more than 9,500 sinkholes, more than 2,800 springs, and loosing streams recorded in Missouri (Vandike, 1997).

3. GEOPHYSICAL INVESTIGATIONS

Several techniques have been used to characterize karst terrain. More detailed investigations of the shallow subsurface often rely on boreholes control to characterize subsurface conditions, but due to the spatial variability of karst terrain, and information from individual boreholes may be insufficient for a complete site evaluation. Geophysical exploration methods have been used in several fields to study a wide range of targets within the subsurface, such as discovering the shallow structure of subsurface and properties at depths up to 100ft. (30m).

Geophysical data can provide suitable continuous coverage between boreholes and significantly decrease ambiguity (subsurface conditions). Numerous geophysical techniques including multichannel analysis of surface waves (MASW) and electrical resistivity tomography (ERT) can be employed to characterize the subsurface in complex terrain like karst regions (Doolittle et al., 1998; Miller et al., 2005; Thierry et al., 2005; Schrott & Sass, 2008). A combination of methods is often used to constrain the interpretation because each technique has inherent advantages and drawbacks.

3.1. MULTICHANNEL ANALYSIS OF SURFACE WAVES (MASW)

3.1.1. Overview. Multichannel Analysis of Surface Waves (MASW) is a non-destructive seismic survey method based on the measurement of seismic surface waves generated by seismic source (active MASW) or ambient noise from cultural activities (passive MASW) for evaluation of the elastic condition (stiffness) of the ground for geotechnical purposes. Nowardays MASW is a commonly used geopgysical technique because of its effectiveness for providing shear-wave velocities measurements and

simplicity of use (Park, 2013). The MASW method has become one of the main surface wave methods to determine shear-wave velocitiy variations for geophysical and civil engineering applications with observed difference of approximately 15% error between the results obtained by MASW and borehole control measurements (Xia et al., 2002; Xia, 2014). Typical MASW survey can be broken down into three steps: data acquisition, data processing, data interpretation. Final shear-waves profile can be presented in 1D, 2D and 3D formats (Park and Taylor, 2010).

3.1.2. Basic Concept. MASW method utilizes frequency-dependent properties of particular type of seismic surface waves (fundamental-mode Rayleigh waves) horizontally travelling along the earth surface directly from the impact point to the receiver spread. The method provides the shear wave velocity information in 1-D (single vertical shear wave velocity profile), 2-D (shear-wave velocity cross-section) or 3-D (interpolation between densely distributed 1-D profiles) formats.

3.1.3. Seismic Waves. In general, seismic waves are parcels of strain energy that propagate outwards from a seismic source. There are two main categories of seismic waves that propagate within the ground and along its surface: body waves and surface waves (Aki & Richards, 2002, Evrett, 2013).

3.1.4. Body Waves. There are two types of body waves: compression waves (the longitudinal, primary or dilatational) and S-waves (the transverse, secondary, or shear-wave).

Body waves can propagate through the internal energy of an elastic solid and may be one of two types. In compressional/dilatational primary (or P-) waves, the particles of the medium move in the direction of wave travel, involving alternating expansion and

contraction of the medium. The particle motion of compressional waves is parallel to the motion of the wave propagation, causing the dilatation and compression of elementary volume particles (Aki & Richards, 1980), as shown in Figure 3.1(a)).

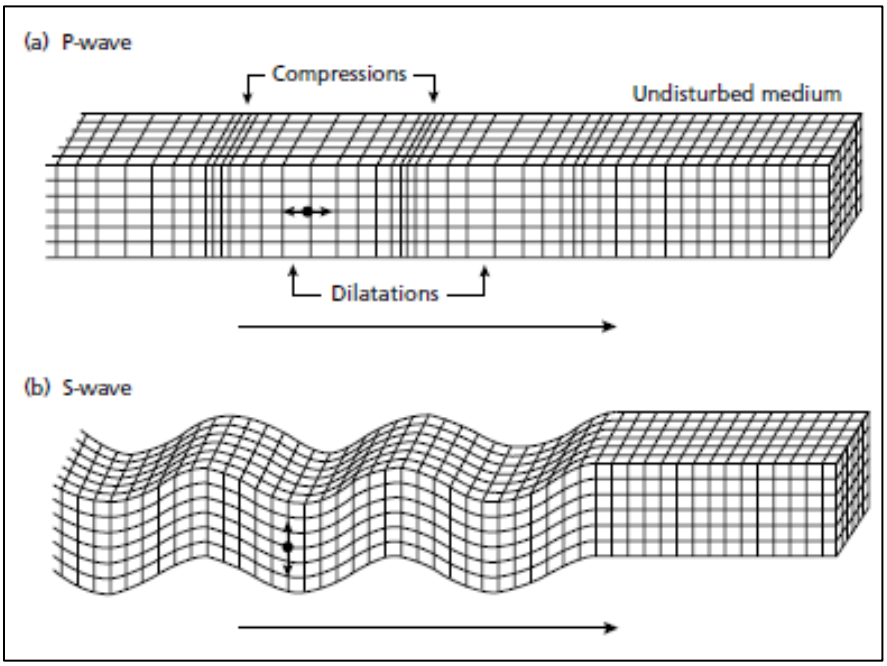

Figure 3.1. Elastic deformations and ground particle motions associated with the passage of body waves. (a) P-wave. (b) S-wave (Bolt, 1982).

3.1.5. Surface Waves. Surface waves are results of interfering *P*-waves and/or *S*-waves travelling primarely along the free surfaces or along the boundary of dissimilar materials (Kearey, Brooks, & Hill, 2002). They induce particles motion which is perpendicular to the direction of wave propagation and has both a vertical and a horizontal component. There are two types of surface waves that are most interesting for engineering purposes based on their modes of propagation, dispersion velocities and the depth range of the associated particle motion: Rayleigh waves and Love waves. Rayleigh waves travel along a boundary with particle motion in vertical direction along the wave patch and always exist in the presence of a free surface. Love waves induce particles

motion which is horizontal and transverse to the direction of wave propagation and only generated in conditions where a soft layer overlying a stiffer layer (Parasnis, 1997). Since their particle motion is always horizontal, Love waves are rarely recorded in seismic surveys where only vertical source and receivers are used (Park et al., 1997), as shown in Figure 3.2.

They represent the strongest portion of the signal received during a seismic survey. For the preliminary location, an average value of Vp/Vs = 1.73 of the ground crust is used. However, Vp/Vs can be determined with a fair degree of accuracy by the Wadati-plot method (Wadati, 1933).

$$Vp = 1.7\ Vs \tag{3.1}$$

The speed of wave propagation is NOT the speed at which particles move in solids (~ 0.01 m/s).

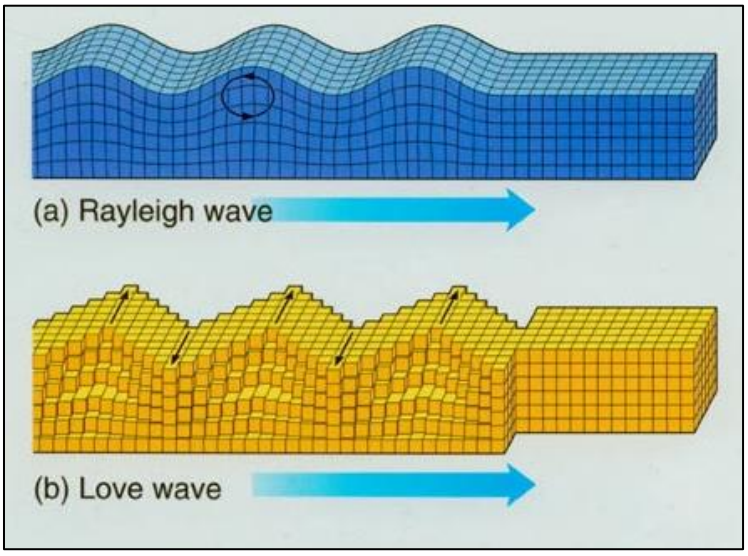

Figure 3.2. (a) Rayleigh wave motion. (b) Love wave motion (http://thinkgeogeek.blogspot.com).

More specifically, in this technique, phase velocities are calculated for each component frequency of the field-recorded Rayleigh waves. The resulting dispersion curve (phase velocity vs. frequency) is inverted using a least squares approach, and a vertical shear-wave velocity profile is generated (Miller et al., 2000; Nazarian et al., 1983; Stokoe et al., 1994; Park et al., 1999a, 1999b, 2000; Xia et al., 1999).

Rayleigh waves result from the interaction of P-waves and vertical (SV) waves with the surface of the ground (Aki & Richards, 1980). The particle motion of Rayleigh waves moves perpendicular to the surface but travels along the wave path (Kearey, Brooks & Hill, 2002). The wave motion is retrograde (counterclockwise) closest to the surface, but becomes prograde (clockwise) at greater depths. More than two-thirds of the seismic energy that is generated is imparted (Loke, 2000).

Particle motion associated with Love waves is parallel to the free surface and perpendicular to the direction of the waves, whereas Rayleigh waves move perpendicular to the surface but travel along the wave path (Kearey, Brooks and Hill, 2002). Love waves are a form of a polarized shear wave and are observed in a multilayer media when the shear wave velocity of the top layer is less than that of the lower layer (Parasnis, 1997). They are the fastest surface wave, move along the ground from side-to-side and are confined to the surface of the crust. Since their particle motion is always horizontal, (Love) waves are seldom recorded in seismic surveying where only vertical sources and receivers are used (Park et al., 1997).

3.1.6. Rayleigh Waves in Homogeneous Elastic Half-Space. Rayleigh waves generated by a vertical point source on a free surface propagate along cylindrical wavefronts away from the impact point (Richart, Hall, & Woods, 1970). Body waves

propagate radially, from the exterior of the source, both into the medium and along the surface, along a hemispherical wavefront, as shown in Figure 3.3. As the waves transfer outward and encounter an increasingly larger volume of material, their amplitude decreases.

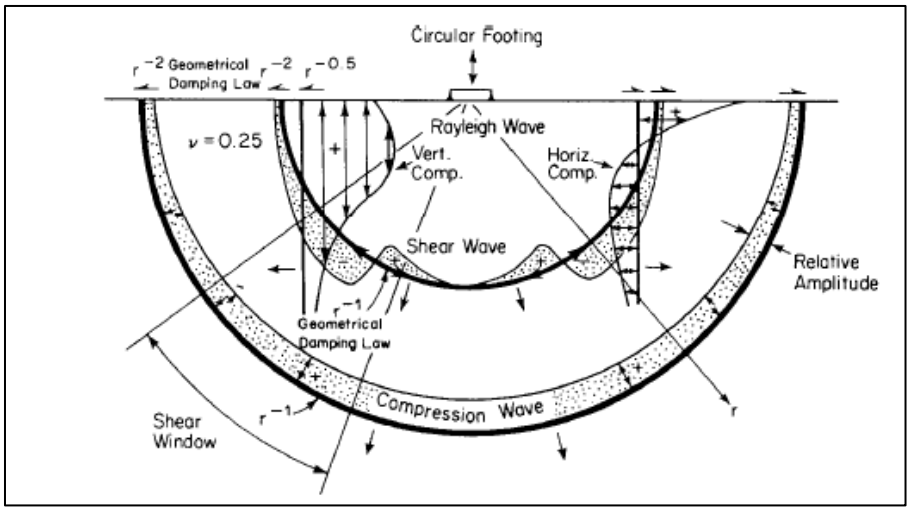

Figure 3.3. Distribution of compressional, shear and Rayleigh waves generated by a point source in a homogeneous half-space, isotropic, elastic half-space (Richart et al., 1970).

This is called geometrical spreading (or geometrical damping) (Aki & Richards, 1980; Richart et al., 1970). In a homogeneous elastic half-space, the amplitude of Rayleigh waves decreases as r-0.5, where r is the distance from the impact point. For comparison, the amplitude of body waves decreases as r-2 along the surface and r-1 into the medium. As two-thirds of the total seismic energy is imparted into Rayleigh waves and Rayleigh waves decay more slowly with distance than body waves, the wave field becomes dominated by Rayleigh wave motion at nearest distances from the seismic source (Richart et al., 1970). Around 67% of the seismic energy is imparted into Rayleigh waves, while about 26% is imparted into shear waves and 7% into compressional waves (Woods, 1968).

The amplitude of Rayleigh waves decays exponentially with depth (Richart et al., 1970). The simplest method is attribution of a factored shear wave phase velocity (usually 0.9 times the Rayleigh wave velocity (Joh 1996, Foti 2000 & Okada 2003) to a depth equivalent to a fraction of the Rayleigh wavelength, λ. Fractional depth factors range from λ/4 to λ/2 (Jones1958, Ballard & McLean 1975; Abbis, 1981).

Gazetas (1982) recommended that λ/4 be used where the stiffness increases significantly with depth and that λ/2 be used for more homogeneous stiffness profiles. However, a factor of λ/3 is most commonly used (Bullen 1963 & Richart et al., 1970) because a significant proportion of the particle motion in the ground associated with Rayleigh wave propagation is approximately this depth. The horizontal and vertical Rayleigh wave displacement amplitudes as a function of dimensionless depth are shown in Figure 3.4 for several values of Poisson's ratio (v) = 0.25 (Richart et al., 1970).

Rayleigh waves have unique properties that allow them to be transformed into subsurface shear-wave velocity profiles (Surf-Seis, 2006). Rayleigh waves are dispersive in nature (different frequencies travel with different phase velocities). The highest usable Rayleigh wave frequency that has been recorded (for geotechnical purposes) involves particle motion within the shallowest depth range (approx. 1 Rayleigh wavelength; typically upper few ft) and travels with a velocity that is mostly a function of the average shear-wave velocity within that depth range.

Intermediate frequencies for Rayleigh waves involve particle motions to intermediate depths (to approx. 1 Rayleigh wavelength), and they travel with velocities that are a function of the average shear-wave velocity over those intermediate depth ranges. Also, the lowest recorded usable frequency involves particle motions to the

greatest depth (1 Rayleigh wavelength) and travels with a velocity that is a function of the shear-wave velocity over that depth range.

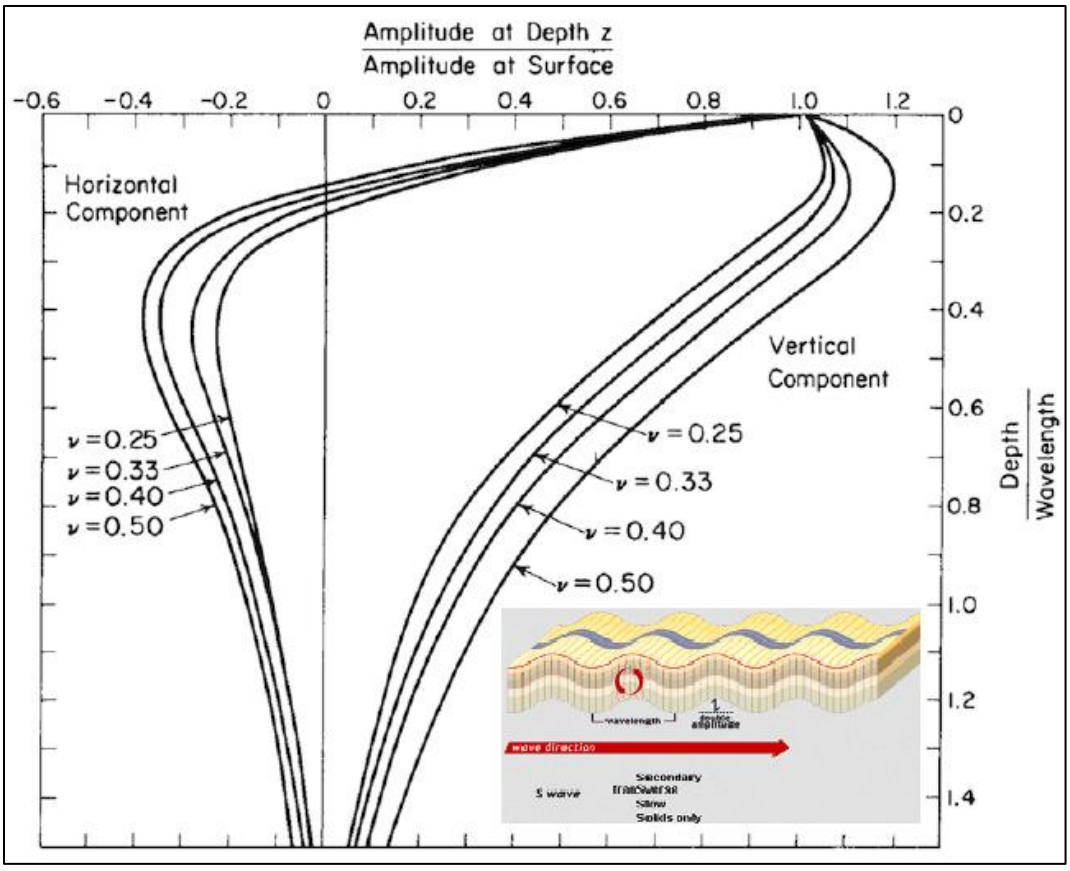

Figure 3.4. Displacement amplitude of Rayleigh waves versus dimensionless depth(Richart et al., 1970).

Equations describing Rayleigh waves propagate along the free surface of the earth with particle motions that decay exponentially with depth. The lower component frequencies of Rayleigh waves involve particle motions at greater depths. In a homogeneous (non-dispersive) medium, Rayleigh wave phase velocities are constant.

Rayleigh wave phase velocities are a function of both the shear-wave and the compression wave velocities of the subsurface. The interrelationships between Rayleigh

wave velocities (VR), shear-wave velocities (β) and compression wave velocities (α) in a uniform medium are expressed in Equation 3.2 (Anderson, 2010):

$$VR6 - 8\beta2VR4 + (24 - 16\beta2 /\alpha2)\ \beta4VR2 + 16(\beta2/\alpha2 - 1)\ \beta6 = 0 \quad (3.2)$$

where

VR is the Rayleigh wave velocity within the uniform medium,

β is the shear-wave velocity within the uniform medium (also denoted as Vs), and

α is the compressional wave velocity within the uniform medium (Also denoted as Vp).

Although the Raleigh wave phase velocity is a function of both compressional (α) and shear-wave (β) velocities, it is much more sensitive to variations in β than in α in Equation 3.3.

$$VR< \beta < \alpha \quad (3.3)$$

Lower frequencies involve particle motion at greater depths, causing VR to also vary with frequency.

Equation 3.4 might initially suggest that it would be difficult to extract the shear-wave velocity because the equation contains two unknowns (shear and compression wave velocities). Fortunately, this is not the case because Rayleigh wave phase velocities are influenced much less by changes in compression wave velocity than by changes in shear wave velocity. In a uniform medium, Rayleigh wave velocity (VR) and shear-wave velocity (β) are related by Equation 3.4 (Anderson, 2010):

$$\beta = VR/C \quad (3.4)$$

The propagation velocity of individual frequency components is referred to as phase velocity C. The variable C is a constant that changes slightly depending on Poisson's ratio of the material through which the seismic waves travel. Even in extreme variations of Poisson's ratio, C only ranges from 0.874 to 0.955 (Anderson, 2010). It is suggested that if a value for C is assumed and the frequencies (with their respective surface wave velocities) are recorded, then a shear-wave velocity profile can be developed through analysis, and a velocity image of the subsurface can be generated (Anderson, 2010).

Rayleigh wave velocities, as noted in Equation 3.2, are a function of both the shear-wave velocity and the compressional wave velocity of the subsurface. A plot of the frequency versus the phase velocity, known as a dispersion curve, visualizes these relations. The shape of the dispersion curve is referred to as the dispersion characteristic of the Rayleigh wave (Everett, 2013).

3.1.7. Rayleigh Waves in Vertically Heterogeneous Elastic Half-Space. Shear-wave and compressional wave velocities vary with depth. Hence, different component frequencies of Rayleigh waves (involving particle motion over different depth ranges) exhibit different phase velocities (Bullen, 1963). The phase velocity of each component's frequency is a function of the variable body wave velocities over the vertical depth range associated with that particular Rayleigh wavelength. More specifically, in the subsurface, the Rayleigh wave phase velocity equation takes the following form:

$$V_R\,(fj, C_Rj, \beta, \alpha, \rho, h) = 0 \quad (j = 1, 2, \ldots, m) \tag{3.5}$$

where

fj is the frequency in Hz,

V_Rj is the Rayleigh-wave phase velocity at frequency fj,

$\beta = (\beta 1, \beta 2, \ldots, \beta n)$ T is the shear-wave velocity vector,

βi is the shear-wave velocity of the i th layer,

$\alpha = (\alpha 1, \alpha 2, \ldots, \alpha n)$ T is the compressional P-wave velocity vector,

αi is the P-wave velocity of the i th layer,

$\rho = (\rho 1, \rho 2, \ldots, \rho n)$ T is the density vector,

ρi is the density of the i th layer,

h = (h1, h2,…., hn-1) T is the thickness vector,

hi is the thickness of the i th layer and,

n is the number of layers within the earth model,

The velocity of Rayleigh waves is comparable to the velocity of shear waves. In a rock formation with a Poisson ratio of approximately 0.25, the velocity of the Rayleigh wave is approximately 92 % of the velocity of the shear wave. In materials with rates from 0.4 to 0.5, the percentage increases to 94 to 95.5 %, respectively (Steeples, 1998). As a general rule, the velocities of Rayleigh waves are assumed to be approximately 90 to 92 percent of the respective shear-wave (Ivanov, Park, & Xia, 2009; Parasnis, 1997). The shear-wave velocity can be estimated within a ten percent margin of error using these assumptions (United States Corps of Engineers, 1995).

The shear-wave velocity of a material is very important when predicting the impact that an earthquake's seismic waves will have on a material as the waves pass through it (Wood, 2009). Knowing the shear-wave velocity of material, one can determine the shear modulus using the relationship between the shear-wave and soil or rock as related by Equation 3.3:

$$\mu=\rho Vs^2 \quad (3.6)$$

where

μ = shear modulus,

p = mass density, and

Vs = shear-wave velocity.

Rayleigh wave velocities, as noted in Equation 3.5, are a function of both the shear-wave velocity and the compressional wave velocity of the subsurface. A plot of frequency versus phase velocity, known as a dispersion curve, visualizes these relations. The shape of the dispersion curve is referred to as the dispersion characteristic of the Rayleigh wave (Evrett, 2013). In MASW, phase velocities are calculated for each component frequency of the field-recorded Rayleigh waves. Then the resulting dispersion curve (phase velocity vs. frequency) is inverted using a least squares approach, and a vertical shear-wave velocity profile is generated (Miller et al., 2000; Nazarian et al., 1983; Stokoe et al., 1994; Park et al., 1999a, 1999b, 2000; Xia et al., 1999). Typical dispersion curve has multimodal character (multiple phase velocities existing for a certain frequency). The mode with the lowest phase velocity (at each frequency) is defined as fundamental mode and exists at all frequencies. Other higher modes, called the first mode, second mode, etc. They have higher phase velocities and are only exist above a cut-off frequency that depends on the mode (Evrett, 2013).

3.2. MULTICHANNEL ANALYSIS OF SURFACE WAVES DATA ACQUISITION

Rayleigh wave velocities are, in general, shown to increase with depth (e.g. waves with longer Rayleigh wavelengths and lower frequencies) and propagate faster than those with shorter wavelengths. The relation between frequency (*f*) and Rayleigh wavelength is called a phase velocity (c(*f*)). These unique characteristics result in a different Rayleigh wavelength (λ(*f*) given as (Kramer, 1996) , as shown in Figure 3.5.

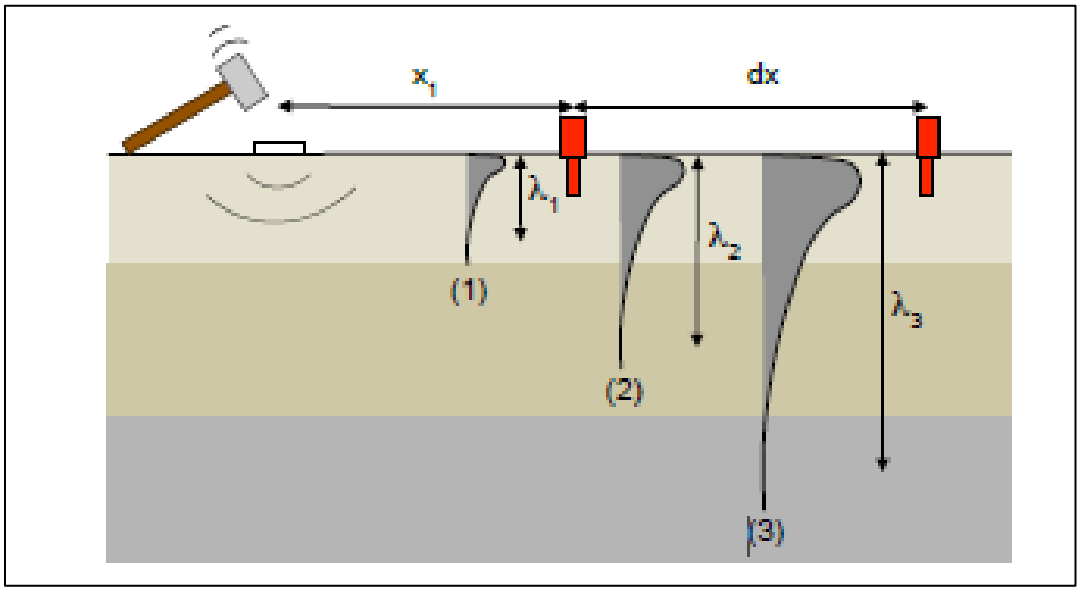

Figure 3.5. Rayleigh wave components with different Rayleigh wavelengths propagating through a layered medium. Wave components with different frequencies reflect soil properties at diverse depths.

The material properties of the topmost layer have an impact on the phase velocity of wave component (1), whereas the phase velocities of wave components (2) and (3) also depend on the properties of the deeper layers.

$$\lambda\,(f) = c(f)/f \tag{3.7}$$

The variable C is a constant that changes slightly depending on Poisson's ratio of the material through which the seismic waves travel. Even in extreme variations of Poisson's ratio, C only ranges from 0.874 to 0.955 (Anderson, 2010). It is suggested that if a value for C is assumed and the frequencies (with their respective surface wave velocities) are recorded, then a shear-wave velocity profile can be developed through analysis, and a velocity image of the subsurface can be generated (Anderson, 2010). These unique characteristics result in a different Rayleigh wavelength λ.

Depending on the nature of the seismic source, MASW method can be categorized as active or passive. The active MASW adopts the conventional seismic refraction mode of surveying by using an active seismic source, such as a sledgehammer, accelerated weight drop or vibroseis deployed in traverse along a linear array of receivers (Park et al., 1999). The passive MASW method utilizes surface waves generated by natural sources or cultural activities, highway traffic and construction equipment (Park et al., 2007). Depending on the receiver configuration there are two ways to conduct a passive MASW survey - the passive remote MASW (Park et al., 2004; Park et al., 2005) employs a two-dimensional receiver array and the passive roadside MASW (Park and Miller, 2008) uses linear one-dimensional receiver array. Data acquisition is more tolerant in parameter selection than other seismic methods because of the easily achieved high level of signal-to-noise ratio in seismic field records.

For the acquisition of active MASW data, low frequency (for example, 4.5 Hz), vertically polarized geophones are lined on the test site surface at the appropriate equal intervals. The number of geophones used is typically 24 or more with a constant inter-geophone spacing that is optimized for site-specific geologic conditions (Donohue,

Forristal, & Donohue, 2013; Lin, Chang, & Chang, 2004). Each geophone is connected to a separate recording channel (Park et al., 1997) and the whole array is connected to engineering seismograph and field laptop equipped with software necessary for data recording. A surface wave is generated with an impact load at one end of the lineup and the geophones record the resulting wave motion as a function of time. The seismic source may be a 20-lb sledgehammer, a mechanical impact device, a shotgun or explosives, depending upon the depth of the investigation and the site-specific conditions. The arrival of surface wave is detected along a set of geophones and recorded on a seismograph, with the output of each geophone being displayed as a single trace.

Proper setup of data acquisition parameters is essential for the success of the surface wave survey. The important field parameters are total length of the receiver spread, source offset (the distance between the source and the nearest geophone), and receiver spacing.

As the geophones only record vertical motion, it is important that they are placed vertically in the subsurface. Each geophone is connected through a separate recording channel to a data acquisition card and a computer equipped with the necessary data acquisition software (Figure 3.6.).

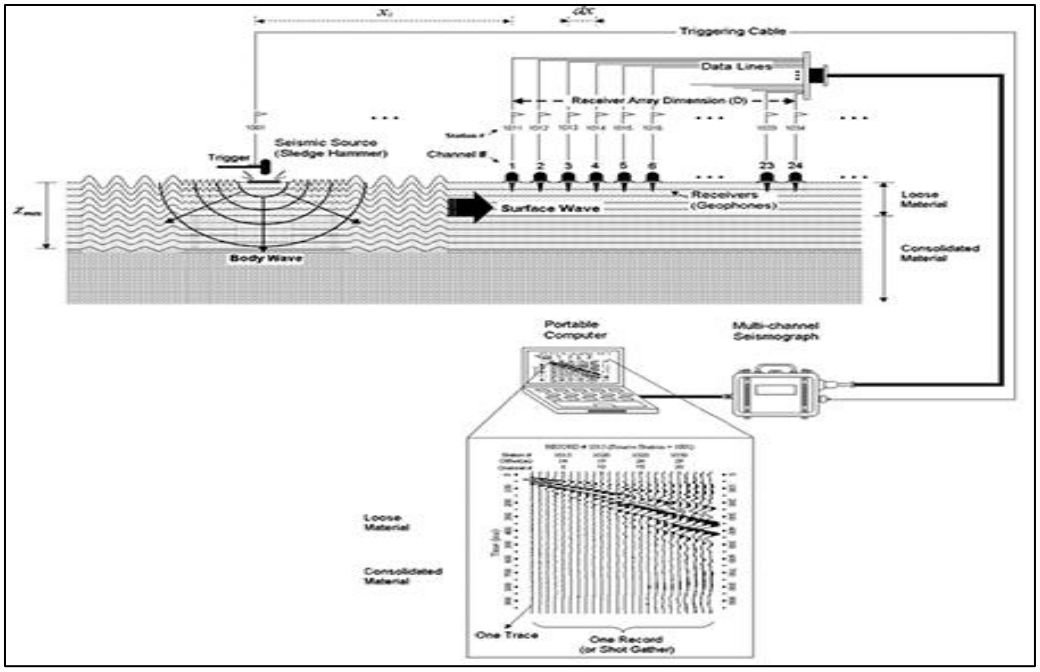

Figure 3.6. The instrumentation used in the MASW tomography survey (Park et al., 2002).

As illustrated in Figure 3.6, geophones are profiled up on the surface of the test site. A wave is generated, and the wave propagation is recorded. The maximum depth of the investigation (Zmax) varies with the site, the natural frequency (*f*e) of the geophones and the type of seismic source that is used. The maximum investigation depth is determined by the longest Rayleigh wavelength that is obtained during data acquisition (λmax). The following is a commonly adopted empirical criterion (Park & Carnevale, 2010):

$$Zmax \approx 0.5\lambda max \tag{3.8}$$

3.2.1. Geophone Spread Length. The overall geophone spread length (D) defines the longest Rayleigh waves wavelength that can be analyzed. It is also related to the maximum investigation depth (Zmax), since the length of the receiver array is related to the longest Rayleigh wavelength that is obtained during data acquisition. A common

criterion is that the longest Rayleigh wavelength (λmax) that can be analyzed is approximately equal to the length of the receiver array (Park & Carnevale, 2010):

$$\lambda max \approx D. \quad (3.9)$$

Attempts to analyze longer Rayleigh wavelengths than those indicated by Equation 3.9 can lead to less accurate results. Recent studies have shown that although there is fluctuating inaccuracy, it will remain within 5% for the interval $D \leq \lambda max \leq 2D$ (Park & Carnevale, 2010), because of the uncertainties (noise) always included in the measurement. A very long receiver spread should be avoided. Surface waves generated by the most commonly used seismic sources (e.g. reasonably heavy sledgehammers) will have attenuated noise level at the end of an excessively long receiver spread, making the signal from the furthermost receivers too noisy to be usable (Park et al., 1999; Xia et al., 2009). The maximum wavelength that can be accurately analyzed is approximately equal to the half of the length of the overall geophones spread.

3.2.2. Source Offset. The appropriate choice of source offset eliminates the near-field effect (the risk that geophones will pick up surface waves that were not fully developed. Long source offset could generate energy for long-wavelength surface waves. It can also result in lack of short-wavelength wave components due to the attenuation. For long offsets, where the distance traveled along the refractor exceeds several Rayleigh wavelengths, the head wave amplitude decreases by a factor close to the inverse square of the offset. At smaller offsets, which is likely to be the case for many LVLs (low-velocity layer or weathering surveys), the amplitude decrease is slightly less. In addition to the variation of amplitude with the offset, significant attenuation occurs if the refractor is thin (Press et al., 1954). This effect is normally associated with shingling, a phenomenon

characterized by a shift of energy to successively later cycles as the offset increases, producing an echelon pattern, as shown in Figure 3.7.

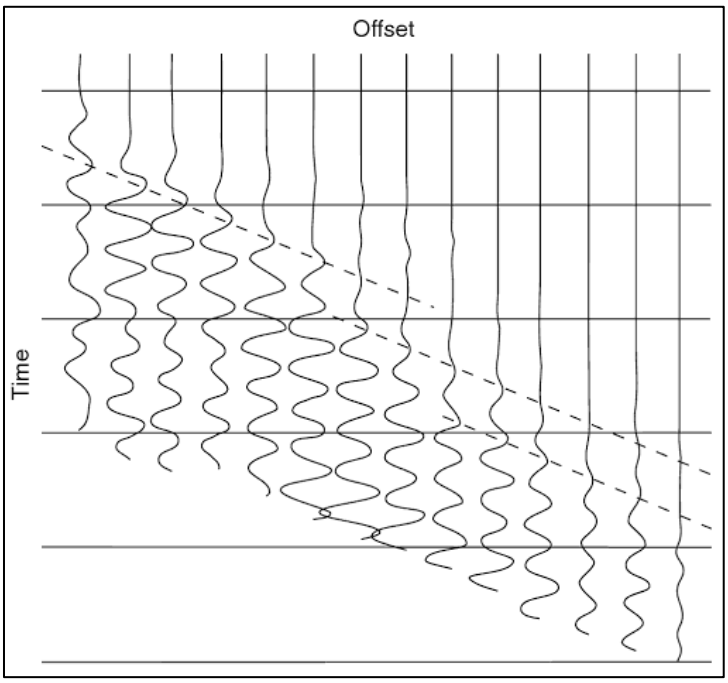

Figure 3.7. Refraction arrivals showing the shingling degree pattern often associated with layers.

The source offset needs to change in proportion to the intended maximum investigation depth, with a conservative calculation being that the source offset is equal to half of the maximum investigation depth (Park & Miller, 2005). The importance of choice of optimum offset is that it controls the degree of contamination by a range of near-field effects. Surface wave cannot fully develop before it strikes the first geophone in case of source positioned too close to the receiver spread. The risk of non-planar surface waves being picked up by the geophones can be minimized by carefully choosing the source offset (Park & Carnevale, 2010). The minimum source offset required to avoid near-field effects depends on the longest Rayleigh wavelength that is being analyzed

(λmax). In most cases, plane-wave propagation of surface waves first occurs when the source offset is greater than half of the longest Rayleigh wavelength (Park et al., 1999).

The source offset also needs to be sufficiently sized to extend to the primary depth range of interest. This concept conforms to the common practice with Equation 3.10 and 3.11:

$$X1 \geq 0.5D \tag{3.10}$$

when $$\lambda max \approx D \tag{3.11}$$

where D is the length of the receiver array. However, studies have shown that this criterion can be relaxed significantly for MASW surveys (Park et al., 1999, 2002; Park & Shawver, 2009).

Studies have shown that this criterion can be relaxed significantly for MASW surveys (Park et al., 1999, 2002; Park & Shawver, 2009). A long source offset, $X_1 \geq D$, can potentially enhance energy for long- Rayleigh wavelength wave components, thus increasing λmax for a receiver array of a given length (Park & Carnevale, 2010). However, such a long source offset can result in a lack of short- Rayleigh wavelength components, due to excessive attenuation (Park & Shawver, 2009). A long source offset, $X_1 \geq D$, can potentially enhance energy for long- Rayleigh wavelength wave components, thus increasing λmax for a receiver array of a given length (Park & Carnevale, 2010). However, such a long source offset can result in a lack of short- Rayleigh wavelength components, due to excessive attenuation (Park & Shawver, 2009). The suggested minimum (X_1, min) and maximum (X_1, max) source offsets for use in practice are as follows (Park, 2015):

$$X_1, \text{min} = 0.2D \quad \text{and} \quad X_1, \text{max} = D. \tag{3.12}$$

The optimum offset (A), based on a layered ground model due to the longer Rayleigh wavelength components of Rayleigh waves requires longer time or larger offsets to develop into plane waves (Zhang et al., 2004).

$$A = \frac{\lambda_{max} C_{R\,min}}{4\Delta C_R} \tag{3.13}$$

where λ_{max},$C_{R\,min}$, and ΔC_R are the longest Rayleigh wavelength, the minimum phase velocity of Rayleigh waves, and the difference between the maximum and minimum phase velocities, respectively.

For example, the first shot was acquired with the nearest source offset of 15ft, the longest Rayleigh wavelength of λmax = 500 ft/sec/25 Hz = 20ft, the minimum phase velocity of $C_R$min =180ft/sec and the difference between the maximum and minimum phase velocities of ΔC_R = 500ft/s - 180ft/sec = 320ft/sec. Therefore, the suggested optimum offset A would be 2.8ft.

3.2.3. Receiver Spacing. The receiver spacing (dx) is defines the shortest wavelength that can be analyzed and the shallowest resolvable depth of MASW survey. The minimum investigation depth λmin relates to the minimum distance between geophones (O'Neill 2003). This assumes that the maximum depth of penetration is approximately half of the maximum recorded Rayleigh wavelength (Park et al., 2009). The receiver spacing is related to the shortest Rayleigh wavelength (λmin) that can be included in a dispersion curve. In general, the receiver spacing should not be greater than half of the shortest Rayleigh wavelength in order to avoid spatial aliasing (Xia et al., 2009):

$$dx \approx \lambda min \approx Zmin$$

$$dx \leq 0.5\ \lambda min. \quad (3.14)$$

Moreover, the receiver spacing acts as a guideline for determining the minimum thickness (hmin) of the shallowest layer of the layered earth model used in the inversion analysis (Park et al., 1999; Xia et al., 2009). In other words,

$$h1 \geq hmin \approx dx \quad (3.15)$$

where h1 is the thickness of the topmost layer of the earth model.

The receiver spacing (dx) also determines the computational artifacts caused by the aliasing impact. It sometimes generates some curved streaks in the dispersion image, caused at the point of dispersion, where the Rayleigh wavelength becomes less than one-half of (dx).

3.2.4. Orientation. The orientation of the profiles should best depict the structures of the subsurface, which is as well important for the best possible interpretation. While interpreting the seismic data, well log data and result from previous geological surveys and studies of the region are often used in relation to the seismic data (Sheriff & Geldart, 1995). Furthermore, the effect spacing needs to be small in all orientation to avoid irregular surface. The subsurface coverage should be uniform with a consistency between the contribution of different source offsets and azimuths (Bacon et al., 2003).

Typically, there was a reasonable match between the two surveys from opposite orientations. If a survey in one orientation produced a poor quality and a difficult-to-extract dispersion curve, the survey in the opposite orientation generally produced a dispersion curve of similar quality, which is largely presumed to be a result of subsurface

lateral heterogeneities. Processing the data surveyed in both orientations helped limit the influence of disturbances.

To phrase it differently, both receiver spacing and source array methods can add additional orientation effects. Subsequently, comprehensively considering the parameters of the source array, the receiver spacing and the geometry in an acquisition system will lay a foundation for a high quality and highly efficient seismic survey project.

3.2.5. Topographical Conditions. Topographical conditions are known to have effect on the quality of the recorded surface wave data and therefore the quality of the resulting dispersion curves. They can also affect the quality of the acquired surface wave data and therefore affect the quality of the generated dispersion images (Zeng, Xia, Miller, Tsoflias, & Wang, 2012). For optimum results, the receivers should be placed on relatively flat terrain, suitable for Active MASW, as shown in Figure 3.8 (A) and 3.8 (B).

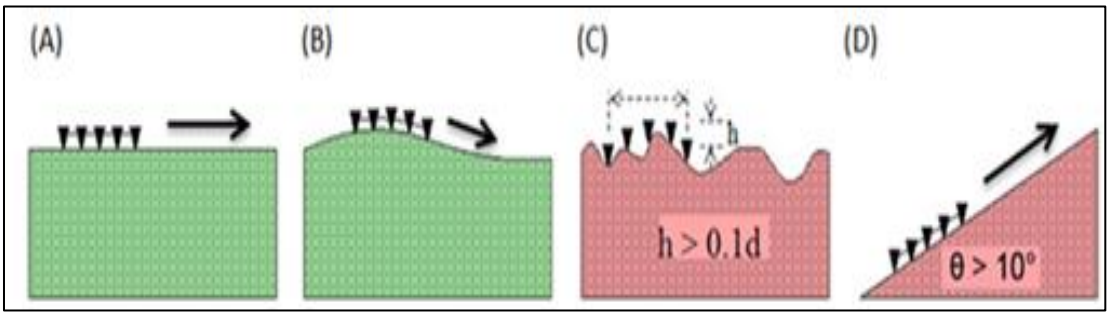

Figure 3.8. Topographical conditions are found to have an effect on the quality of the recorded multichannel surface wave data. Receivers should be placed on relatively flat terrain for optimum results (A & B). Surface reliefs greater than 0.1d and the recorded data (C & D). Adopted from Park (2015).

Surface reliefs within the receiver spread greater than 0.1 d can have a significant effect on the generation of surface waves (Park, 2015), as shown in Figure 3.8 (C), and

should therefore be avoided. The slope of the surface along the receiver spread can also affect the quality of the surface wave records, as shown in Figure 3.8 (D).

However, topography can also interfere with surface wave propagation. Results of numerical investigations presented by Zeng et al. (2012) indicated that the slope of the topography along the survey profile (θ) should preferably be less than 10º. A steeper topography (i.e., a slope angle $\theta > 10^{\circ}$) can lead to significant errors (greater than 4%) in estimation of the Rayleigh wave dispersion characteristics (Zeng et al., 2012).

In theory, maximum investigation depth is defined by the longest surface wave wavelength generated during the data acquisition. On practice, the maximum investigation depth also depends on the survey site and type (strength) of seismic source. A heavier source provides increased investigation depth. For example – the use of 20 lb. sledgehammer typically results in 30 – 100ft. (10 – 30m) depth of investigation. Recent studies reported that use of non-metallic plate placed in the impact point can generate stronger energy at the lower frequency part of surface waves than a conventional metallic plate (Cui, 2013). Also, the maximum investigation depth is determined by the longest Rayleigh wavelength that is obtained during data acquisition.

Recording frequency of 1000 Hz (sampling interval of 1ms) is most commonly used in active MASW surveys. The total recording time of 1 second is usually used for the impulsive seismic source MASW surveys.

3.2.6. Resolution of MASW Data. Another important thing to consider is the desired resolution of MASW data. Resolution is mostly a function of the receiver spacing, which is directly related to the shortest wavelength and therefore determines the shallowest resolvable depth of investigation. The total length of the receiver spread is

directly related to the longest wavelength that can be analyzed, which in turn defines the maximum depth of investigation. The source offset distance controls the possible degree of contamination by the near-field effects (surface waves are formed through interference of body waves generated from reflections and refractions, so they require to propagate a certain minimum distance from the source to fully develop, which may result in both underestimation or overestimation of Rayleigh wave phase velocity due to the body waves contamination near to the source). Vertical stacking with multiple impacts can suppress ambient noise significantly, producing a high signal to noise ratio. This is good in surveys in urban areas. Three to five vertical stacks are recommended during survey.

3.3. MULTICHANNEL ANALYSIS OF SURFACE WAVES DATA PROCESSING

Various component frequencies of Rayleigh waves involve particle motion at various depths. For example - the lower frequencies involve particle motion at greater depths. So the different component frequencies of Rayleigh waves exhibit different phase velocities. The whole MASW technique is based on the relationship between the Rayleigh wave phase velocities and the depth-range of associated particle motion.

The quality of the acquired surface wave records can be evaluated in terms of the resolution of the phase velocity spectrum, i.e., the sharpness of the amplitude peaks observed at each frequency, the extractable frequency range and the continuity of the fundamental mode high-amplitude band.

The quality of the MASW data can also be affected by natural geologic conditions that may not produce well-defined dispersion curves and cannot be used to calculate reliable shear-wave velocity models.

After data acquisition, field records are analyzed using SurfSeis software developed by Kansas Geological Survey (KGS). In order to convert seismic record to an estimate of shear wave velocity, three crucial steps must be performed: generation of dispersion image (overtone - a graphic representation of intensity in phase velocity and frequency space) and extraction of the fundamental-mode dispersion curve from it. The software calculates phase velocities for each component frequency of recorded MASW data to generate the resultant dispersion image to extract the dispersion curve. Then, the curve is inverted using a least–squares approach to generate a vertical shear-wave velocity profile. Basically, software performs wavefield transformation from offset-to-time domain into phase velocity-to-frequency domain (multichannel record, time-space domain, to dispersion image, frequency-phase velocity domain). Then MASW data are being inverted to generate 1-D (depth) shear wave velocity profile. Figure 3.9 displays the raw seismic record, dispersion curve extracted from the overtone image, and the resulting shear wave velocity profile.

3.3.1. Dispersion Analysis. The intent of dispersion analysis is to estimate one or more dispersion curves that are in turn passed into the next step of inversion process. The following are the most influential factors affecting the dispersion analysis:

1. Frequency range for depth of investigation,
2. Approximate phase velocity range,
3. Easy characterization of higher modes, and
4. Identification and reduction of noise events.

The influence of these factors on the analysis is highly dependent on the data quality (signal-to-noise ratio, S/N). A “good” quality data set suggests that surface-wave

is the most prominent seismic event (with highest S/N), whereas a “bad” quality data set is usually contaminated by noise. In the dispersion curve analysis, the fundamental mode surface waves are the signal, and everything else is noise. Noise includes all higher-mode surface waves as well as all body wave events.

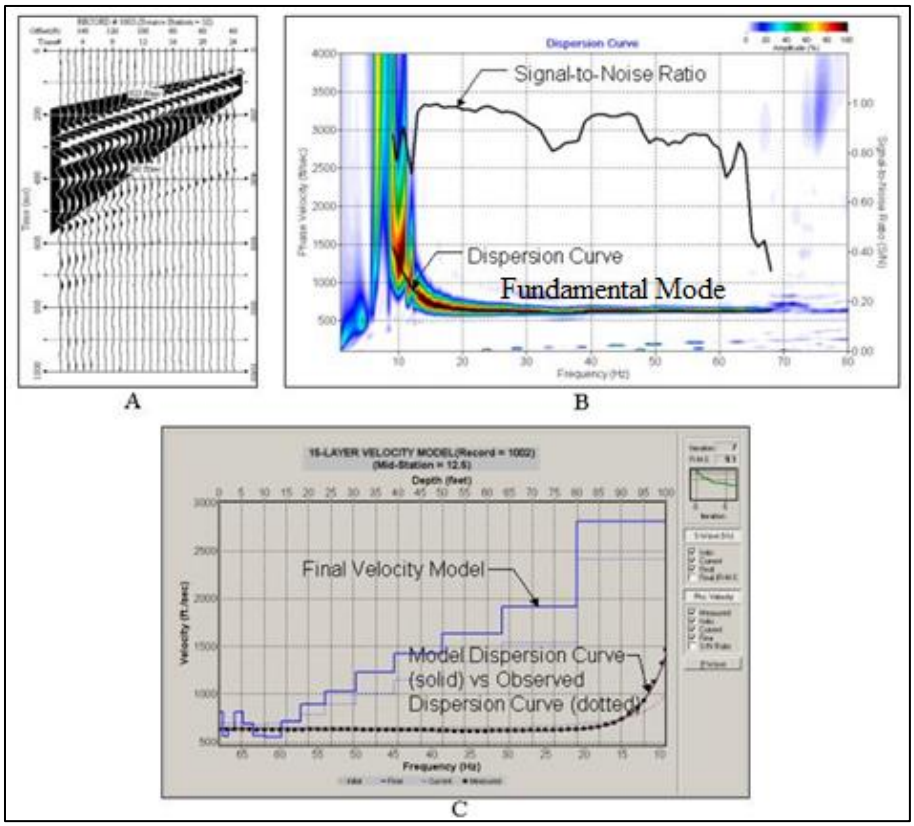

Figure 3.9. (A) Acquisition seismic time series data; (B) Dispersion curves extraction frequency and phase velocity; and (C) 1-D shear-wave velocity profiles Vs. 1-D depth curve (http://www.kgs.ku.edu/software/surfseis/gifs/masw).

Software also performs evaluation of an approximate phase velocity range for the surface waves. It generally ranges from as low as 650ft/sec (or 200m/sec) to as high as 2,500ft/sec (760m/sec) depending on the material type. This information is used by the program to initiate the analysis by searching within this range for a phase velocity

corresponding to a certain surface wave frequency with the greatest coherence throughout the entire range of offset and the highest signal-to-noise ratio which is indicative of a high confidence in the acquired phase velocity (Figure 3.9). The SurfSeis software calculates phase velocities within the specified frequency range. This calculation can be run multiple times using different values and varieties of parameters, examining the output curves until an optimum solution is identified. In general, the curve with the highest signal-to-noise ratio (S/N) represents the best option. The quality of a dispersion curve is judged according to two criteria: the signal-to-noise ratio (S/N) and the general dispersion curve direction.

The next processing step is an extraction of a fundamental-mode dispersion curve from the dispersion image. This extracted curve is called a "measured" dispersion curve that is an input data to the next data analysis step (inversion). The quality of the acquired surface wave records can be evaluated in terms of the resolution of the phase velocity spectrum, i.e., the sharpness of the amplitude peaks observed at each frequency, the extractable frequency range and the continuity of the fundamental mode high-amplitude band. The quality of a dispersion curve is judged according to two criteria: the signal-to-noise ratio (S/N) and the general dispersion curve direction. The quality of the ‘match’ between the two curves is evaluated on the root-mean-square error (Xia et al., 1999). The inversion of a dispersion curve using SurfSeis Software is particularly straightforward, as it is a fully automated process that removes any human error incurred during the calculations.

3.4. MULTICHANNEL ANALYSIS OF SURFACE WAVES DATA INTERPRETATION

Data interpretation of MASW involves the analysis of the variations of the shear wave velocities with depth with a goal to transform the output velocity model into a geologic model of the subsurface.

Interpretation of the subsidence features in karst terrain environment is difficult because of the inherent complexity of the subsurface and the resolution limits of MASW technique. Shear wave velocity models can clearly show the low-velocity zones, which can be interpreted as sinkholes, voids, fractured bedrock, or naturally in-filled collapsed features.

In Missouri for example, the shear wave velocity value used to determine the depth to top of bedrock is mostly 1000ft/sec. but can vary. Again, highly stiff earth materials have relatively high shear wave velocities compared to fractured or weak earth materials (Table 3.1).

Reliability of output shear-wave velocity data decreases as lateral and vertical heterogeneity of soil/rock increases. Therefore, site conditions should be considered; the immoderate dip of the subsurface layer along the survey line (more than about 10 percent), disadvantageous topography, or known high lateral variability in soil or rock properties may be reasons to reject field data as inconvenient for interpretation in terms of simple vertical variation of subsurface.

Table 3.1. Shear wave velocity (Vs) of some earth materials (National earthquake hazards reduction program).

Earth Material	Shear-wave velocity (Vs) (ft/sec)	Shear-wave velocity (Vs) (m/sec)
Hard Rock (A)	> 5,000	> 1,500
Rock (B)	2,500-5,000	760-1,500
Very Dense Soil and Soft Rock (C)	1,200-2,500	360-760
Stiff Soil (D)	600-1,200	180-360
Soft Clay Soil (D)	< 600	< 180
Soils requiring additional response (F)	< 600, and meeting some additional conditions	< 180, and meeting some additional conditions

3.5. ELECTRICAL RESISTIVITY TOMOGRAPHY (ERT)

3.5.1. Overview. Electrical Resistivity Tomography (ERT) is a nondestructive geophysical technique based on the electrical resistivity method. ERT has been used for decades as an effective environmental and geotechnical tool. In particular, ERT methodology is widely used for determining the maximum depth of rock, acquiring information on the elevation of soil, the top of rock, etc. This method is especially preferred for vision characterization in karst terrain (Zhou, 1999).

The purpose of an electrical resistivity survey is to determine the subsurface resistivity distribution in karst characteristics, such as caves, that may or may not be easily recognizable on the subsurface. Areas where the top of rock is limestone or gypsum, like it is in Missouri have a high probability of karst development. Karst areas commonly lack surface water and have numerous streambeds that are dry except during

periods of high runoff. When an electrical resistivity tomography survey is conducted in karst terrain, current flow is generally assumed to be electrolytic rather than electronic.

Surface electrical resistivity surveying is based on the principle that the partition of electrical potential on the subsurface around a current-carrying electrode depends on the soil's materials and rock to demonstrate the variations in their electrical resistivity because of the variations in their mineral content, permeability, fluid saturation, porosity, etc. After that, areas of the subsurface undergoing dissolution can be differentiated from the top of rock by measuring the resistivity of the subsurface in good resolution.

3.5.2. Ohm's Law and Resistivity. The fundamental principle behind the combination and interpretation of electrical resistivity measurements was created in the electrical physical theory of Ohm's law. Ohm's law, Equation 3.16, states that the product of the electrical current, I, and the resistance of the wire, R, through which the current passes is equivalent to the potential difference, V, across the conductor:

$$V = IR \tag{3.16}$$

According to Gibson and George (2003), this relationship is best represented by envisioning a current passing through a thin wire. The expounded application of Ohm's law has made this relationship a capstone concept in the study of electrical theory. Units for electrical potential, current and resistance are volts, amperes and ohms, respectively. As indicated, the conductor element can be tangibly described as a wire element.

The resistance of the wire is related to both the geometric shape and material attributes of the wire. The geometry of the wire is typically cylindrical, possessing a length and cross-sectional area, and is made of a conductive material. The total resistance

of the wire element, R, is the product of the material resistivity, ρ, and the ratio of the wire length and cross-sectional area:

$$R = \rho\,(L/A). \tag{3.17}$$

Considering the physical relationship between the geometry of the conductor and the material property, Equation 3.16 can be manipulated to from Equation 3.17 to determine the material resistivity of the conductor element.

This form states that the units for resistivity depend on the volume of the space through which the current travels. Typical units for resistivity, ρ, include ohm-meters and ohm-centimeters (Gibson & George, 2003).

In a similar situation, the measurement of the potential difference can be related to the dissipation of the electrical current within an infinite, homogenous half-space. In this instance, the application of an electrical current travels in radial fashion out from the point of origin. During the current application, the resistance at any location away from the source point within the homogeneous mass can be found by determining the radius from the point of origin and the surface area of the respective hemispherical equipotential surface. Relating this model to the original wire example, Equation 3.17 can be rewritten using the radius, r, as the distance for which the current travels and the surface area of the resulting equipotential surface, $2\pi r^2$.

$$R = \rho(r/2\pi r^2) = (\rho/2\pi r) \tag{3.18}$$

Equation 5.4 describes the system resistance at any point away from the source point within the homogeneous mass. Using the resistance term from the mentioned homogeneous earth model, Equation 3.19 relates the resistance of the earthen model to Ohm's law:

$$V = IR = I\,(\rho/2\pi r) \tag{3.19}$$

where

U = potential, in V,

ρ = resistivity of the medium, and

r = distance from the electrode.

Likewise, the potential difference between any two points within the homogeneous mass would be the difference between the two equipotential surfaces, as expressed in Equation 5.5 (Gibson & George, 2003):

$$U = \frac{\rho\, I}{2\pi\, rA} - \frac{\rho\, I}{2\pi r\, B} = \frac{\rho\, I}{2\pi}\left[\frac{1}{r\, A} - \frac{1}{r\, B}\right] \tag{3.20}$$

where

rA and rB = distances from the point to electrodes A and B

Equation 3.21 relates the applied current, I, and measured potential difference, V, to a constant value that accounts for spatial considerations, or the way in which the reading was acquired. This model, a concept of equipotential surfaces, and means of measuring potential differences between various surfaces, is fundamental in the interpretation of collected field data (Gibson & George, 2003).

$$\rho = (2\pi U/I)\,[1/\,[(1/ra)-(1/rb)] \tag{3.21}$$

Figure 3.10 explains the electric field around the two electrodes regarding equipotential and current lines. The equipotential represents the imagery projectiles or bowls surrounding the current electrodes where the electrical potential is equal on each one. The current lines represent a sampling of the infinite paths followed by the current, which are defined by the condition that they must be everywhere and normal to the equipotential surfaces.

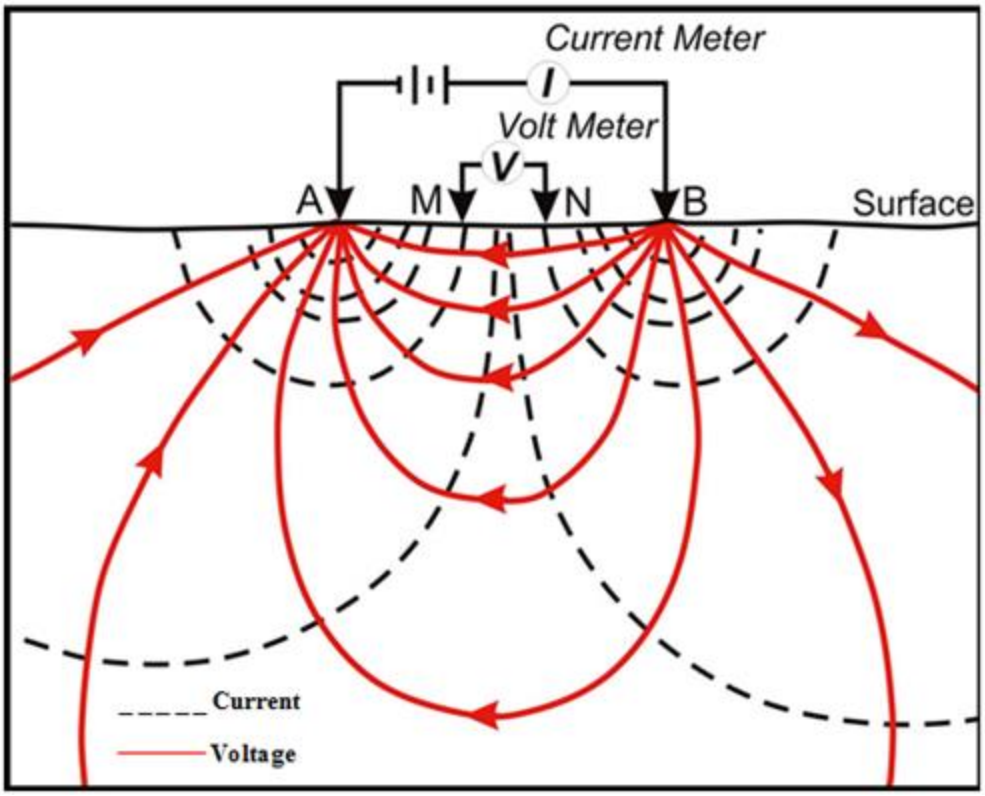

Figure 3.10. Equipotential and current lines for a pair of current electrodes, A and B, in a homogeneous half-space.

In a homogenous condition, the measured resistivity will be equivalent to the real value of resistivity at a given location within the media. However, the occurrence of a homogenous condition is rare in practice, if not nonexistent. A collected reading is considered an apparent resistivity measurement in order to account for the inherent heterogeneity of the subsurface. Visual resistivity is the resistivity of a theoretical, homogeneous half-space that complements the measured current and potential difference for a particular measurement scheme (United States Corps of Engineers, 2001). Mostly, the obvious resistivity value is an average reading of the energized soil mass engaged during the measurement. Numerically, the obvious resistivity can be expressed by Equation 3.22:

$$V = UM - UN = \frac{\rho I}{2\pi}\left[\frac{1}{AM} - \frac{1}{BM} + \frac{1}{BN} - \frac{1}{AN}\right] \quad (3.22)$$

where

UM and UN = potentials at M and N, and

AM = distance between electrodes A and M, etc.

These distances are always the actual distances between the respective electrodes, whether or not they lie on a line. The quantity of the brackets, S is a function only of the various electrode spacing. The quantity is denoted by 1/K, which allows the equation to be rewritten as:

$$V = \frac{\rho I}{2\pi}\ \frac{1}{K} \quad (3.23)$$

where

K = the array geometric factor.

Equation 3.24 can be solved for ρ to obtain

$$\rho = 2\pi K\ \frac{V}{1}. \quad (3.24)$$

The resistivity of the medium can be established from the measured values of V, I and K, the geometric factor. The variable K is a function only of the geometry of the electrode arrangement.

When these measurements are made over real heterogeneous earth, as distinguished from the fictional homogeneous half-space, the symbol ρ is replaced by ρa for apparent resistivity. The resistivity surveying problem is reduced to its essence. The use of apparent resistivity values from field monitoring at various locations, and with various electrode configurations, is designed to estimate the actual resistivity of several earth materials present at a site and to locate their confines spatially below the surface of the site.

An electrode array with stationary spacing is used to investigate the lateral changes in apparent resistivity, reflecting the lateral geologic variability or localized anomalous features. The size of the electrode array is varied as we investigate how changes in resistivity affect depth.

The resistivity is clearly affected by a material at increasing greater depths (hence the larger volume) as the electrode spacing is increased. Because of this impact, a plot of apparent resistivity against electrode spacing can be used to signal vertical variations in resistivity.

The geometric coefficient, K, varies with array types. The spacing and layout of the current and potential electrodes impact the induced equipotential fields created within the earthen mass. The geometric factor for a general four probe system can be derived from Equation 3.21(Gibson & George, 2003).

3.5.3. Relationship between Geology and Resistivity. Electric current flows in subsurface materials at shallow depths through two main methods. They are electronic conduction and electrolytic conduction. In electronic conduction, the current flow is via free electrons, such as in metals. In electrolytic conduction, the current flow is via the motion of ions in groundwater. In engineering and environmental surveys, electrolytic conduction is the more common mechanism. However, electronic conduction is important when conductive minerals are present, such as metal sulfides and graphite in mineral surveys.

The resistivity of common rocks, chemicals, and soil materials (Keller & Frischknecht, 1966: Daniels & Alberty, 1966: Telford et al., 1990) is shown in Figure 3.11. Igneous and metamorphic rocks typically have elevated resistivity values. The

resistivity of these rocks is greatly dependent on the degree of fracturing and the percentage of the fractures that are filled with groundwater. Thus, a given rock type can have a large range of resistivity, from about 1000 to 10 million Ω·m, depending on whether it is wet or dry. This characteristic is useful in the detection of fracture zones and other weathering features, such as in engineering and groundwater surveys.

Sedimentary rocks, which are usually more porous and have higher water content, normally have lower resistivity values compared to igneous and metamorphic rocks. The resistivity values range from 10 to about 10000 Ω·m, with most values below 1000 Ω·m. The resistivity values are dependent on the porosity of the rocks and the salinity of the contained water.

Unconsolidated sediments generally have even lower resistivity values than sedimentary rocks, with values ranging from about 10 to less than 1000 Ω·m. The resistivity value is dependent on the porosity (assuming all of the pores are saturated) as well as the clay content. Clay soil normally has a lower resistivity value than sandy soil. However, one should note the overlap in the resistivity values of the different classes of rocks and soils should be noted. This is because the resistivity of a particular rock or soil sample depends on a number of factors, including the porosity, the grade of water saturation, and the concentration of dissolved salts. The resistivity of groundwater varies from 10 to 100 Ω·m, depending on the concentration of the dissolved salts (Loke el al., 2011).

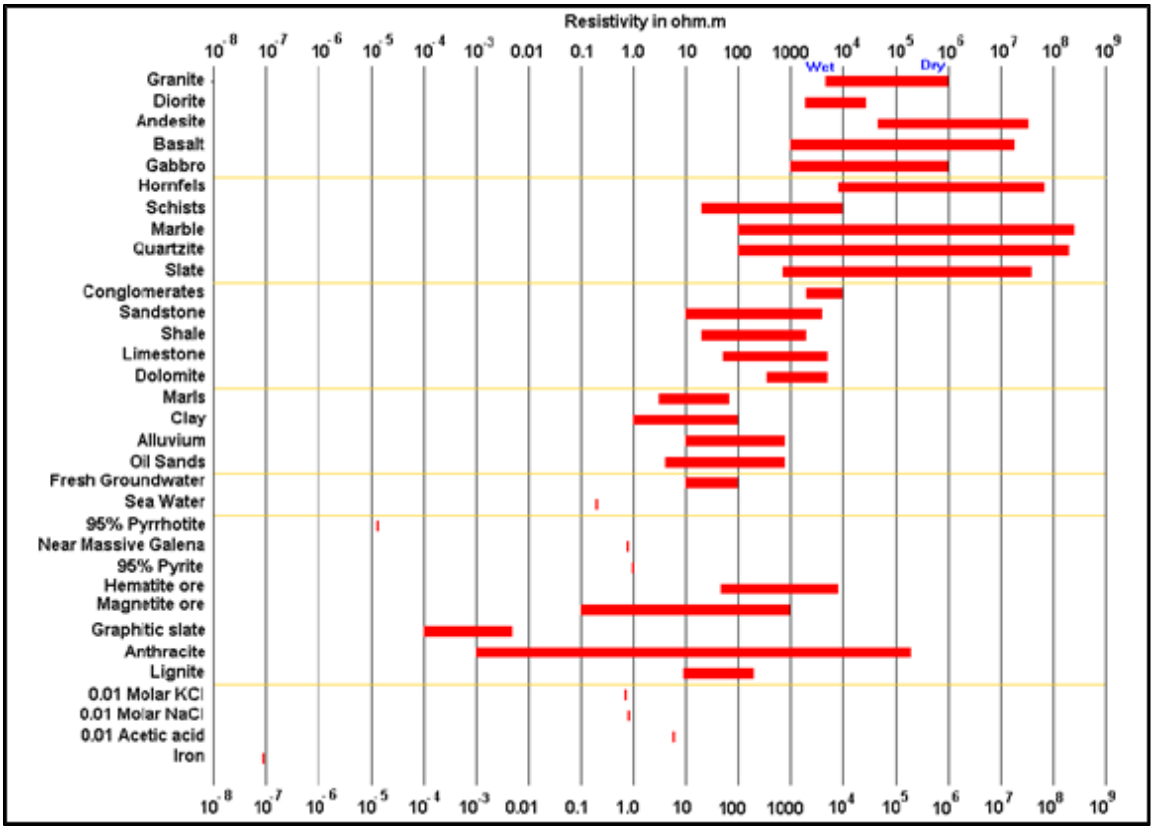

Figure 3.11. The resistivity of rocks, soils, and minerals (Keller & Frischknecht, 1966; Daniels & Alberty, 1966; Telford et al., 1990).

3.5.4. Electrical Resistivity Array Configuration. In theory, soil resistivity could be measured by using a single current source and receiver element. In practice, this is not feasible due to the contact resistance between the earth and the electrode pair. To overcome this phenomenon, four electrodes are used for measurement: two electrodes provide current to the subsurface and two electrodes measure the potential difference between the earth materials (Milson, 1996). Current electrodes are identified as C1 and C2 (or A and B), and potential electrodes are identified as P1 and P2 (or M and N) (Loke, 2000), as shown in Figure 3.12.

The types of electrode arrays that are most commonly used are Wenner (Figure 3.12a, Schlumberger (Figure 3.12b), pole-dipole (Figure 3.12c) and Dipole-Dipole

(Figure 3.12d). Other electrode configurations are either used experimentally, on non-geotechnical problems, or are no longer popular. Some of these include the Lee, half-Schlumberger, Polar Dipole, and gradient arrays.

In any case, the geometric factor for any four-electrode system can be found from Equation 3.22 and can be advanced for more complicated systems by using the rule illustrated in Equation 3.20. It can also be seen from Equation 3.25 that the current and potential electrodes can be interchanged without affecting the results; this property is called reciprocity (Milson, 1996). For the purpose of this research, the discussion will concentrate on the Dipole-Dipole array, which was used during these studies.

Unlike to the Wenner and Schlumberger arrays, the configuration of the Dipole-Dipole array does not place the potential electrode pair inside the current electrode pair. Current and potential electrode pairs have common interior spacing and are separated by a distance ten times the internal spacing of the electrode pair. The Dipole-Dipole array is ordinarily used for performing tomography survey due to the array's ability to resolve lateral variations. In comparison to the Wenner and Schlumberger arrays, the Dipole-Dipole array has a weak signal and is more susceptible to the effects of ambient or cultural, noise.

If the division between both pairs of electrodes is the same, a, and the division between the centers of the Dipoles is restricted to a (n+1), the resistivity is given by

$$\rho a = \pi a \pi (n+1)\,(n+2)\,\frac{V}{1}. \qquad (3.25)$$

3.5.5. Wenner Array. The Wenner array is described by the equal spacing between all four electrodes. The two current electrodes, C1 and C2, are placed on the outside of the array during which the potential electrodes, P1 and P2, reside inside of the

array. The potential measurements are possessed at the mid-span of the potential electrodes at a depth of approximately 0.5 to 1.0 times the electrode spacing (also known as the spacing). Different depth measurements are made by varying the period spacing of the array, as shown in Figure 3.12a.

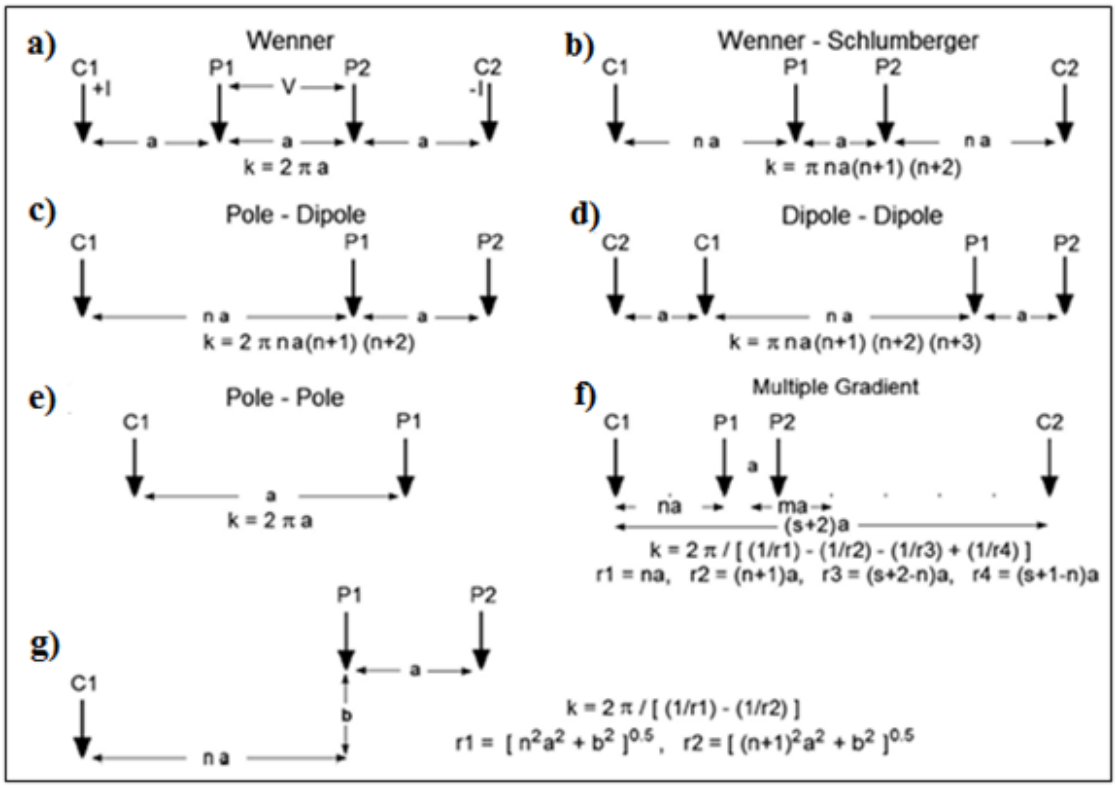

Figure 3.12. These are some commonly used electrode arrays and their geometric factors. Note that for the multiple gradient arrays, the total array length is‘(s + 2) an’, the distance between the center of the potential Dipole pair is P1-P2 and the center of the current pair C1-C2 is given by ‘ma.’ 'British Geological Survey (c) NERC 2013. K = Geometric Factor.

In an exemplified homogeneous earth model, the sensitivity of the Wenner array provides a pattern with strong horizontal layering immediately below the potential electrode pair. Because the focus of vertical electrical sounding (VES) is to differentiate between horizontal layering beneath a common point, the Wenner array is a practical

array for this application. The high signal of the Wenner array also makes the array suitable for use in noisier environments (Loke, 2000).

3.5.6. Schlumberger Array. The Schlumberger array is arranged with two current electrodes on the outside of the array, set apart by a distance of at least five times the space between the two interior potential electrodes. The potential difference measurement is believed to show incorrect at the mid-span of the potential internal electrodes, at a depth of approximately one-half of the length between the current external electrodes. Similar to the Wenner array, the Schlumberger array provides a high signal directly below the potential electrode pair, as shown in Figure 3.12b.

The Schlumberger array is preferred for VES applications due to the strong horizontal resolution and ease of setup in the field. As compared to the Wenner array where all four electrodes must be repositioned after each test,

The Schlumberger array is preferred for VES applications due to its strong horizontal resolution and ease of setup in the field. As compared to the Wenner array, where all four electrodes must be repositioned after each test, the Schlumberger array only requires that the two exterior current electrodes be moved to acquire a new measurement. The potential interior electrodes are moved only as the current electrodes are spaced beyond the practical limits of the survey. That movement occurs when the ratio between the potential electrode spacing and the space between the exterior current electrode and positional electrodes in the mid-span is greater than 0.4 (United States Corps of Engineers, 1995).

3.5.7. Dipole-Dipole Array. The Dipole-Dipole array is logistically the most appropriate in the field, particularly for large spacing and for 2-D imaging. The

convention for the Dipole-Dipole array shown in Figure 3.12d is that the current and voltage electrode spacing are the same, a, and the spacing against them is an integer multiple of a. The Dipole-Dipole array is usually used for performing tomography surveying due to the array's ability to resolve lateral variations. For a comparison against the Wenner and Schlumberger arrays, the Dipole-Dipole array has a weaker signal and is very susceptible to the effects of ambient, or cultural, noise. The apparent resistivity reading recorded using the Dipole-Dipole array represents a condition present at the mid-span of the array length that occurs at a depth amounting to one-half the product of the Dipole electrode spacing, a, and one plus the separation factor (n+1).

3.6. ELECTRICAL RESISTIVITY TOMOGRAPHY DATA ACQUISITION

ERT data are typically acquired with the use of resistivity meter. Resistivity meter is connected to the electrode cables, and the electrode cables are attached to metal stakes pounded to the ground using rubber-band. In some instances, it is essential to water the ground in proximity of the metal electrode to ensure a good contact between the metal stake and ground. Newer resistivity meters are equipped with multiple channels, which allows multiple electrodes to be engaged and measurements to be taken through each channel. For instance, the SuperSting R8 resistivity meter, produced by Advanced Geosciences, Inc., is equipped with eight channels. Subsequently, the system engages nine electrodes to collect eight different potential difference measurements for each current injection (Advanced Geosciences, Inc., 2006).

Planning and preparation are a significant part of ERT survey. Desired depth of investigation, acquisition time, data resolution must be considered prior to each ERT

survey. The sequencing information considers the array style and information pertaining to the electrode locations (or electrode address) during each measuring sequence. There are no theoretical limits to the depth of penetration. Therefore, as the electrode spacing increases, the signal strength decreases. At a certain electrode separation distance, the signal strength is too low to provide reliable measurements of the potential difference. Practical limits should be instilled that consider the signal strength of the particular array type and equipment ability. Advanced Geosciences, Inc., (2008) suggested that when considering depth of penetration for tomography applications, practitioners can generally assume that the depth of penetration is approximately 15 to 25 % of the length of the electrode spread. The survey resolution is also related to electrode spacing.

Coskun (2012) recommends the commonly used Dipole-Dipole array because it offers better lateral and vertical resolutions than the other arrays. It is also worth noting that the data acquisition time for a Dipole-Dipole array using 72 electrodes is typically 45minutes, and around 2 hours and 3 hours for 84 electrodes, and 168 electrodes, respectively after survey set-up. Loke (1999) shares a similar view as Coskun, adding that the Dipole-Dipole array is more suitable for investigating karst terrain because of its ability to detect sharp changes in bedrock topographies.

Current practices propose that the electrode spacing should not be greater than twice the size of the object or feature to be imaged. The design of the survey (i.e., survey run length, electrode spacing, and array type) directly impacts the depth of penetration and resolution (Advanced Geosciences Inc., 2008). It is not always possible or practical to image a survey line or area in one deployment of electrodes. However, this can vary depending on the preference between the resolution and imaged depth. Typically,

increasing the electrode spacing will increase the imaged depth and reduce the resolution of the section and vice versa. However, it is often recommended that if the desire is to increase the imaged depth, more electrodes should be added to the section instead of increasing the electrode spacing. To continue a survey after completion of the initial data collection, electrodes may be configured to collect additional data along a common survey line or area, using roll-along survey techniques (Loke 2000), as shown in Figure 3.13.

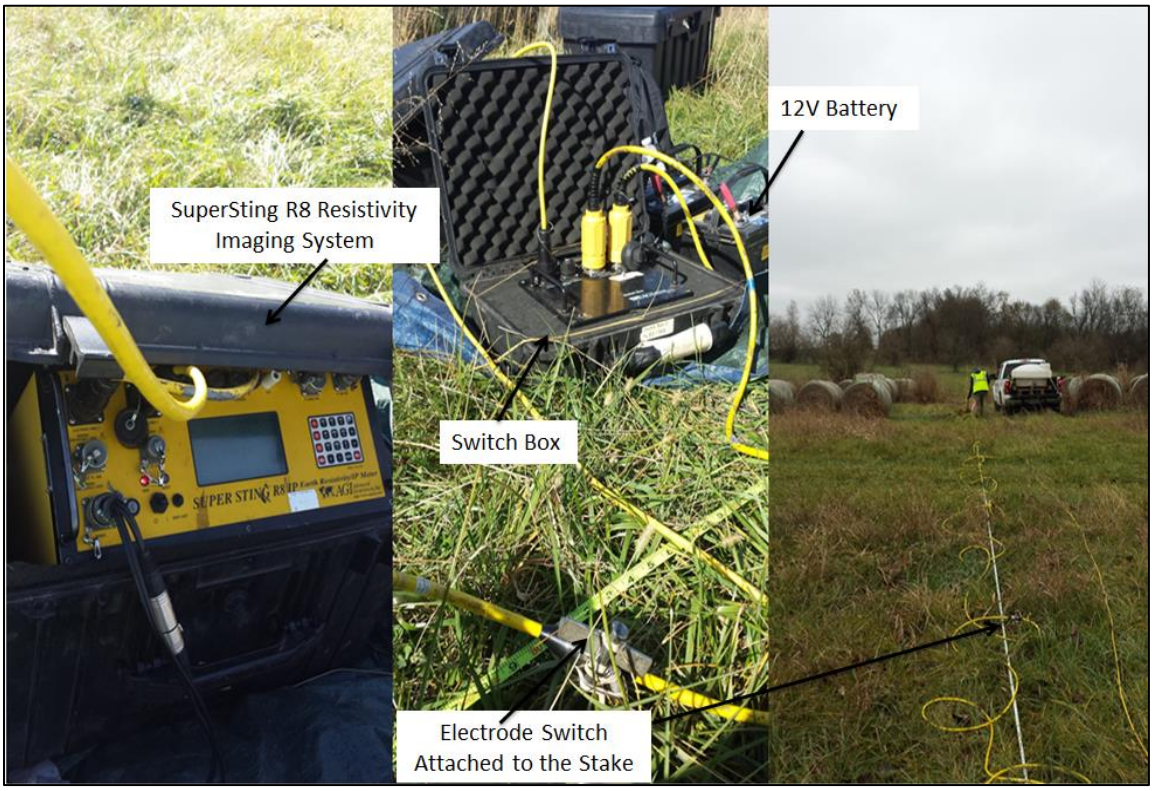

Figure 3.13. SuperSting R8/IP resistivity (left). Switch Box (AGI) connecting passive cables (middle). ERT field setup (right).

3.7. ELECTRICAL RESISTIVITY TOMOGRAPHY DATA PROCESSING

After data acquisition, the raw data are typically transferred to the laptop for processing. During data processing inversion software transforms the apparent resistivity values measured from the field to true resistivity by applying backward and forward modeling in a process called inversion. There are a variety of processing software available these days, including RES2DINV (Geotomo), Earth Imager (AGI), ZondRes2D (Zond), etc. In this study, Res2DInv is used for ERT data processing. The RES2DINV program uses the cell-based method in which the model parameters are the resistivity values of the model cells, and the data provides the measured apparent resistivity values (Loke, 2011). The mathematical link between the model parameters and the model response for the 2-D and 3-D resistivity models is provided by either the finite-difference (Dey & Morrison, 1979) or finite-element methods (Silvester & Ferrari, 1990).

The ERT data processing involves two main steps. The first step is to the inspection of the resistivity data sets for the presence of any points that have anomalously high or low apparent resistivity values, called “bad data points”, and subsequently removing them when necessary (Figure 3.14b). Bad data points can be a result of several factors, such as the failure or malfunction of equipment during the survey and very poor electrode subsurface contact due to dry soil or shorting across the cable caused by very wet subsurface conditions.

The second step is to run an inversion of the data. The inversion involves some iterative calculations and the generation of a 2-D resistivity image of the subsurface to represent the actual resistivity of the sections. The final result of the inversion is a 2-D resistivity image of the subsurface showing the distribution of resistivity across a profile.

Additionally, pseudo section can be displayed and shows distribution of apparent resistivity values (Figure 3.14a).

The root-mean squared (RMS) error is used to measure the difference between calculated and measured apparent resistivity values. In practice, the lower the error, the better the data quality is. However, the model with the low RMS error can sometimes show unrealistic variations in the model resistivity values, and might not be best model from geological perspective. A careful approach is to choose the model at the iteration after which the RMS error does not change significantly. According to Loke (1999), an RMS error of 5% is recommended for a geologic model of good quality.

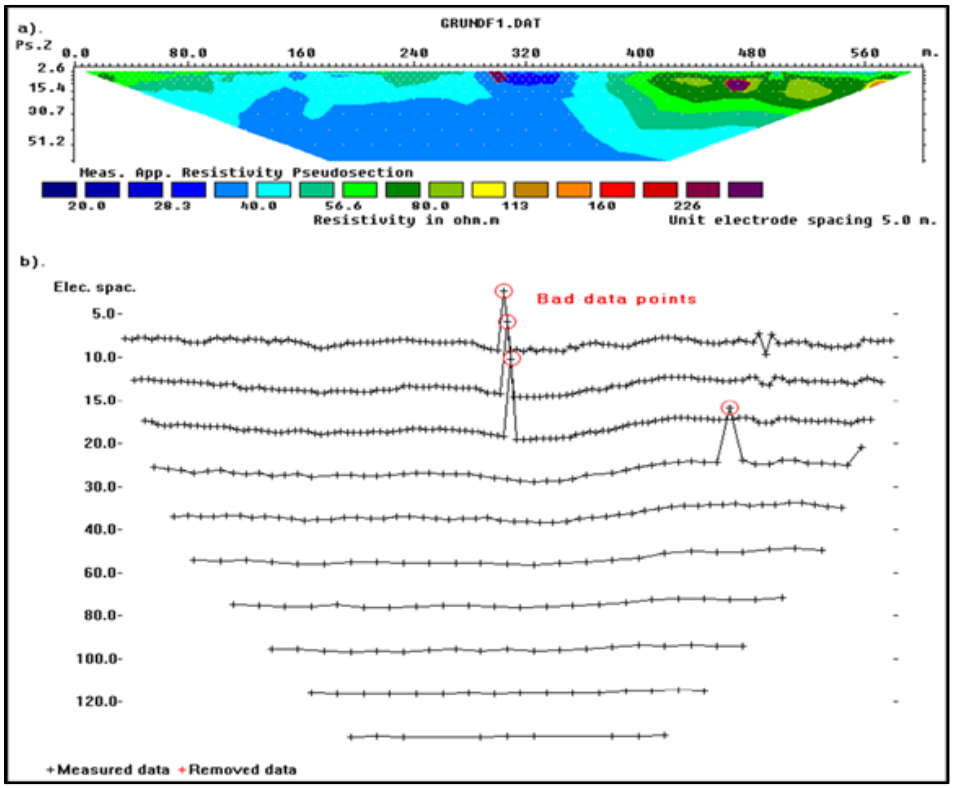

Figure 3.14. An example of a field data set with a few bad data points. The apparent resistivity data in (a) pseudosection form and in (b) profile form. (Loke, 1999).

3.8. ELECTRICAL RESISTIVITY TOMOGRAPHY DATA INTERPRETATION

The interpretation is based on the inverse model generated form the inversion software, RES2DINV. The chart showing colors with various ranges of resistivity is used to estimate the resistivity of the imaged subsurface earth materials.

Factors such as porosity, conductivity, saturation, salinity, clay content, lithology and temperature can affect the ability of different materials to conduct electrical current. Accordingly, materials of the same mineral content may exhibit different resistivity values. For example, both the top-of-rock limestone and air-filled voids typically are characterized by high resistivity values ranging from 50 ohm-m to 107 ohm-m., which can be seen in Table 3.2. When an air-filled void is entirely embedded in limestone, it usually cannot be easily detected on the resistivity data because of low resistivity contrast.

Furthermore, dry soil usually has a much higher resistivity than saturated soil. The same situation appears with weathered and un-weathered rock. Weathered rock is usually more porous and fractured, and it becomes more saturated with groundwater; as a result, weathered rock has a lower resistivity than un-weathered/the top of rock.

Table 3.2. Resistivity of common earth materials (Robinson, 1988).

Earth Material	Resistivity, Average or Range (Ohm-m)	Earth Material	Resistivity, Average or Range (Ohm-m)
Granite	10^2-10^6	Sandstone	1-10^8
Diorite	10^4-10^5	Limestone	50-10^7
Gabbro	10^3-10^6	Dolomite	10^2-10^4
Andesite	$10^{2\text{-}}10^4$	Sand	1-10^3
Basalt	10-10^7	Clay	1-10^2
Peridotite	10^2-10^3	Brackish water	0.3-1
Air	~ 0	Seawater	0.2

According to previous studies (Torgashov, 2012) conducted in southwest Missouri, typical resistivity values for the subsurface materials are characterized as follows:

- Moist clays in southwest Missouri are normally characterized by low resistivity values, usually less than 100 ohm-m, and may vary due to different degrees of saturation, porosity, and layer thicknesses.
- Moist soils and intensively fractured rocks intermixed with clay typically have resistivity values between 100 and 400 ohm-m. Such variation is explained by different porosity, saturation, clay content and layer thicknesses.
- Relatively top-of-limestone with minimal clay content is characterized by higher resistivity values, typically more than 400 ohm-m. Resistivity values of the top of limestone may vary due to varying layer thickness, moisture content, porosity, saturation, and impurities.
- Air-filled cavities usually show very high resistivity values, usually more than 10,000 ohm-m, but again these are variable depending on the conductivity of the surrounding strata and depth/size/shape of a void.
- Zones of electrical resistivity contrast are where relatively the top of rock is surrounded by moist, loose materials (such as clay) or where air-filled voids are embedded in relatively the top of limestone. These zones can be successfully detected by electrical resistivity tools.

4. RESEARCH EXPERIMENTS

4.1. STUDY SITE

The study site is located immediately within the southwestern limits of southwest Missouri of the Ozarks physiographic region which is characterized by undulating to rolling plains. Elevations of the region range between ~900 to ~1,500 ft. (asl). Southwest Missouri lies on the western side of the Ozark Uplift where the rock layers dip gently towards the west with minor faulting and folding, regionally. It is underlain by thick Mississippian-age limestone with high porosity and susceptible to dissolution. Uneven dissolution of this formation has resulted in a highly irregular bedrock-overburden interface. Therefore, karst density in the area is among Missouri's highest (Figures 4.1 and 4.2). The details of the studies are described in the next two sections.

This research emphasizes the need to apply efficient means for investigating hazards to urban development such as an unstable soil foundation for structures, flood hazards, groundwater contamination, and public safety in regards to potential catastrophic collapse.

Figure 4.1. Southwest Missouri map where the study was conducted. (http://www.nationsonline.org/oneworld/map/USA/missouri_map.htm).

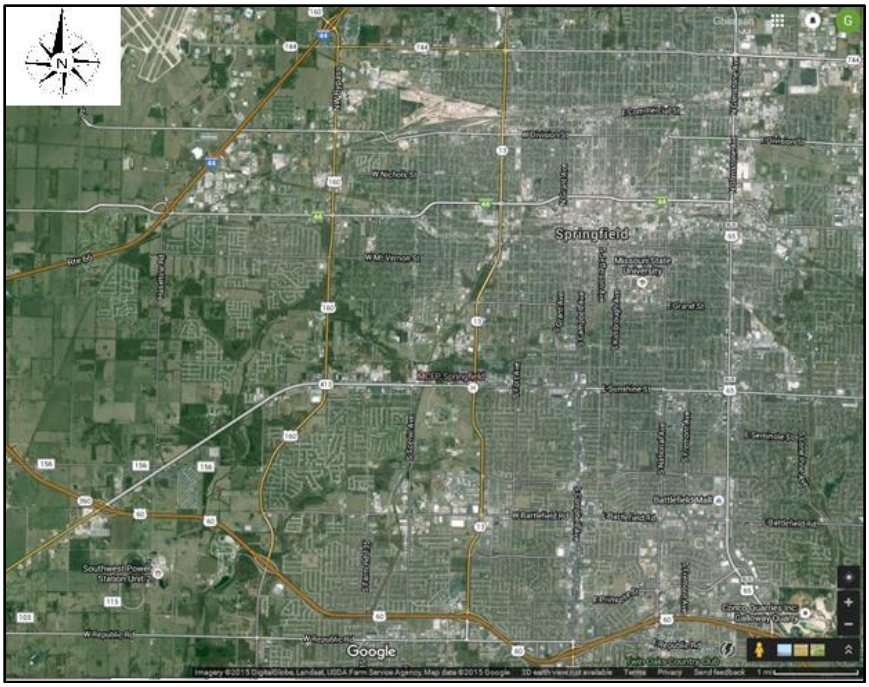

Figure 4.2. Map showing the location of the study area Zone A and Zone B (Courtesy of Google Earth).

4.2. MULTICHANNEL ANALYSIS OF SURFACE WAVES (MASW)

4.2.1. Data Acquisition. MASW data were acquired at 34 locations parallel and perpendicular to the ERT traverses oriented west to east. Total number of 272 MASW profiles in both west to east and north to south directions were acquired.

Data acquisition starts by the recording software launch and arming of the trigger geophone. Once the MASW array initialized, operator gives the command to release the seismic source (20 lb. sledgehammer) which notifies the seismograph to start data recording. From three to five seismic records were collected at each traverse for a purpose of staking to minimize the environment noise.

The main goal of the study was to develop appropriate acquisition parameters for MASW surveys conducted in karst terrain topography in order to improve the data resolution and maximize the depth of investigation. Figure 4.3 shows employed MASW equipment: Seistronix RAS-24 seismograph and 24 vertically polarized 4.5 Hz geophones. Source offsets of 10 ft. (3 m) and 30 ft. (9 m) were used for data acquisition. Receiver spacings of 2.5 ft. (0.76 m) and 5 ft. (1.5 m) were used in attempt to increase the vertical resolution of MASW data and to minimize lateral smearing. These parameters were chosen to achieve the investigation depth of approximately 30 ft. (9m).

For each MASW traverse, eight measurements per site were obtained (four records with seismic arrays oriented in west-east direction and four records with seismic arrays oriented in north-south direction (parallel and perpendicular to the direction of corresponding ERT traverses). Table 4.1 and Figure 4.4 shows parameters used to collect MASW data in the study.

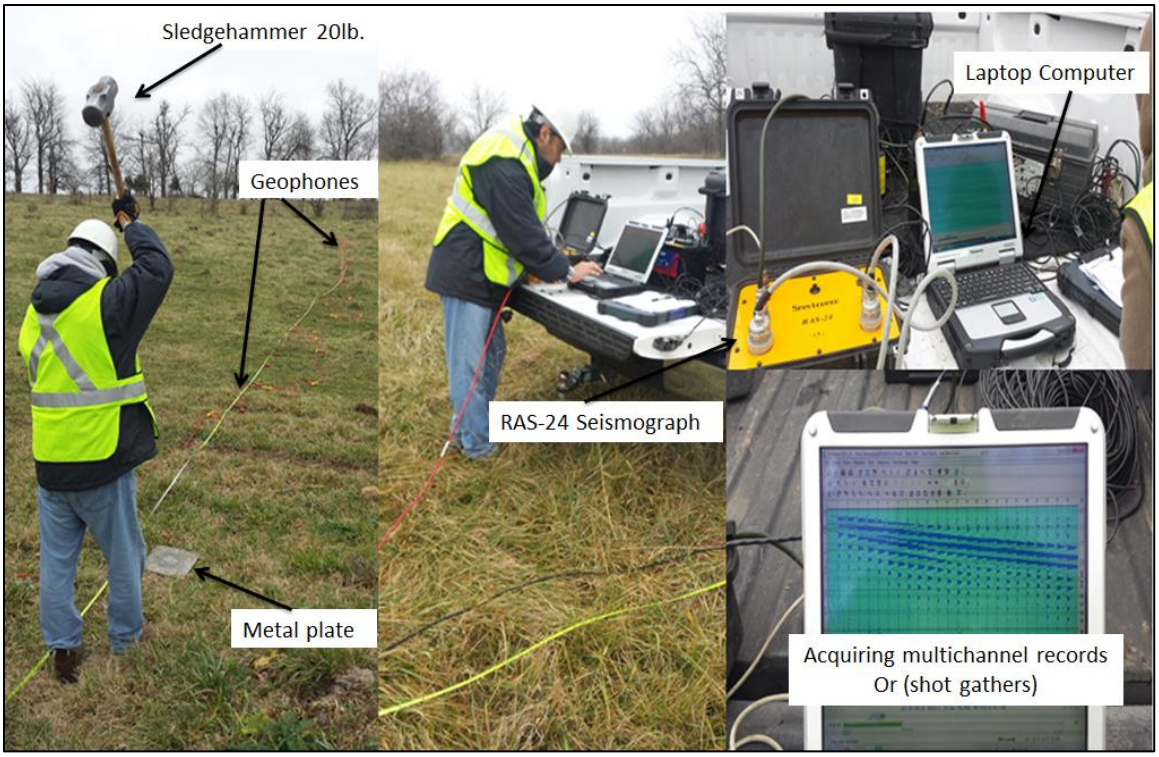

Figure 4.3. Active MASW data acquisition.

Table 4.1. Survey parameters used during MASW surveys in this study.

Source (lb.)	Receiver (Hz)	Receiver Spread (ft.)			Recording	
		Length (D)	Source offset (X1)	Receiver spacing (dx)	dt (ms)	T (sec)
				24-channel		
20lb. Sledge hammer	4.5	57.5	10	2.5	0.5ms	1sec
		115	30	5		
		57.5	10	2.5		
		115	30	5		

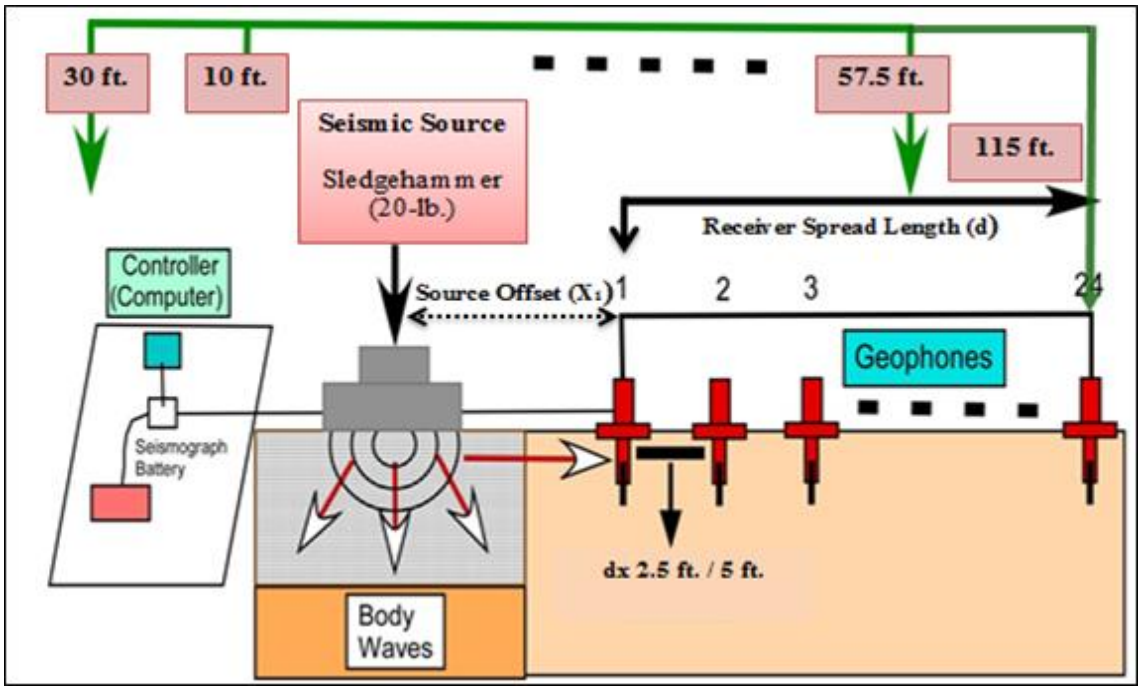

Figure 4.4. Schematic diagram of MASW data acquisition setup.

4.2.2. Data Processing and Interpretation. All seismic records acquired in this research were processed using SurfSeis4 software, developed by the Kansas Geological Survey.

Figures 4.5 to 4.7 display examples of the multichannel seismic records with overlay of preliminary data quality evaluation provided by the processing software. This step of data processing is to check overall data quality. This step is required to get a primary idea about the overall data quality, surface wave velocity range, dominant frequency, and the relative probability of higher modes contamination. “Excellent” and “good” quality data sets suggest that the surface waves are the most prominent seismic events (with highest signal-to-noise ratio) in the particular seismic record. “Fair” and “poor” quality data sets are typically contaminated by noise which can be a result of the irregularity of the bedrock surface, presence of voids, proximity of the array to the

construction site, receivers malfunction, etc. These seismic records can be not suitable for processing due to a lack of any recognizable surface wave signal.

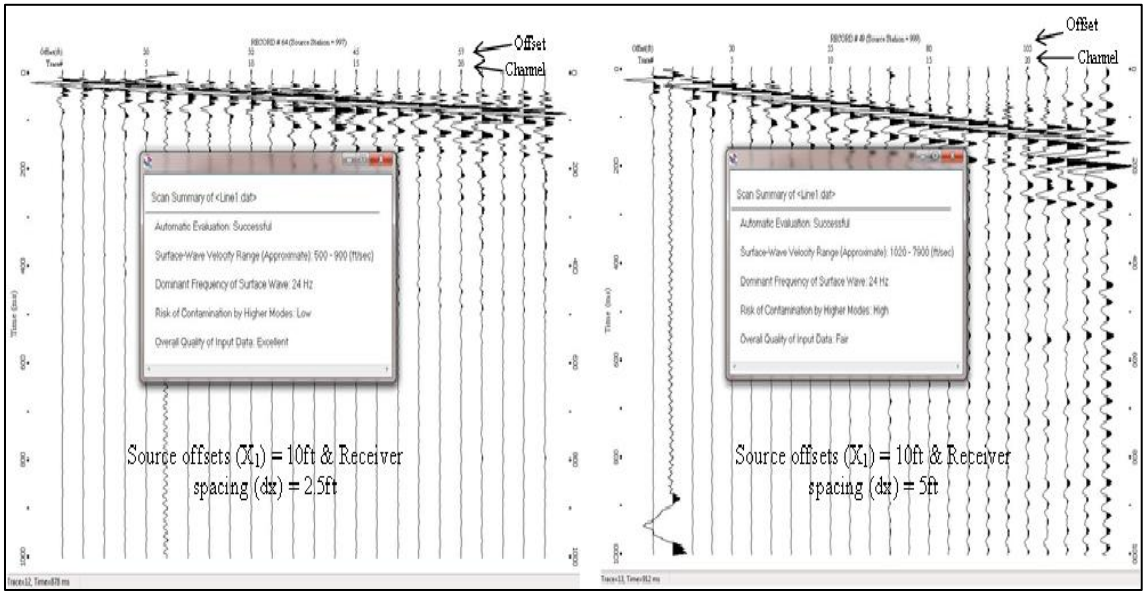

Figure 4.5. The multichannel seismic records with overlay of preliminary data quality evaluation provided by the processing software (SurfSeis4).

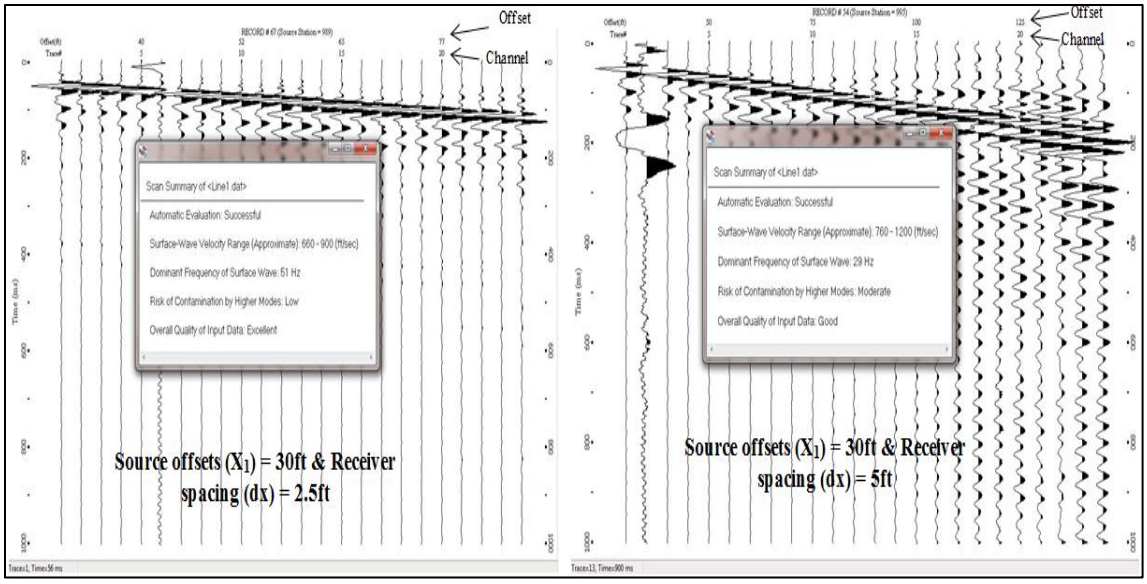

Figure 4.6. The multichannel seismic records with overlay of preliminary data quality evaluation provided by the processing software (SurfSeis4).

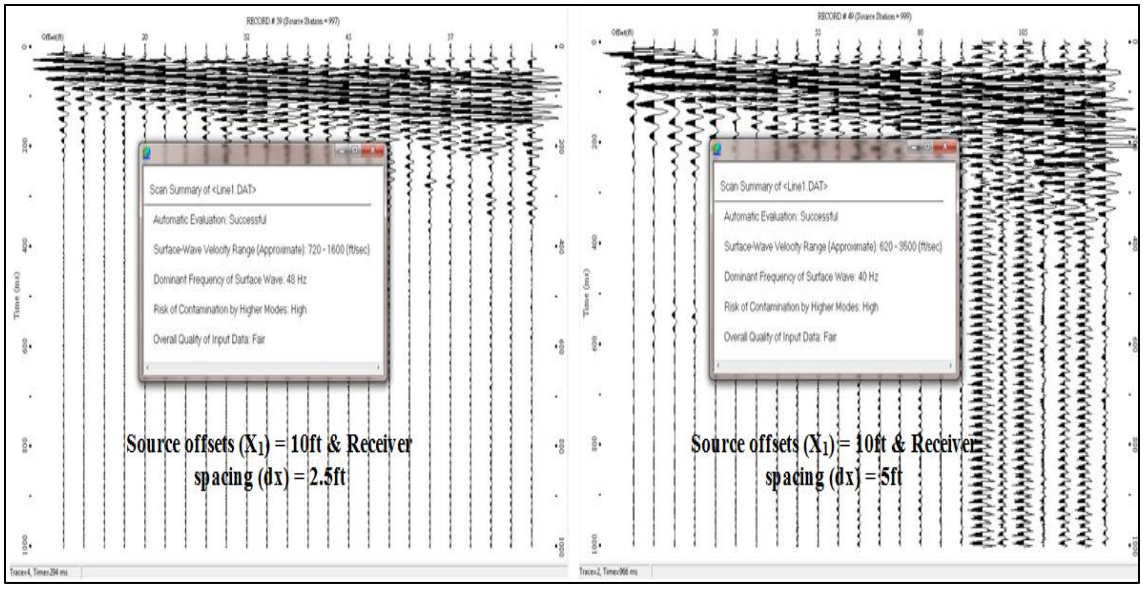

Figure 4.7 The multichannel seismic records with overlay of preliminary data quality evaluation provided by the processing software (SurfSeis4).

Following the visual evaluation, initial processing was initiated and included staking multiple shots as well as applying muting. The purpose of muting application is to remove specific seismic energy which arrives in specific time frame as a result of its velocity of propagation characteristics (Miller, Ivanov, et al., 2001). After proper muting, the quality and observation range of the desired mode (i.e., fundamental mode) improve significantly. The downside of muting is that it introduces a high velocity gradient feature at the low frequency end of the dispersion curve, which is not present before muting. This artifact can be easily handled by using the dispersion curve from the non-muted data that covers the same frequency range, so the artificially high velocity values can be ignored and are thus considered harmless (Miller, Ivanov, et al., 2001).

To show the effect of muting, the muting was applied to the seismic record collected with the source offset of 10ft. (3.04 m) and the receiver spacing of 2.5ft. (0.76) as it shown in Figures 4.8 and 4.9 to compare their dispersion curves before and after application of muting. It can be seen from Figure 4.8A that seismic energy associated

with surface waves dominates in the seismic record. Figure 4.8B displays the dispersion image with up-warping artifact appeared at high frequencies range that can be caused by contamination from higher modes. The fundamental mode dominates a wide frequency range between 38 and 61 Hz (with corresponding velocities between 1,060ft/sec and 1,735ft/sec) on the overtone image. However, the resulting 1-D shear wave velocity profile can be distorted if the extracted dispersion curve will be improperly picked from the ambiguous overtone image.

Figure 4.9B displays the dispersion image generated from the muted seismic record. The presence of higher mode surface waves in the original seismic record is almost completely eliminated, and the seismic energy associated with higher modes disappeared. The fundamental mode can be observed within a frequency range between 36 and 63 Hz (with corresponding velocities between 1,040ft/sec to 1,720ft/sec).

Their attempt to observe seismic energy associated with fundamental mode in the range between 36 and 67 Hz by boosting the amplitude of the phase-velocity – frequency spectrum did not bring any results. Thus, the seismic energy associated with higher modes is significantly higher, and corresponding dispersion images inhibit the ambiguous character of dispersion curve extraction of the fundamental mode trend below 40 Hz.

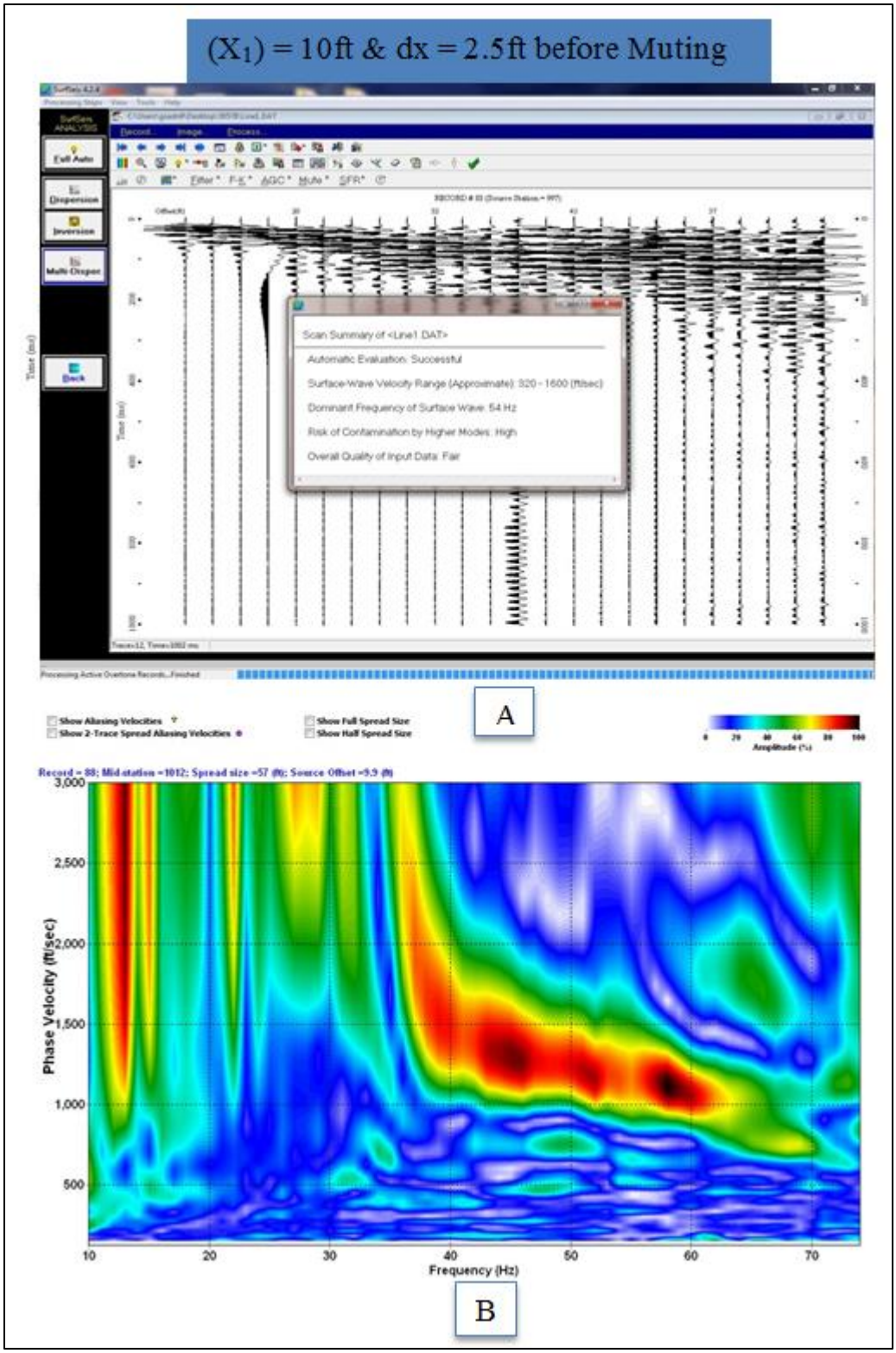

Figure 4.8. (A) The multichannel seismic record collected with the source offset of 10ft. (3.04 m) and receiver spacing of 2.5ft. (0.76m); (B) Corresponding overtone image with the fundamental and higher modes identified.

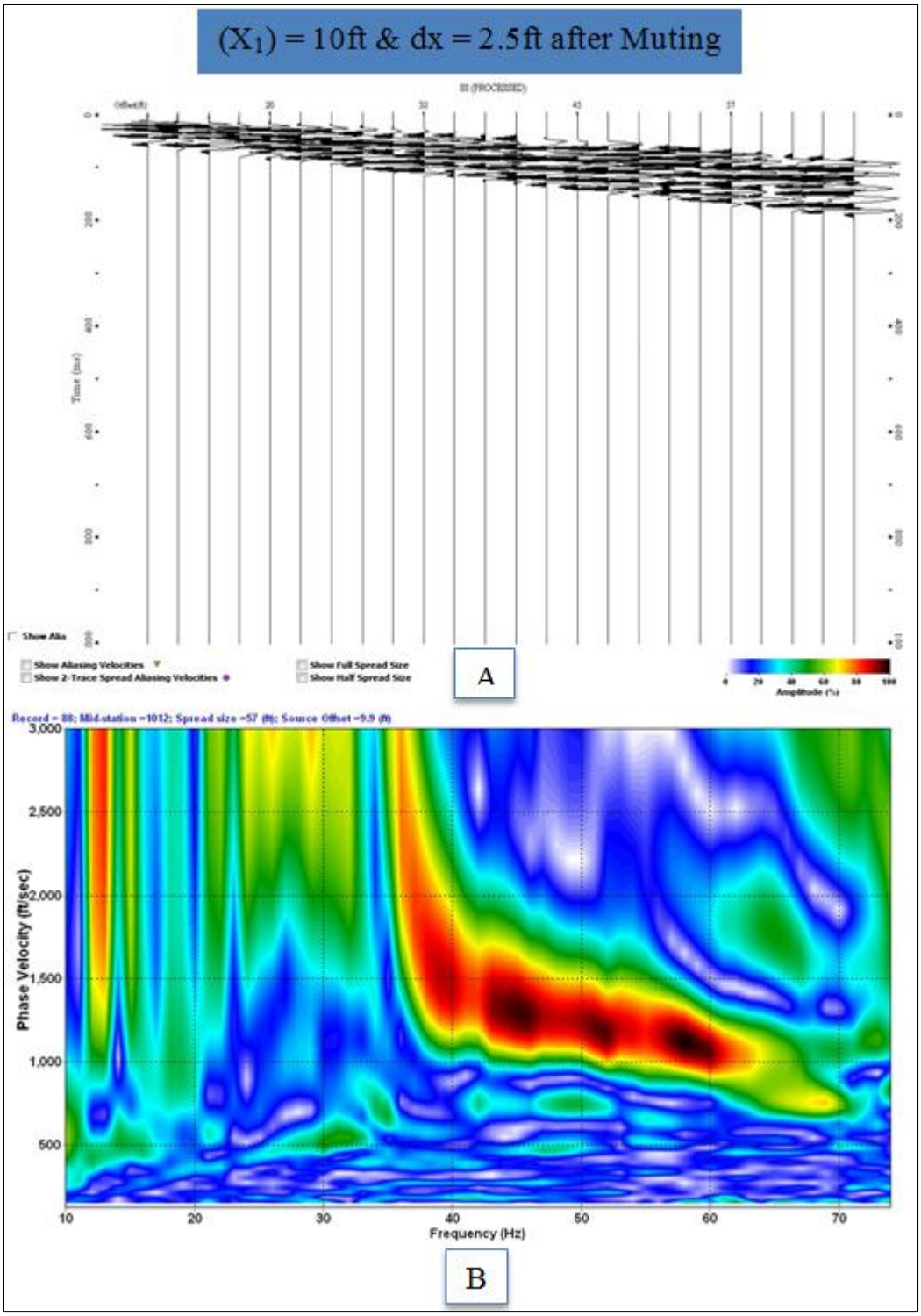

Figure 4.9. (A) The multichannel seismic record collected with offset of 10ft. (3.04 m) and receiver spacing of 2.5ft. (0.76 m) with applied muting. (B) Corresponding overtone image with the fundamental and higher modes identified.

Following the generation of overtone images, fundamental mode dispersion curves were estimated. The curves then were inverted to obtain 1-D shear wave velocity profiles (Figure 4.10).

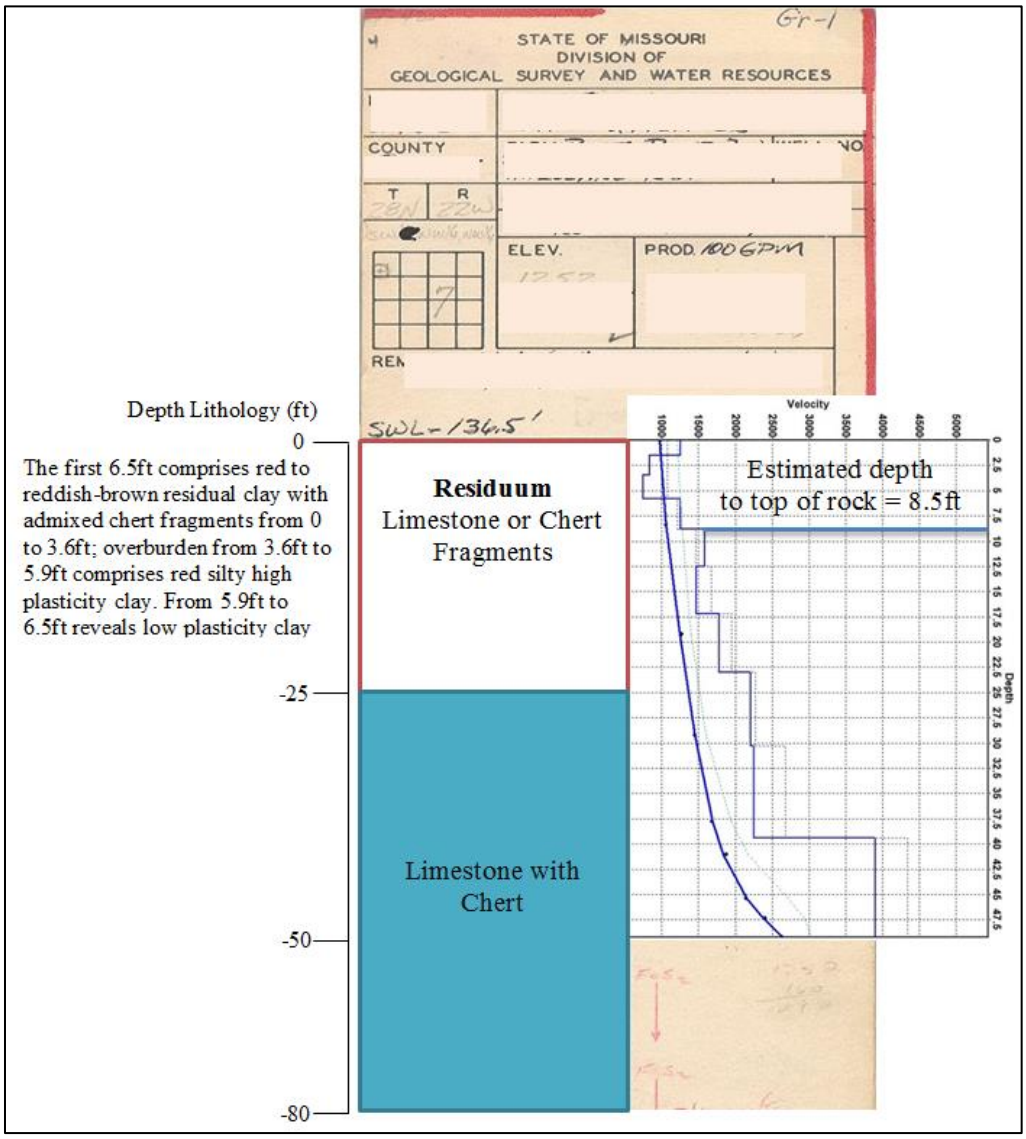

Figure 4.10. The results of the borehole BH1. In the same graph, the 1-D shear wave velocity profile deduced from the MASW survey along the Traverse No. 5 is shown. The MASW method estimated with accuracy the shear wave velocity in the layers and assisted in the layer identification of all the neighboring traverses.

Based on the author's previous experience, shear wave velocity in excess of 1,500 ft/sec corresponds to top of weathered rock. The value was used for this study for the purpose of mapping top of bedrock. To verify the interpretations, the MASW data were compared with bore holes in terms of depth to bedrock. As seen in Figure 4.10, the depth of interpreted top of bedrock on the MASW profile of collected by the 10 x 2.5ft. array configuration corresponded well to the top of rock obtained by drilling.

4.3. ELECTRICAL RESISTIVITY TOMOGRAPHY (ERT)

4.3.1. Data Acquisition. ERT data were acquired along a total of sixteen traverses oriented in W-E direction. The traverse orientations were selected to image the dominant north-south trending joint sets in the study area. The ERT traverses were spaced at 400ft. intervals.

The ERT data were acquired using an AGI SuperSting R8/IP, a multichannel electrode system powered by two 12-Volts batteries (Figure 4.11). During the field set-up, electrode cables were attached to metal stakes pounded to the ground using rubber-band. Switch box was also used to connect the electrodes (passive electrodes) to the resistivity meter. In an effort to ensure good quality ERT data are acquired, the field crews routinely performed contact resistance tests. The contact resistance test was performed prior data acquisition to ensure that all of the metal stakes are connected properly to the cables and to the ground.

One hundred sixty eight electrodes were spaced at 5ft. intervals covering a length of 835ft. and with expectation to image up to the depth of 100ft. As the length of the ERT traverses exceeded the array length of 835ft., 50% roll-along overlap option was used. A

dipole-dipole electrode configuration was utilized in this study. This array gives a better lateral resolution than the other types of arrays (Schlumberger and Wenner arrays) and is more suitable for investigating karst terrain.

Figure 4.11. ERT field set up.

4.3.2. Data Processing and Interpretation. ERT data were processed using Res2DInv software. As a first step of data processing, "bad" data points were removed manually. The bad data points were either anomalously high or low values. Then, "forward modeling" subroutine was used to specify the subsurface resistivity in order to calculate the apparent resistivity that would be measured by a survey over such a structure. As a result of data processing, 2D cross-sectional images were generated, as shown in Figures 4.12 and 4.13.

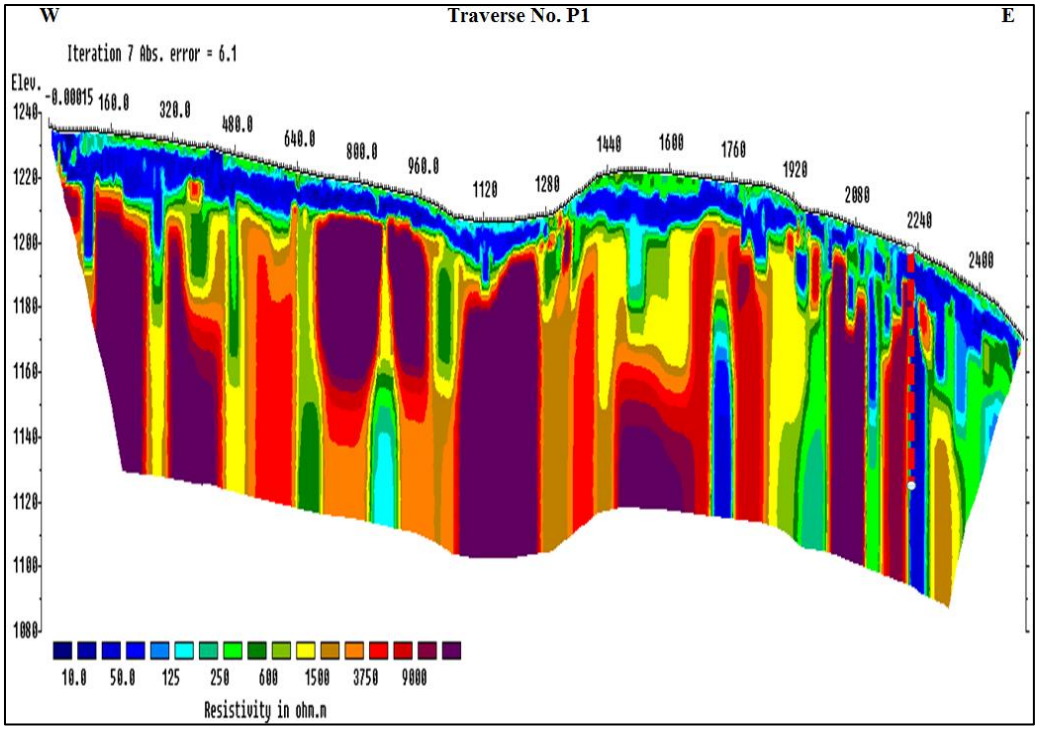

Figure 4.12. Typical example of 2-D uninterpreted ERT model. Traverse No. P1 and three overlapping ERT traverses acquired at the study site along 2,440ft.

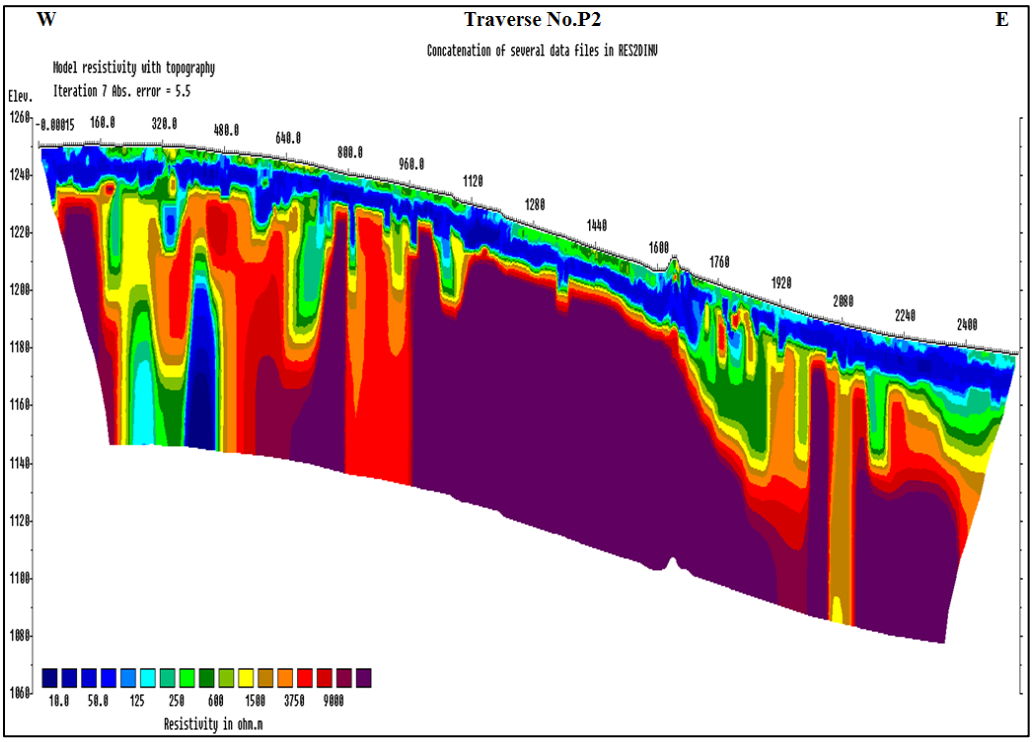

Figure 4.13. Typical example of 2-D uninterpreted ERT model. Traverse No. P2 and three overlapping ERT traverses acquired at the study site along 2,440ft.

Regarding the interpretation of the ERT data, , it was determined that moist soils are characterized by resistivity values of less than 125 ohm-m; dry soils by resistivity values greater than 125 ohm-m; moist weathered and/or fractured rock by resistivity values less than 600 ohm-m; moist fractured rock with moist piped clay/soil-fill by resistivity values less than 125 ohm-m; and drier, possibly less weathered rock by resistivity values greater than 600 ohm-m (Anderson et al., 2006; Muchaidze, 2009; Myat et al., 2008; Robison & Anderson, 2008). Figures 4.14 and 4.15 show the interpreted top on two representatives ERT traverses (Traverse No. P1 and Traverse No. P2).

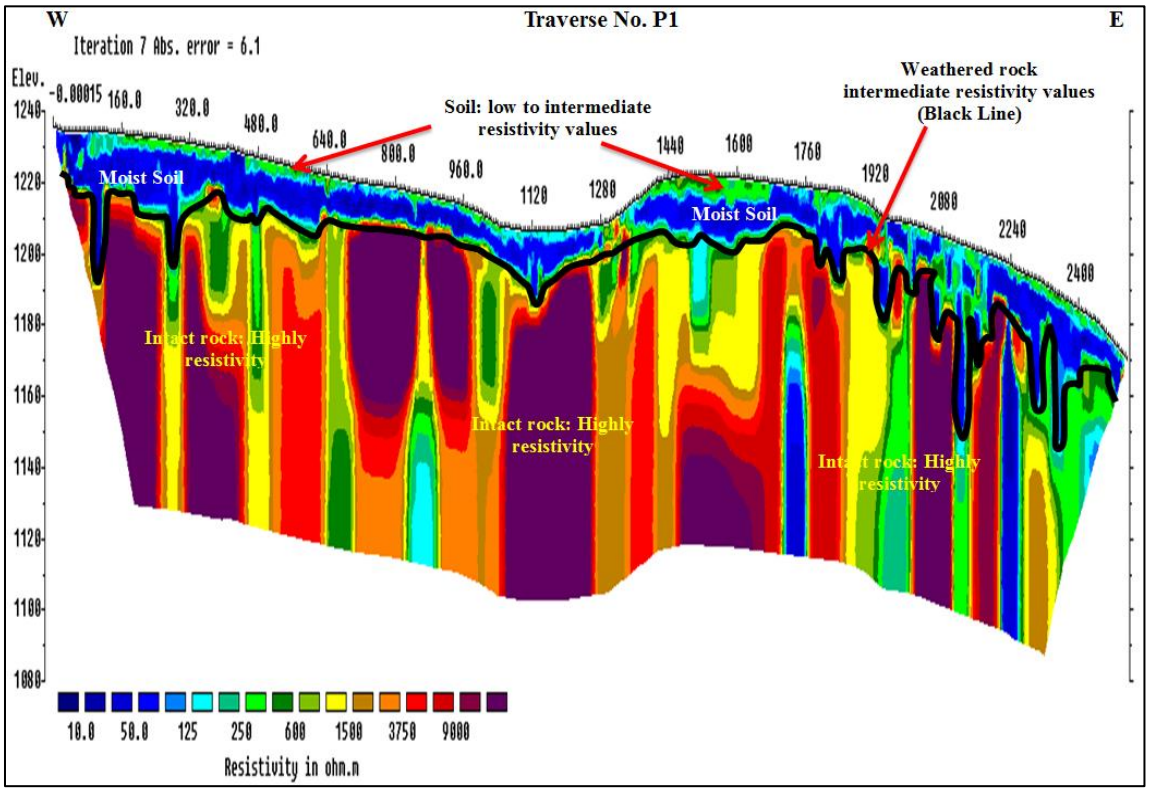

Figure 4.14. 2-D Interpreted versions of resistivity Traverse No. P1. Depth to top of bedrock is around 16 ft. and corresponds to the 125 ohm-m contour interval.

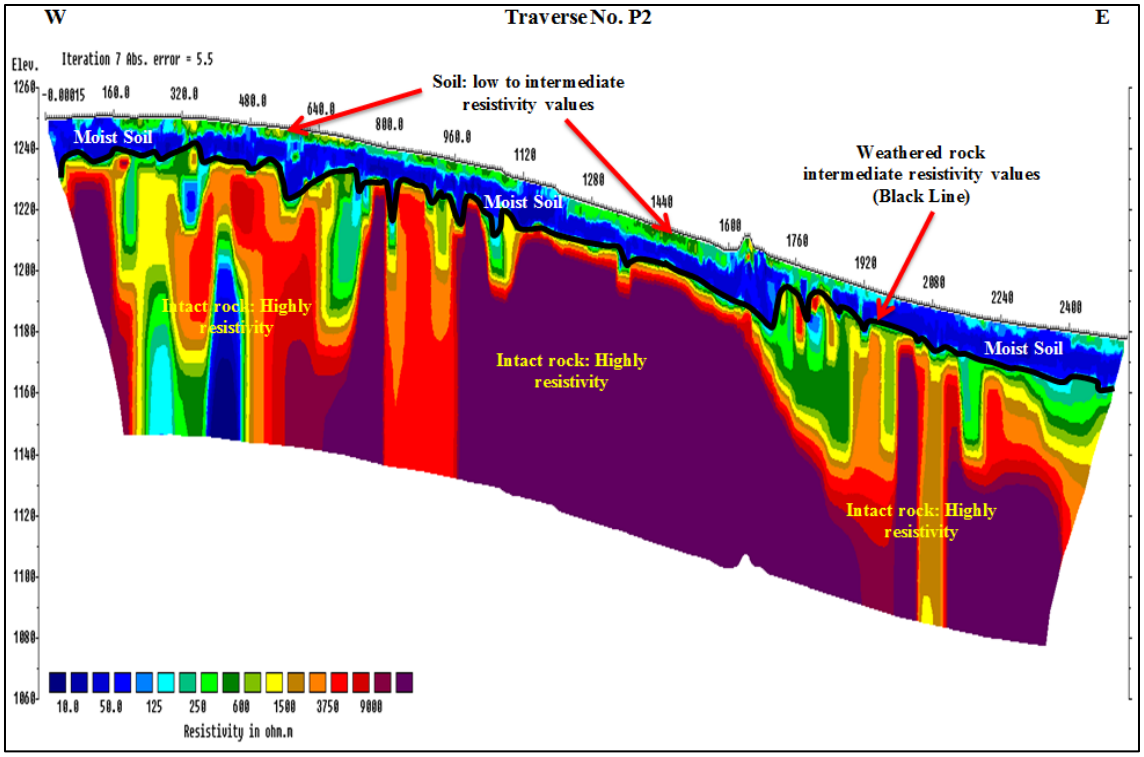

Figure 4.15. 2-D interpreted versions of resistivity Traverse No. P2. Depth to top of bedrock varies from 10 to 19 ft. and corresponds to the 125 ohm-m contour interval.

Boring control was used to verify the interpretations. Bore hole (BH1) was drilled along ERT Traverse No. P1. The borehole was drilled to a depth of 98ft. (30.6m) below subsurface. The top of rock was encountered at a depth of about 15ft. (4.6m), which was consistent with the ERT interpretations (Figure 4.16).

The ERT data interpretations were also compared with MASW data interpretations in terms of estimated depth to the top of bedrock (Figures. 4.17, 4.18, and 4.19). The comparison revealed a good agreement between the two.

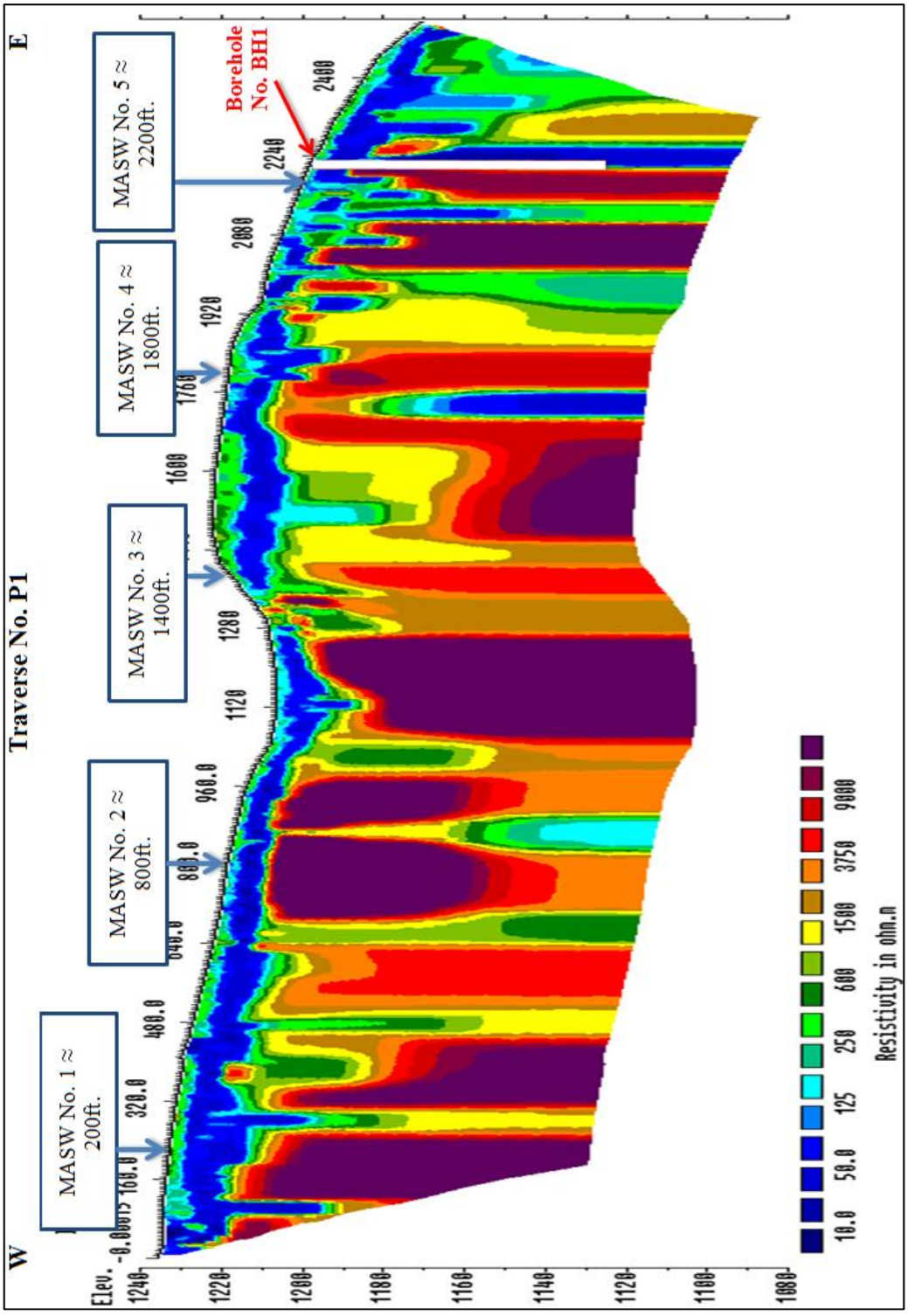

Figure 4.16. Interpreted versions of resistivity Traverse No. P1. The top of rock correlates reasonably well with the 125 ohm-m contour interval. The borehole location has been superposed in a red dashed line. The 200ft. mark on the resistivity profile corresponds with MASW profile No.1; the 800ft. mark corresponds with profile No. 2 location; the1, 400ft. mark corresponds with profile No.3; the1, 800ft. mark corresponds with profile No. 4; and the 2,200ft. mark corresponds with profile No.5.

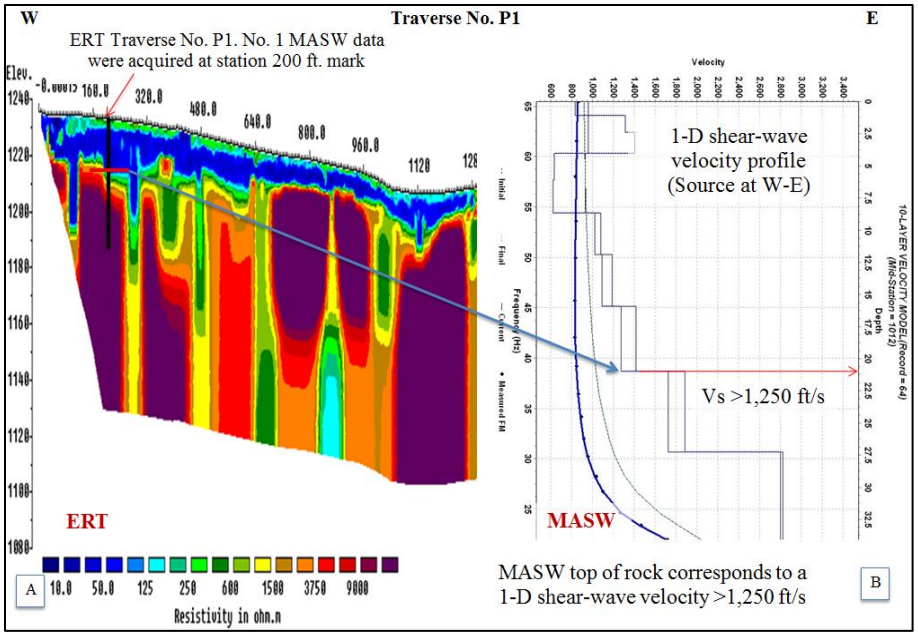

Figure 4.17. (A) ERT Traverse No. P1 tied with MASW profile No. 1. at the 200ft. (61m) mark; (B) Corresponding 1-D shear-wave velocity profile. MASW depth to top of weathered rock ("acoustic" top of rock) is identified at 15ft. (4.6m) depth. Red color line on Figure 8.8 (B) indicates interpreted depth to top of rock.

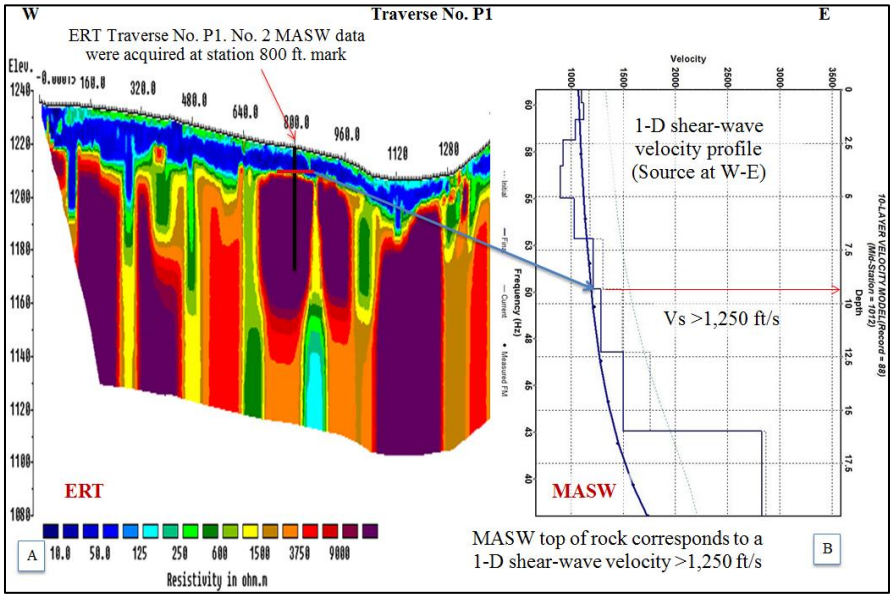

Figure 4.18. (A) ERT Traverse No. P1 tied with MASW profile No. 2.at the 800ft. (244m) mark; (B) Corresponding1-D shear-wave velocity profile. MASW depth to top of weathered rock ("acoustic" top of rock) is identified on 7ft. (2.1m) depth. Red color line on Figure 8.9 (B) indicates interpreted depth to top of rock.

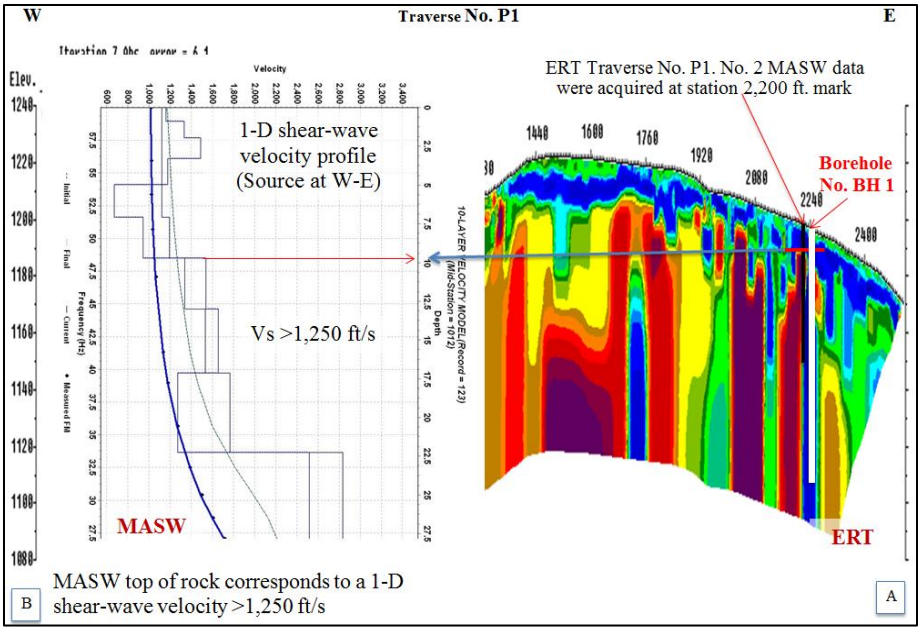

Figure 4.19. (A) ERT Traverse No. P1 tied with MASW profile No. 5 and borehole (BH1), at the 2,200ft. (670m) mark; (B) Corresponding 1-D shear-wave velocity profile. MASW depth to top of weathered rock ("acoustic" top of rock) is identified at 8.5ft. (2.6m) depth. Red color line on Figure 8.10 (B) indicates interpreted depth to top of rock.

5. COMPARATIVE ANALYSES

A comparative analysis is followed to analyze the performance of each MASW configuration. Two types of comparative analyses are performed in this research: qualitative and quantitative. The qualitative comparisons are solely based on visual assessments of overtone images. The quantitative comparisons are based on the assessment of the quantities calculated for each MASW configuration.

5.1. QUALITATIVE COMPARISON

The goal of qualitative analysis approach is twofold: 1) to compare overtone images and dispersion curves; 2) to compare 1-D shear wave velocity profiles. The comparisons are performed using different array configurations.

5.1.1. Comparison of Overtone Images and Dispersion Curves. Two MASW profiles (Traverse No.1 and Traverse No. 2) collected by different array configurations (geophone spacing, source offset, and the array orientation) were analyzed in attempt to evaluate the effect of different parameters on the process of dispersion curve extraction followed by modelling of 1-D shear wave velocity profiles. More specifically, the MASW data results were analyzed for frequency and phase velocity ranges, interpreted depth to top of rock, maximum depth of the investigation, signal-to-noise ratio, difference between the theoretical and the experimental dispersion curves (root-mean-square error), and the maximum number of iterations for inversion procedure.

5.1.2. MASW Traverse No. 1 Oriented West-East. Results from dispersion curves and shear wave velocity profiles for all the tested parameters are presented in Table 5.1.

Table 5.1. Results from all the dispersion curves and generated 1-D shear wave velocity profiles for MASW Traverse No. 1. X_1 - source offset; dx - geophone spacing; D - receiver spread length; λ_{max} maximum resolvable Rayleigh wave wavelength; λ_{min} minimum resolvable Rayleigh wave wavelength; Z_{max} penetration depth; S/N - signal-to-noise ratio; RMS -root-mean-square error.

(X_1) (ft.)	dx (ft.)	D (ft.)	Orientation	λmax (ft.)	λmin (ft.)	Velocity, Vphmax/Vphmin (ft./s)	Frequency, *f*min/*f*max (Hz)	Zmax (ft.)	Risk of Higher mode Value	(S/N) (%)	(RMS) Error (%)	Iteration Value (1-30)
10	2.5	57.5	W-E	50	14	1,541-895	31-65	18	Moderate	98	6.5	9
10	5	115	W-E	56	17	1,696-917	30-53	19	High	88	5.6	8
30	2.5	57.5	W-E	50	16	1,553-859	31-54	20	Low	85	6.8	6
30	5	115	W-E	46	19	1,744-995	38-53	16	High	92	6.3	6
10	2.5	57.5	N-S	64	18	1,740-850	27-47	23	Moderate	98	4.8	9
10	5	115	N-S	54	19	1,515-900	28-47	17	High	70	2.4	8
30	2.5	57.5	N-S	52	15	1,609-805	31-55	18	High	88	10.8	6
30	5	115	N-S	56	19	1,688-874	30-47	18	High	76	9.8	10

Figure 5.1A displays the MASW data collected along Traverse No.1 oriented west-east with source offset of 10ft. and geophone spacing of 2.5ft. Phase velocities were manually picked using 11 equally spaced points from the fundamental-mode dispersion curve in Figure 5.1B (represented by white dots) and used for an inversion process to generate a 1-D shear wave velocity model (Figure 5.1C).

The dispersion analysis shows that the data possesses dominant frequencies at approximately f_{min}= 31 Hz to f_{max} = 65 Hz. The phase velocity varied between V_{phmax} = 1,541ft/sec and V_{phmin} = 895ft/sec, corresponding to the Rayleigh waves wavelength of λ_{min} = 14ft. and λ_{max} = 55ft. The picked frequency and phase velocity ranges fall within the determined fundamental mode. With these values and the traverse length, the minimum and maximum penetration depths is Z_{max} = 18ft.

These parameters yielded the inverted Vs model that was obtained with the high signal-to-noise ratio (S/N) of 98 % and an RMS error of 6.5 % with nine iterations. The

fundamental mode is clearly observable in the absence of a higher mode signs. The dispersion curve is continuous and distinguishable at frequencies higher than 30 Hz. The theoretical dispersion curve matches the experimental curve at higher frequencies. These results can be due to the employed combination of the receiver spread length and the source offset.

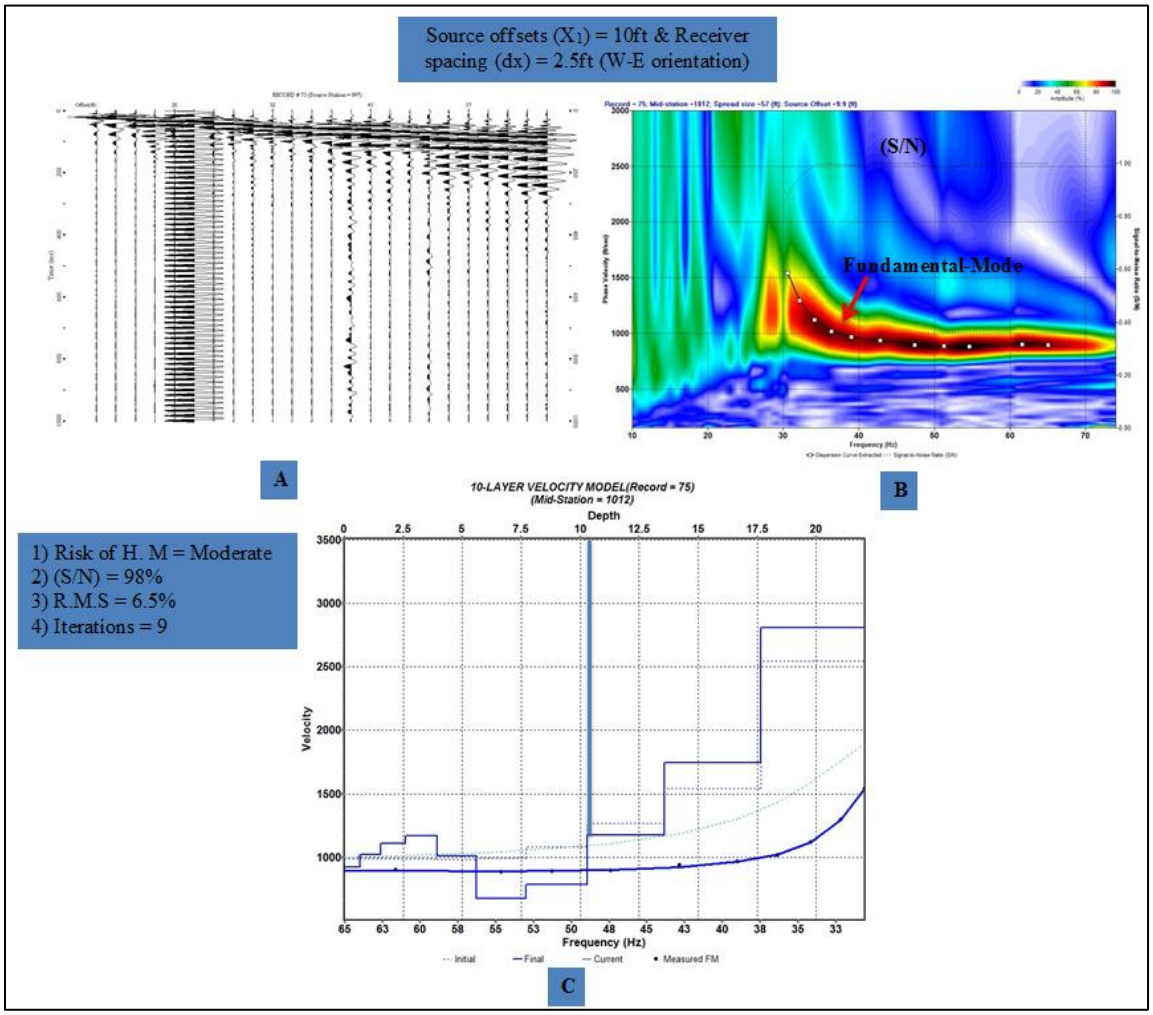

Figure 5.1. MASW survey data collected along Traverse No.1 oriented west-east array. (A) The 24 channel record (shot gather); (B) The dispersion image (overtone) with superposed dispersion curve (phase velocity versus frequency) where the fundamental mode is quite clear. (C) The 1-D shear wave velocity profile, deduced from the inversion technique. 1) Risk of higher mode; 2) The signal-to-noise ratio (S/N); 3) R.M.S. error; 4) Iterations.

Figure 5.2A displays the MASW data collected along Traverse No.1 oriented west-east with source offset of 10ft. and geophone spacing of 5ft. Phase velocities were manually picked using 9 equally spaced points from the fundamental-mode dispersion curve in Figure 5.2B (represented by white dots) and used for an inversion process to generate a 1-D shear wave velocity model (Figure 5.2C).

The dispersion analysis shows that the data possesses dominant frequencies at approximately f_{min}= 30 Hz to f_{max} = 53 Hz. The phase velocity varied between V_{phmax} = 1,696 ft/sec and V_{phmin} = 917ft/sec, corresponding to the Rayleigh waves wavelength of λ_{min} = 17ft. and λ_{max} = 56ft. The picked frequency and phase velocity ranges fall within the determined fundamental mode. With these values and the traverse length, the minimum and maximum penetration depths is Z_{max} = 19ft.

These parameters yielded the inverted Vs model that was obtained with the high signal-to-noise ratio (S/N) of 88 % and an RMS error of 9.2 % with eight iterations. The fundamental mode lacks separation from the higher mode (this overlap might be due to the similarities in phase velocities in that frequency ranges). The dispersion curve is non-coherent at frequencies higher than 30 Hz. The theoretical dispersion curve fairly matches the experimental curve at higher frequencies. Low quality survey results can be due to the employed combination of the receiver spread length and the source offset.

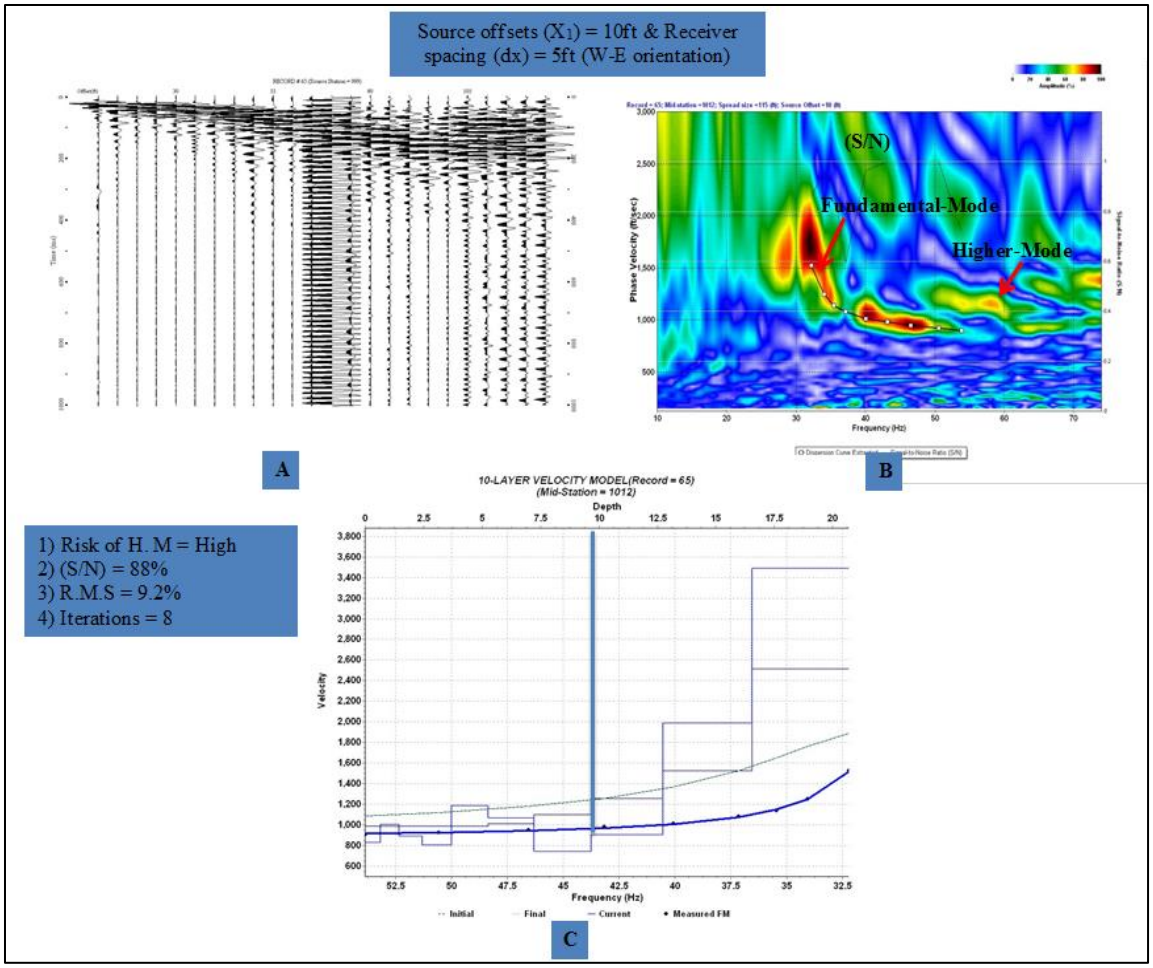

Figure 5.2. MASW survey data collected along Traverse No. 1 oriented west-east array. (A) The 24 channel record (shot gather); (B) The dispersion image (overtone) with superposed dispersion curve (phase velocity versus frequency) where the fundamental mode is quite clear. (C) The 1-D shear wave velocity profile, deduced from the inversion technique. 1) Risk of higher mode; 2) The signal-to-noise ratio (S/N); 3) R.M.S. error; 4) Iterations.

Figures 5.3 and 5.4 display the MASW data collected along Traverse No. 1 oriented west-east on the basis of the comparison between the MASW survey output for the employed source offset of 30 ft. (9.14m) with a receiver spacing of 2.5ft. (0.76m) and the source offset of 30ft. (9.14m) with a receiver spacing of 5ft. (1.52m), respectively. Figures 5.3 and 5.4 show how the various combinations of source offset and geophone

spacing can affect the resulting overtone images and extracted dispersion curves for the fundamental and higher modes.

Figure 5.3A displays the MASW data collected along Traverse No.1 oriented west-east with source offset of 30ft. and geophone spacing of 2.5ft. Phase velocities were manually picked using 8 equally spaced points from the fundamental-mode dispersion curve in Figure 5.3B (represented by white dots) and used for an inversion process to generate a 1-D shear wave velocity model (Figure 5.3C).

The dispersion analysis shows that the data possesses dominant frequencies at approximately f_{min}= 31 Hz to f_{max} = 54 Hz. The phase velocity varied between V_{phmax} = 1,533 ft/sec and V_{phmin} = 859 ft/sec, corresponding to the Rayleigh waves wavelength of λ_{min} = 16ft. and λ_{max} = 50ft. The picked frequency and phase velocity ranges fall within the determined fundamental mode. With these values and the traverse length, the minimum and maximum penetration depths is Z_{max} = 20ft.

These parameters yielded the inverted Vs model that was obtained with the high signal-to-noise ratio (S/N) of 85 % and an RMS error of 13.2 % with six iterations. The fundamental mode is hardly distinguishable and very limited in the presence of a higher mode. The dispersion curve is continuous and distinguishable at frequencies higher than 30 Hz. The theoretical dispersion curve fairly matches the experimental curve at higher frequencies. These results can be due to the employed combination of the receiver spread length and the source offset.

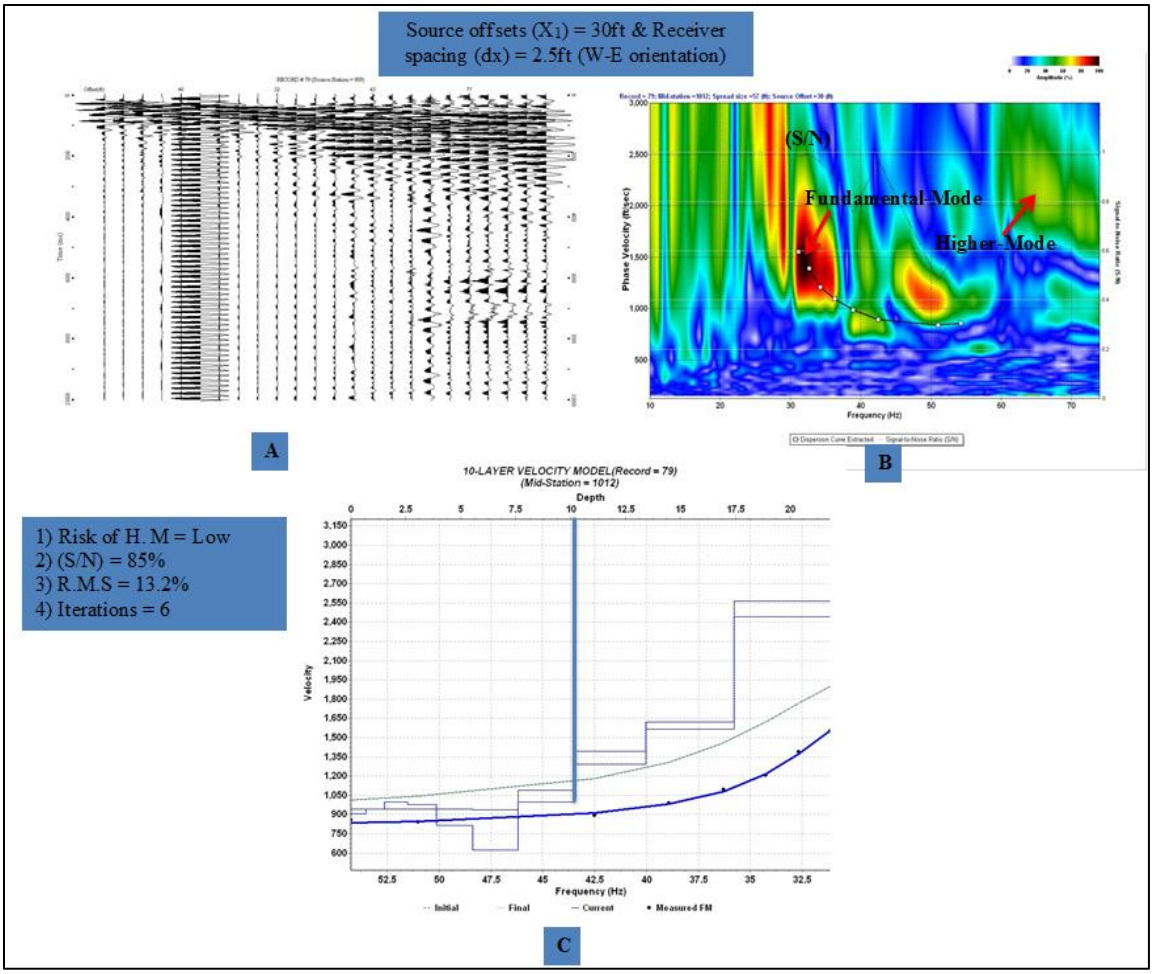

Figure 5.3. MASW survey data collected along Traverse No.1 oriented west-east array. (A) The 24 channel record (shot gather); (B) The dispersion image (overtone) with superposed dispersion curve (phase velocity versus frequency) where the fundamental mode is quite clear. (C) The 1-D shear wave velocity profile, deduced from the inversion technique. 1) Risk of higher mode; 2) The signal-to-noise ratio (S/N); 3) R.M.S. error; 4) Iterations.

Figure 5.4A displays the MASW data collected along Traverse No.1 oriented west-east with source offset of 30ft. and geophone spacing of 5ft. Phase velocities were manually picked using 8 equally spaced points from the fundamental-mode dispersion curve in Figure 5.4B (represented by white dots) and used for an inversion process to generate a 1-D shear wave velocity model (Figure 5.4C). The dispersion analysis shows that the data possesses dominant frequencies at approximately f_{min}= 38 Hz to f_{max} = 53

Hz. The phase velocity varied between V_{phmax} = 1,744ft/sec and V_{phmin} = 995ft/sec, corresponding to the Rayleigh waves wavelength of λ_{min} = 19ft. and λ_{max} = 46ft. The picked frequency and phase velocity ranges fall within the determined fundamental mode. With these values and the traverse length, the minimum and maximum penetration depths is Z_{max} = 19ft. These parameters yielded the inverted Vs model that was obtained with the high signal-to-noise ratio (S/N) of 92 % and an RMS error of 12.6 % with six iterations. The fundamental mode lacks separation from the higher mode (this overlap might be due to the similarities in phase velocities in that frequency ranges). The dispersion curve is non-coherent at frequencies higher than 30 Hz. The theoretical dispersion curve fairly matches the experimental curve at higher frequencies. Low quality survey results can be due to the employed combination of the receiver spread length and the source offset.

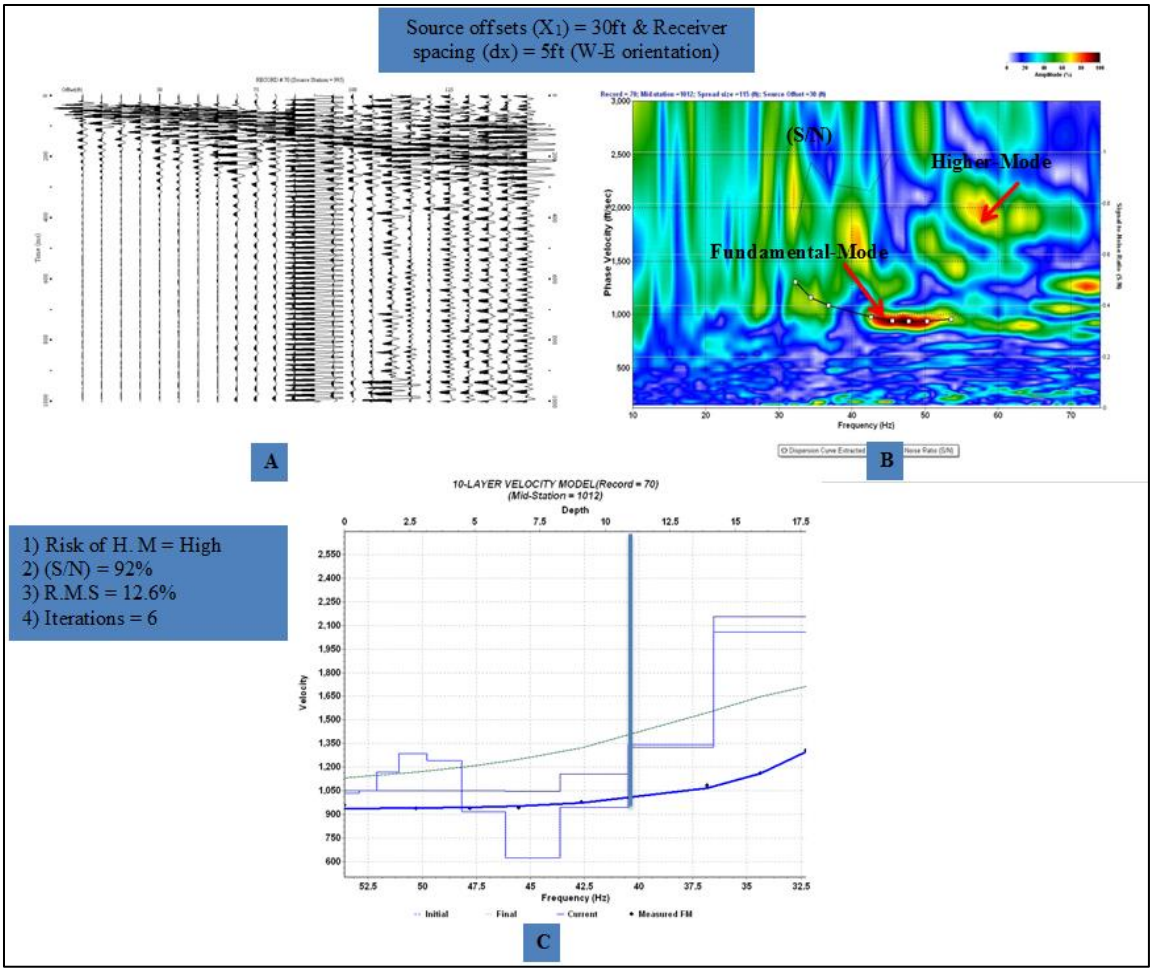

Figure 5.4. MASW survey data collected along Traverse No.1 oriented west-east array. (A) The 24 channel record (shot gather); (B) The dispersion image (overtone) with superposed dispersion curve (phase velocity versus frequency) where the fundamental mode is quite clear. (C) The 1-D shear wave velocity profile, deduced from the inversion technique. 1) Risk of higher mode; 2) The signal-to-noise ratio (S/N); 3) R.M.S. error; 4) Iterations.

5.1.2. MASW Traverse No. 1 Oriented North to South. Figure 5.5A displays the MASW data collected along Traverse No. 1 oriented west-east with source offset of 10ft. and geophone spacing of 2.5ft. Phase velocities were manually picked using 11 equally spaced points from the fundamental-mode dispersion curve in Figure 5.5B (represented by white dots) and used for an inversion process to generate a 1-D shear wave velocity model (Figure 5.5C).

The dispersion analysis shows that the data possesses dominant frequencies at approximately f_{min}= 27 Hz to f_{max} = 47 Hz. The phase velocity varied between V_{phmax} = 1,740ft/sec and V_{phmin} = 850ft/sec, corresponding to the Rayleigh waves wavelength of λ_{min} = 18ft. and λ_{max} = 64ft. The picked frequency and phase velocity ranges fall within the determined fundamental mode. With these values and the traverse length, the minimum and maximum penetration depths is Z_{max} = 21.5ft.

These parameters yielded the inverted Vs model that was obtained with the high signal-to-noise ratio (S/N) of 98 % and an RMS error of 4.8 % with nine iterations. The fundamental mode is clearly observable in the absence of a higher mode signs. The dispersion curve is continuous and distinguishable at frequencies higher than 30 Hz. The theoretical dispersion curve matches the experimental curve at higher frequencies. These results can be due to the employed combination of the receiver spread length and the source offset.

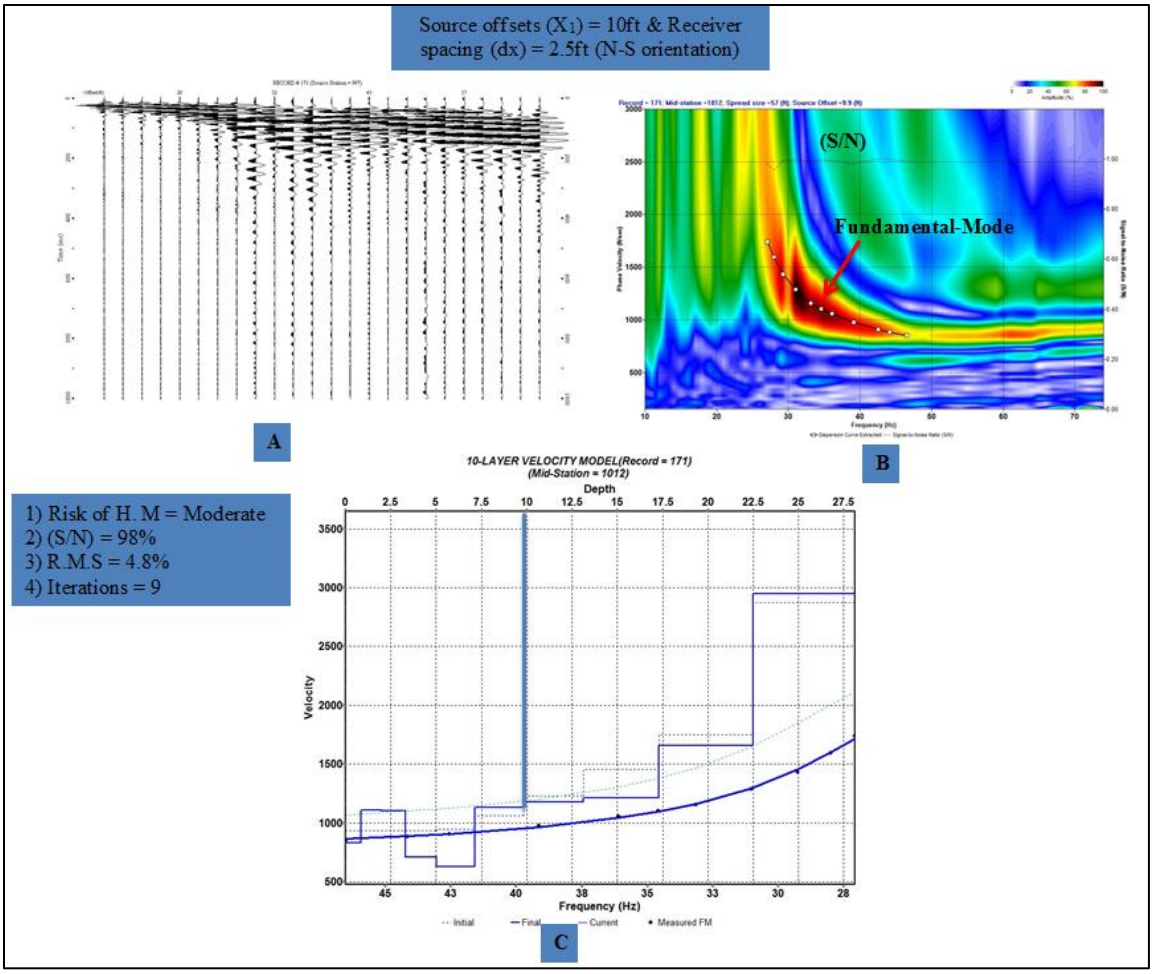

Figure 5.5. MASW survey data collected along Traverse No. 1 oriented north to south array. (A) The 24 channel record (shot gather); (B) The dispersion image (overtone) with superposed dispersion curve (phase velocity versus frequency) where the fundamental mode is quite clear. (C) The 1-D shear wave velocity profile, deduced from the inversion technique. 1) Risk of higher mode; 2) The signal-to-noise ratio (S/N); 3) R.M.S. error; 4) Iterations.

Figure 5.6A displays the MASW data collected along Traverse No. 1 oriented west-east with source offset of 10ft. and geophone spacing of 2.5ft. Phase velocities were manually picked using 9 equally spaced points from the fundamental-mode dispersion curve in Figure 5.6B (represented by white dots) and used for an inversion process to generate a 1-D shear wave velocity model (Figure 5.6C).

The dispersion analysis shows that the data possesses dominant frequencies at approximately f_{min}= 28 Hz to f_{max} = 47 Hz. The phase velocity varied between V_{phmax} = 1,515 ft/sec and V_{phmin} = 900ft/sec, corresponding to the Rayleigh waves wavelength of λ_{min} = 19ft. and λ_{max} = 54ft. The picked frequency and phase velocity ranges fall within the determined fundamental mode. With these values and the traverse length, the minimum and maximum penetration depths is Z_{max} = 17ft.

These parameters yielded the inverted Vs model that was obtained with the high signal-to-noise ratio (S/N) of 70 % and an RMS error of 4 % with twelve iterations, the lowest of the eight trials. The fundamental mode is observable and can be distinguished from the higher mode. The dispersion curve is continuous at frequencies higher than 30 Hz. The theoretical dispersion curve fairly matches the experimental curve at higher frequencies. These results can be due to the employed combination of the receiver spread length and the source offset.

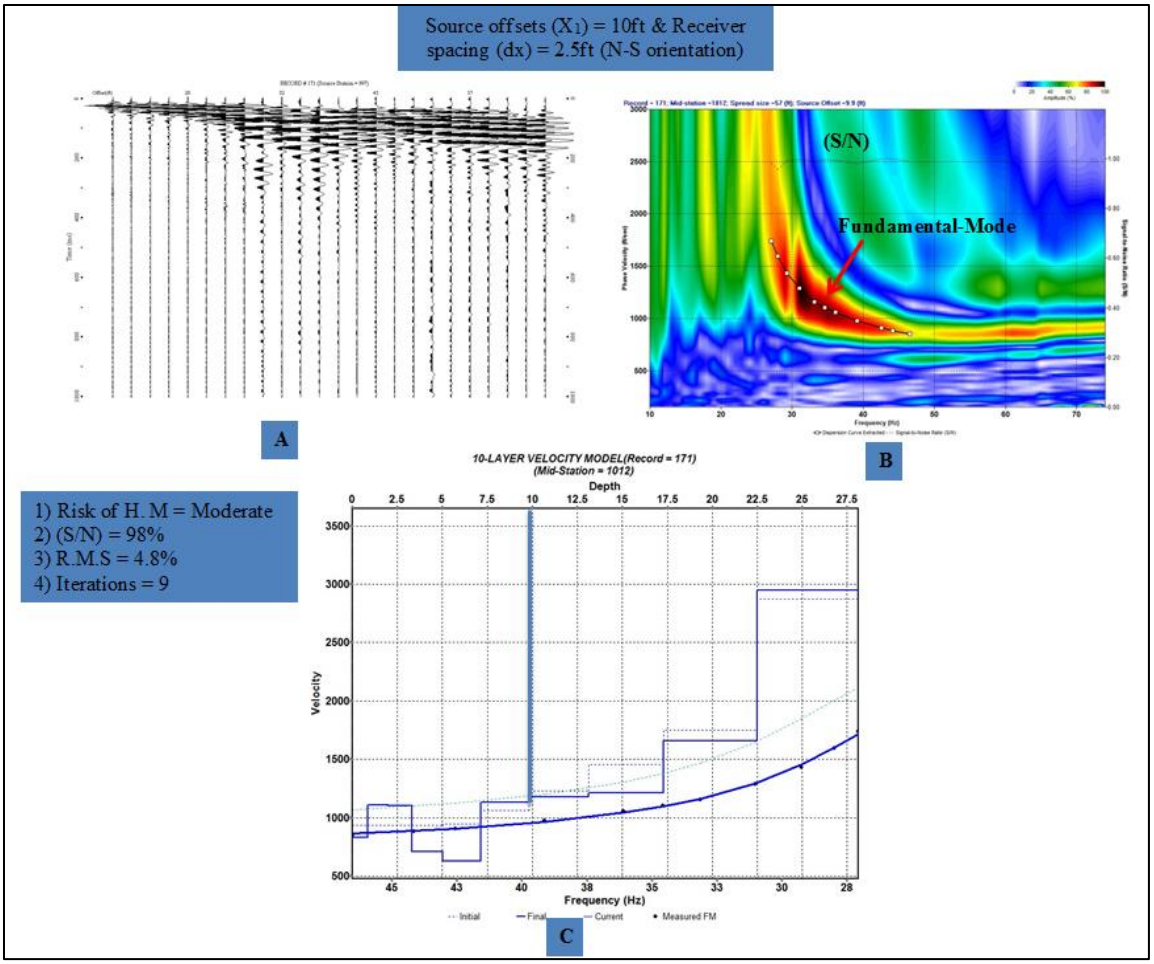

Figure 5.6. MASW survey data collected along Traverse No. 1 oriented north to south array. (A) The 24 channel record (shot gather); (B) The dispersion image (overtone) with superposed dispersion curve (phase velocity versus frequency) where the fundamental mode is quite clear. (C) The 1-D shear wave velocity profile, deduced from the inversion technique. 1) Risk of higher mode; 2) The signal-to-noise ratio (S/N); 3) R.M.S. error; 4) Iterations.

Figures 5.7 and 5.8 display the MASW data collected along Traverse No. 1 oriented north-south on the basis of the comparison between the MASW survey output for the employed source offset of 30ft. (9.14m) with a receiver spacing of 2.5ft. (0.76m) and the source offset of 30ft. (9.14m) with a receiver spacing of 5ft. (1.52m), respectively. Figures 5.7 and 5.8 show how the various combinations of source offset and

geophone spacing can affect the resulting overtone images and extracted dispersion curves for the fundamental and higher modes.

Figure 5.7A displays the MASW data collected along Traverse No. 1 oriented north-south with source offset of 30ft. and geophone spacing of 2.5ft. Phase velocities were manually picked using 9 equally spaced points from the fundamental-mode dispersion curve in Figure 5.7B (represented by white dots) and used for an inversion process to generate a 1-D shear wave velocity model (Figure 5.8C).

The dispersion analysis shows that the data possesses dominant frequencies at approximately f_{min}= 31 Hz to f_{max} = 55 Hz. The phase velocity varied between V_{phmax} = 1,609 ft/sec and V_{phmin} = 805ft/sec, corresponding to the Rayleigh waves wavelength of λ_{min} = 15ft. and λ_{max} = 52ft. The picked frequency and phase velocity ranges fall within the determined fundamental mode. With these values and the traverse length, the minimum and maximum penetration depths is Z_{max} = 18ft.

These parameters yielded the inverted Vs model that was obtained with the high signal-to-noise ratio (S/N) of 88 % and an RMS error of 19 % with six iterations. The fundamental mode is hardly distinguishable and limited in the presence of a higher mode. The dispersion curve is continuous and distinguishable at frequencies higher than 30 Hz. The theoretical dispersion curve fairly matches the experimental curve at higher frequencies. Low quality survey results can be due to the employed combination of the receiver spread length and the source offset.

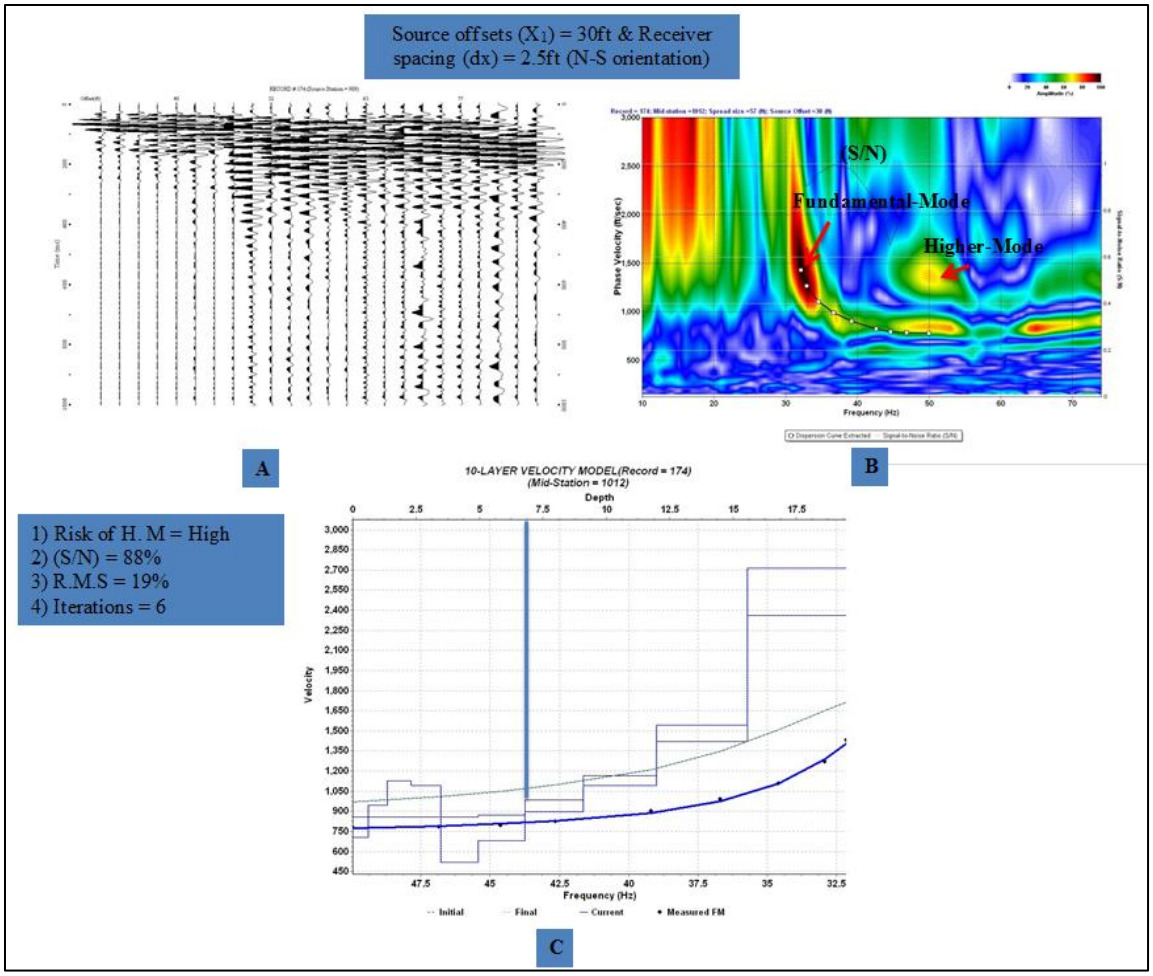

Figure 5.7 MASW survey data collected along Traverse No. 1 oriented north to south array. (A) The 24 channel record (shot gather); (B) The dispersion image (overtone) with superposed dispersion curve (phase velocity versus frequency) where the fundamental mode is quite clear. (C) The 1-D shear wave velocity profile, deduced from the inversion technique. 1) Risk of higher mode; 2) The signal-to-noise ratio (S/N); 3) R.M.S. error; 4) Iterations.

Figure 5.8A displays the MASW data collected along Traverse No. 1 oriented north-south with source offset of 30ft. and geophone spacing of 5ft. Phase velocities were manually picked using 7 equally spaced points from the fundamental-mode dispersion curve in Figure 5.8B (represented by white dots) and used for an inversion process to generate a 1-D shear wave velocity model (Figure 5.8C).

The dispersion analysis shows that the data possesses dominant frequencies at approximately f_{min}= 30 Hz to f_{max} = 47 Hz. The phase velocity varied between V_{phmax} = 1,688ft/sec and V_{phmin} = 874ft/sec, corresponding to the Rayleigh waves wavelength of λ_{min} = 19ft. and λ_{max} = 56ft. The picked frequency and phase velocity ranges fall within the determined fundamental mode. With these values and the traverse length, the minimum and maximum penetration depths is Z_{max} = 18ft.

These parameters yielded the inverted Vs model that was obtained with the high signal-to-noise ratio (S/N) of 76 % and an RMS error of 12 % with ten iterations. The fundamental mode is hardly distinguishable and limited in the presence of a higher mode. The dispersion curve is continuous and distinguishable at frequencies higher than 30 Hz. The theoretical dispersion curve fairly matches the experimental curve at higher frequencies. Low quality survey results can be due to the employed combination of the receiver spread length and the source offset.

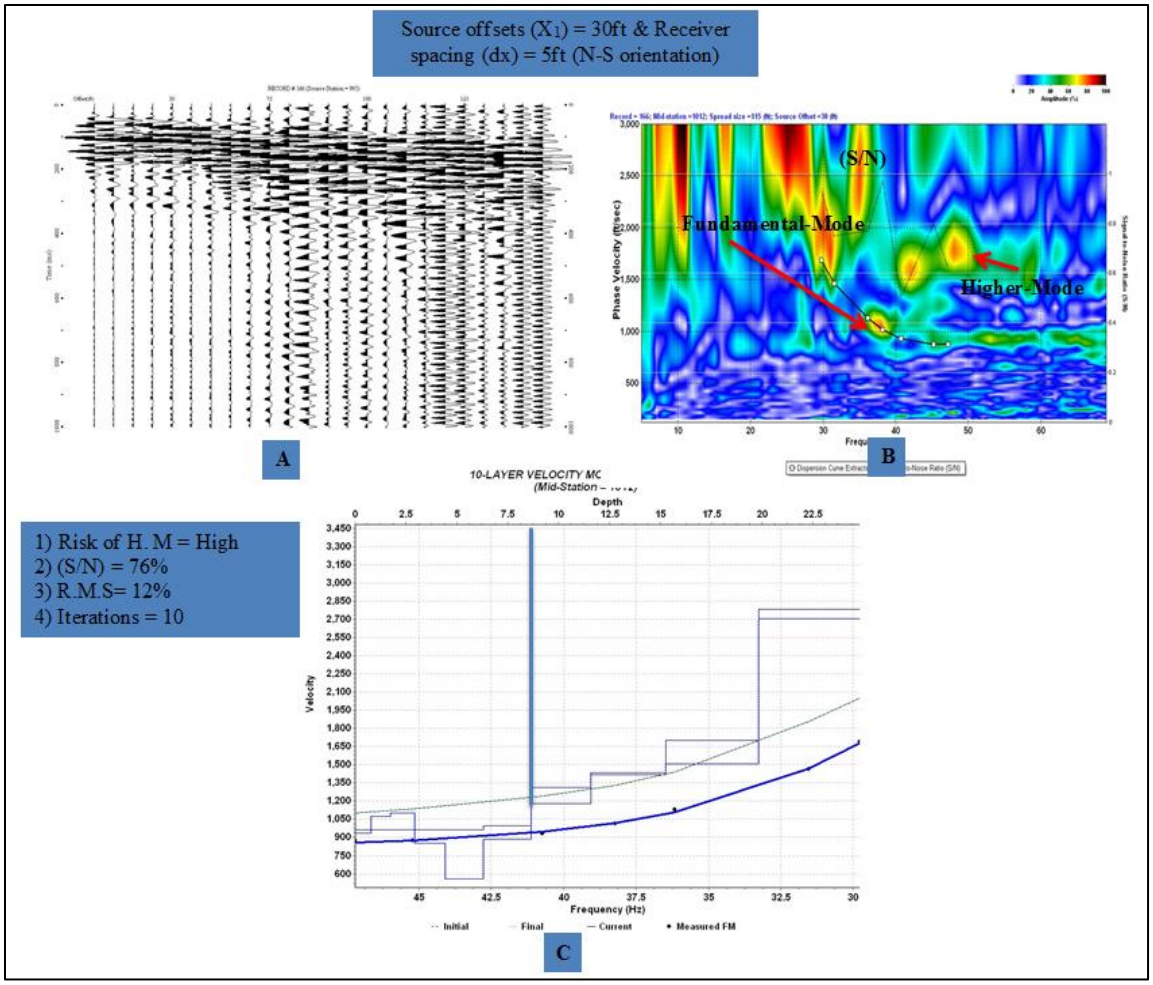

Figure 5.8. MASW survey data collected along Traverse No. 1 oriented north to south array. (A) The 24 channel record (shot gather); (B) The dispersion image (overtone) with superposed dispersion curve (phase velocity versus frequency) where the fundamental mode is quite clear. (C) The 1-D shear wave velocity profile, deduced from the inversion technique. 1) Risk of higher mode; 2) The signal-to-noise ratio (S/N); 3) R.M.S. error; 4) Iterations.

Eight configurations of MASW survey setup were tested. An average dispersion curve was obtained by combining all 8 records using the frequency range from 27 to 54 Hz and the phase velocity range from 805ft/sec to 1,696ft/sec. This process was repeated for all of the receiver array types, with the dominant frequency of the surface waves varied from 30 to 53 Hz for the various array types. An excellent signal-to-noise ratio was obtained for all of the records until a satisfactory match was reached between the

experimental and the theoretical dispersion curves with a relative error of less than 10% to 15%.

The following conditions were common for all three inversions: 1) the 1-D shear-wave velocity profile geometry was defined by ten model blocks (layers) with fixed thicknesses increasing by 5% with depth, plus a model half-space; 2) the depth to the average model half-space was determined as 18.6ft., corresponding to approximately one-third of the maximum resolvable wavelength; 3) a maximum of 8 iterations is possible.

5.1.3. MASW Traverse No. 2 Oriented West-East. Results from dispersion curves and shear wave velocity profiles for all the tested parameters are presented in Table 5.2.

Table 5.2. Results from all the dispersion curves and generated 1- D shear wave velocity profiles for MASW Traverse No. 2. X_1 - source offset; dx - geophone spacing; D - receiver spread length; λ_{max} maximum resolvable Rayleigh wave wavelength; λ_{min} minimum resolvable Rayleigh wave wavelength; Z_{max} penetration depth; S/N - signal-to-noise ratio; RMS -root-mean-square error.

(X_1) (ft.)	dx (ft.)	D (ft.)	Orientation	λmax (ft.)	λmin (ft.)	Velocity, Vphmax/Vphmin (ft./s)	Frequency, *f*min/*f*max (Hz)	Zmax (ft.)	Risk of Higher mode Value	(S/N) (%)	(RMS) Error (%)	Iteration Value (1-30)
10	2.5	57.5	W-E	40	15	1,228-839	31-55	13	High	95	5.2	8
10	5	115	W-E	40	17	1,247-928	31-55	13	High	85	9.0	10
30	2.5	57.5	W-E	43	15	1,670-899	25-53	14	High	98	9.5	10
30	5	115	W-E	42	16	1,221-913	29-58	14	High	94	2.9	10
10	2.5	57.5	N-S	45	13	1,312-834	29-62	15	Moderate	98	2.7	10
10	5	115	N-S	51	16	1,515-900	30-58	17	Moderate	95	10.0	10
30	2.5	57.5	N-S	45	14	1,346-854	30-62	15	Moderate	99	11.0	10
30	5	115	N-S	41	15	1,184-913	29-62	14	High	91	17.0	10

Figure 5.9A displays the MASW data collected along Traverse No. 2 oriented west-east with source offset of 10ft. and geophone spacing of 2.5ft. Phase velocities were

manually picked from the fundamental-mode dispersion curve in Figure 5.9B (represented by white dots) and used for an inversion process to generate a 1-D shear wave velocity model (Figure 5.9C).

The dispersion analysis shows that the data possesses dominant frequencies at approximately f_{min} = 31 Hz to f_{max} = 55 Hz. The phase velocity varied between V_{phmax} = 1,228ft/sec and V_{phmin} = 839ft/sec, corresponding to the Rayleigh waves wavelength of λ_{min} = 13.7ft. and λ_{max} = 40ft. The picked frequency and phase velocity ranges fall within the determined fundamental mode. With these values and the traverse length, the minimum and maximum penetration depths is Z_{max} = 13ft.

These parameters yielded the inverted Vs model that was obtained with the high signal-to-noise ratio (S/N) of 95 % and an RMS error of 5.2 % with eight iterations. The fundamental mode is clearly observable in the absence of higher modes. The dispersion curve is continuous and distinguishable at frequencies higher than 30 Hz. The theoretical dispersion curve matches the experimental curve at higher frequencies. These results can be due to the employed combination of the receiver spread length and the source offset.

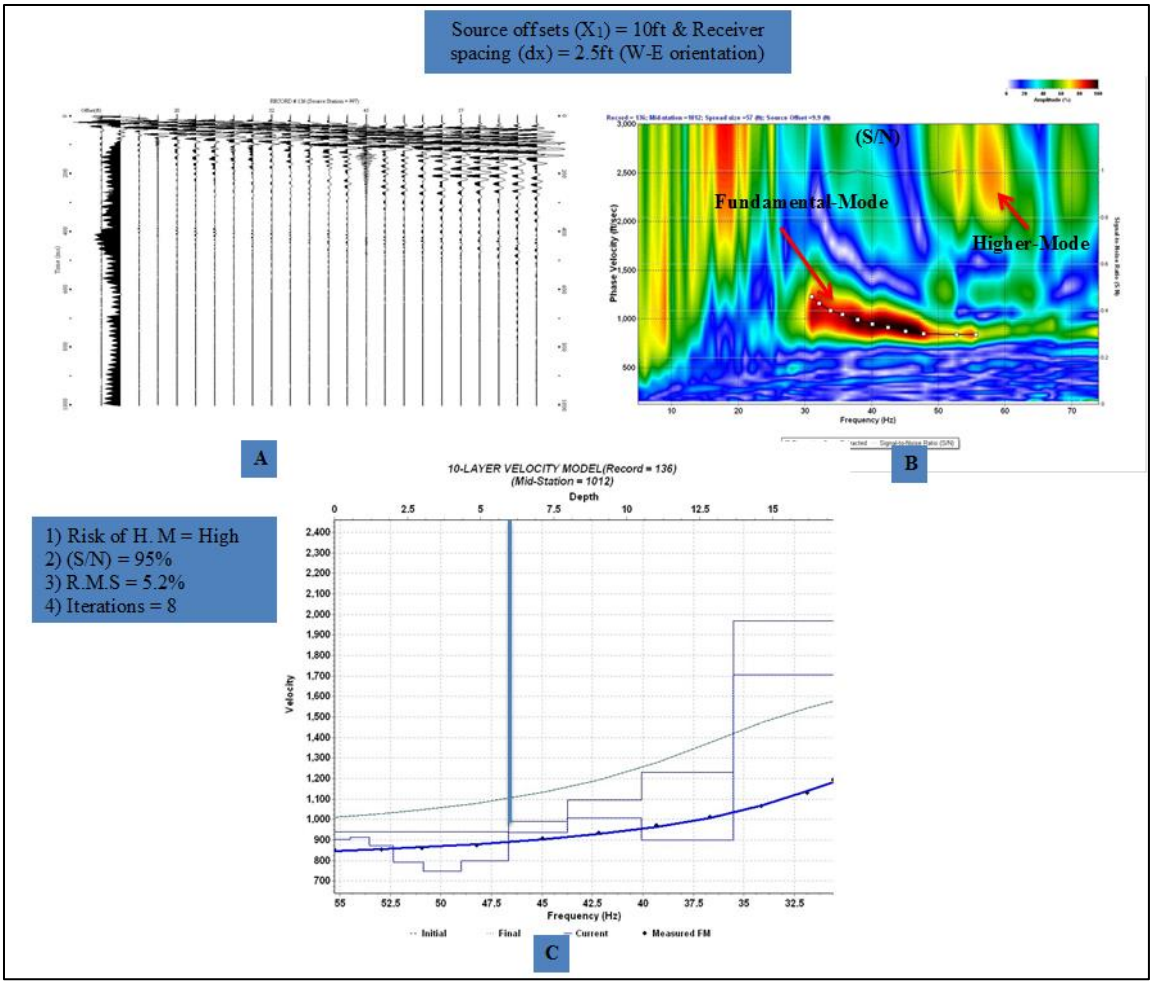

Figure 5.9. MASW survey data collected along Traverse No. 2 oriented west-east array. (A) The 24 channel record (shot gather); (B) The dispersion image (overtone) with superposed dispersion curve (phase velocity versus frequency); (C) The 1-D shear wave velocity profile, deduced from the inversion technique. 1) Risk of higher mode; 2) The signal-to-noise ratio (S/N); 3) R.M.S. error; 4) Iterations.

Figure 5.10A displays the MASW data collected along Traverse No. 2 oriented west-east with source offset of 10ft. and geophone spacing of 5ft. Phase velocities were manually picked using 9 equally spaced points from the fundamental-mode dispersion curve in Figure 5.10B (represented by white dots) and used for an inversion process to generate a 1-D shear wave velocity model (Figure 5.10C).

The dispersion analysis shows that the data possesses dominant frequencies at approximately f_{min}= 31 Hz to f_{max} = 55 Hz. The phase velocity varied between V_{phmax}

= 1,247ft/sec and V_{phmin} = 928ft/sec, corresponding to the Rayleigh waves wavelength of λ_{min} = 17ft. and λ_{max} = 40ft. The picked frequency and phase velocity ranges fall within the determined fundamental mode. With these values and the traverse length, the minimum and maximum penetration depths is Z_{max} = 13ft.

These parameters yielded the inverted Vs model that was obtained with the high signal-to-noise ratio (S/N) of 85 % and an RMS error of 9 % with eight iterations. The fundamental mode is observable in the presence of a higher mode. The dispersion curve is continuous and distinguishable at frequencies higher than 30 Hz. The theoretical dispersion curve matches the experimental curve at higher frequencies. Low quality survey results can be due to the employed combination of the receiver spread length and the source offset.

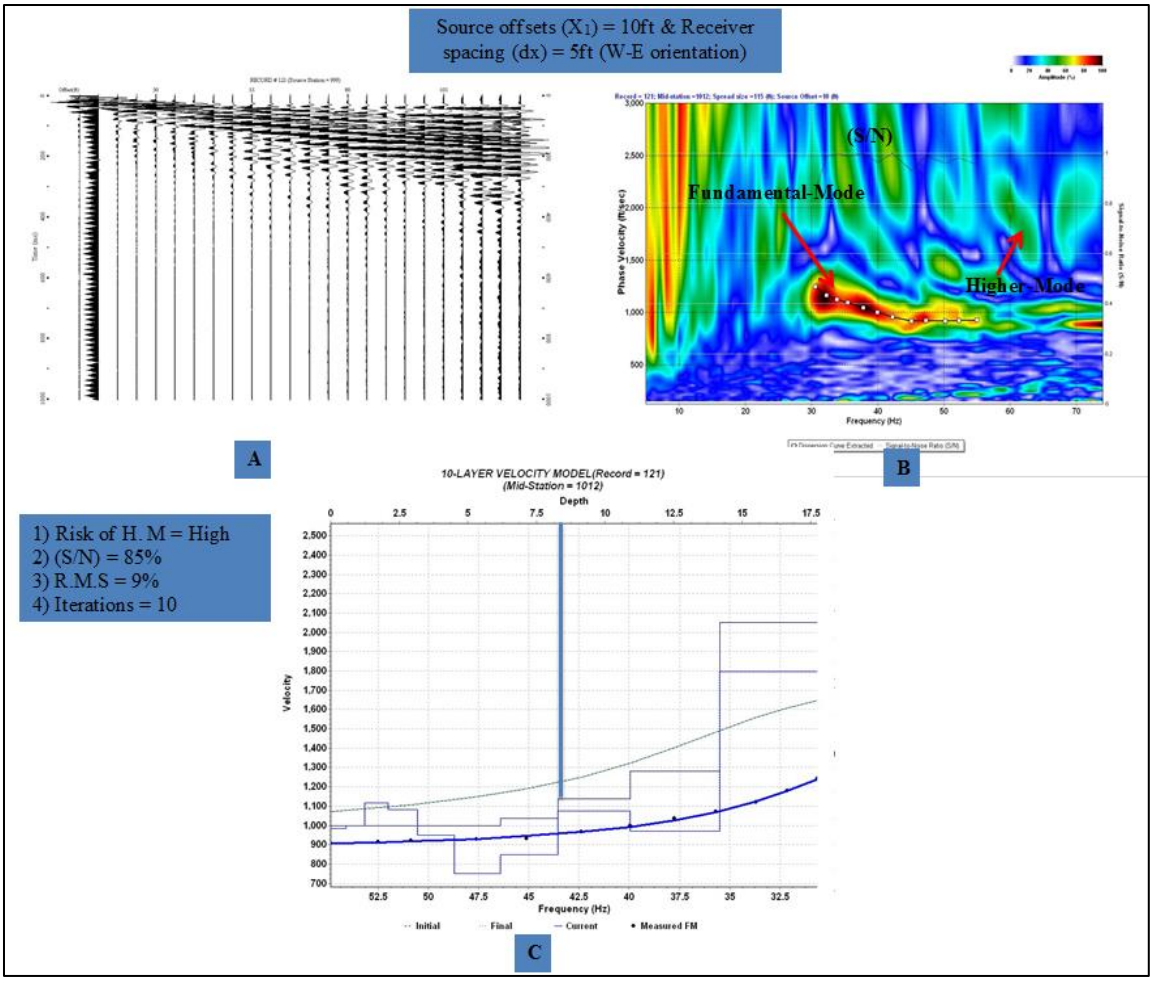

Figure 5.10. MASW survey data collected along Traverse No. 2 oriented west-east array. (A) The 24 channel record (shot gather); (B) The dispersion image (overtone) with superposed dispersion curve (phase velocity versus frequency); (C) The 1-D shear wave velocity profile, deduced from the inversion technique. 1) Risk of higher mode; 2) The signal-to-noise ratio (S/N); 3) R.M.S. error; 4) Iterations.

Figures 5.11 and 5.12 display the MASW data collected along Traverse No. 2 oriented west-east on the basis of the comparison between the MASW survey output for the employed source offset of 30ft. (9.14m) with a receiver spacing of 2.5ft. (0.76m) and the source offset of 30ft. (9.14m) with a receiver spacing of 5ft. (1.52m), respectively. Figures 5.11 and 5.12 show how the various combinations of source offset and geophone spacing can affect the resulting overtone images and extracted dispersion curves for the fundamental and higher modes.

Figure 5.11A displays the MASW data collected along Traverse No. 2 oriented west-east with source offset of 30ft. and geophone spacing of 2.5ft. Phase velocities were manually picked using 9 equally spaced points from the fundamental-mode dispersion curve in Figure 5.11B (represented by white dots) and used for an inversion process to generate a 1-D shear wave velocity model (Figure 5.11C).

The dispersion analysis shows that the data possesses dominant frequencies at approximately f_{min}= 25 Hz to f_{max} = 53 Hz. The phase velocity varied between V_{phmax} = 1,670ft/sec and V_{phmin} = 899ft/sec, corresponding to the Rayleigh waves wavelength of λ_{min} = 15ft. and λ_{max} = 43ft. The picked frequency and phase velocity ranges fall within the determined fundamental mode. With these values and the traverse length, the minimum and maximum penetration depths are Z_{max} = 14ft.

These parameters yielded the inverted Vs model that was obtained with the high signal-to-noise ratio (S/N) of 98 % and an RMS error of 9.5 % with ten iterations. The fundamental mode lacks separation from the higher mode (this overlap might be due to the similarities in phase velocities in that frequency ranges). The dispersion curve is moderately distinguishable at frequencies higher than 30 Hz. The theoretical dispersion curve fairly matches the experimental curve at higher frequencies. Low quality survey results can be due to the employed combination of the receiver spread length and the source offset.

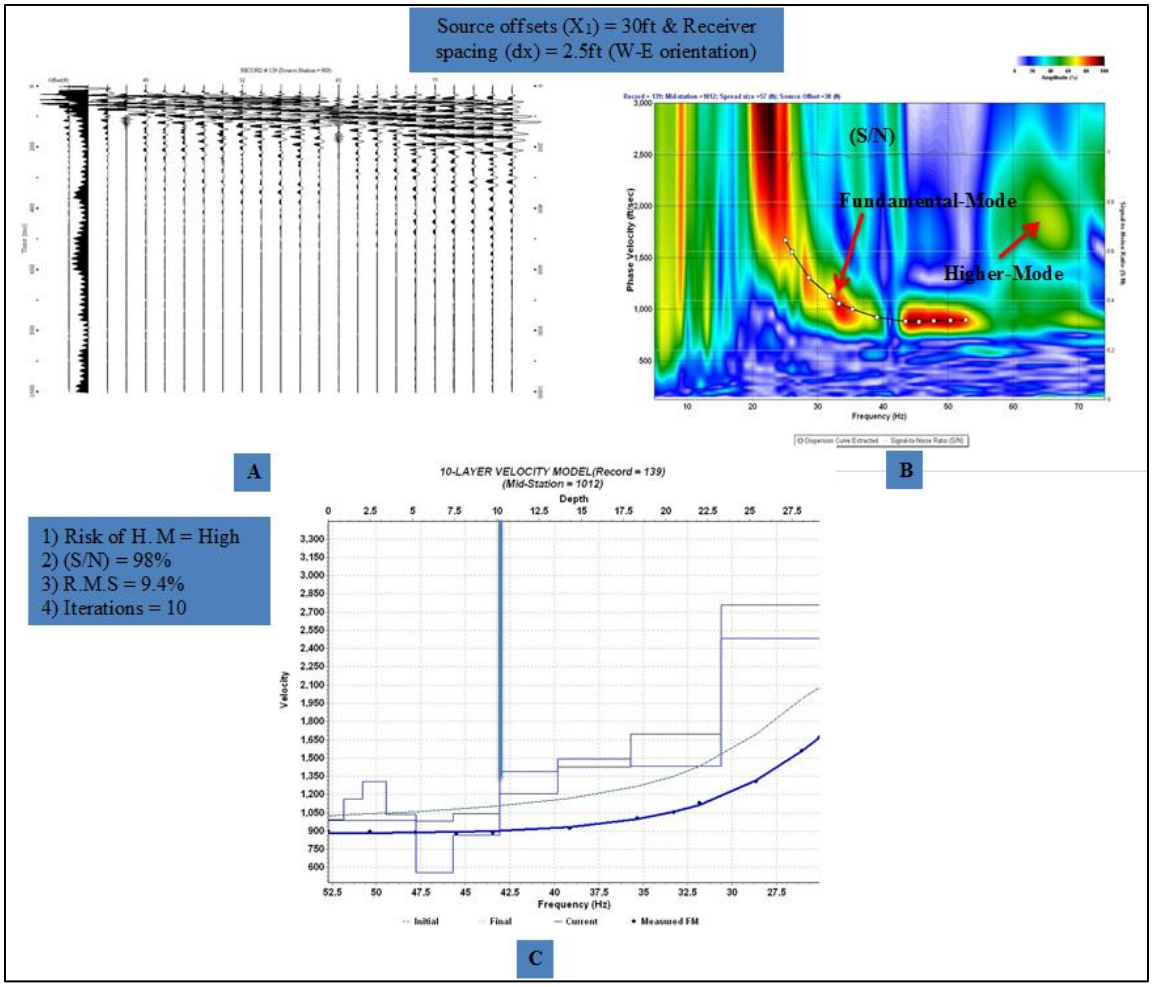

Figure 5.11. MASW survey data collected along Traverse No. 2 oriented west-east array. (A) The 24 channel record (shot gather); (B) The dispersion image (overtone) with superposed dispersion curve (phase velocity versus frequency); (C) The 1-D shear wave velocity profile, deduced from the inversion technique. 1) Risk of higher mode; 2) The signal-to-noise ratio (S/N); 3) R.M.S. error; 4) Iterations.

Figure 5.12A displays the MASW data collected along Traverse No. 2 oriented west-east with source offset of 30ft. and geophone spacing of 5ft. Phase velocities were manually picked using 9 equally spaced points from the fundamental-mode dispersion curve in Figure 5.12B (represented by white dots) and used for an inversion process to generate a 1-D shear wave velocity model (Figure 5.12C).

The dispersion analysis shows that the data possesses dominant frequencies at approximately f_{min}= 29 Hz to f_{max} = 58 Hz. The phase velocity varied between V_{phmax}

= 1,221ft/sec and V_{phmin} = 913ft/sec, corresponding to the Rayleigh waves wavelength of λ_{min} = 15ft. and λ_{max} = 43ft. The picked frequency and phase velocity ranges fall within the determined fundamental mode. With these values and the traverse length, the minimum and maximum penetration depths are Z_{max} = 14ft.

These parameters yielded the inverted Vs model that was obtained with the high signal-to-noise ratio (S/N) of 94 % and an RMS error of 2.9 % with ten iterations. The fundamental mode is visible and can be separated from the higher mode. The dispersion curve is moderately distinguishable at frequencies higher than 30 Hz. The theoretical dispersion curve fairly matches the experimental curve at higher frequencies. Low quality survey results can be due to the employed combination of the receiver spread length and the source offset.

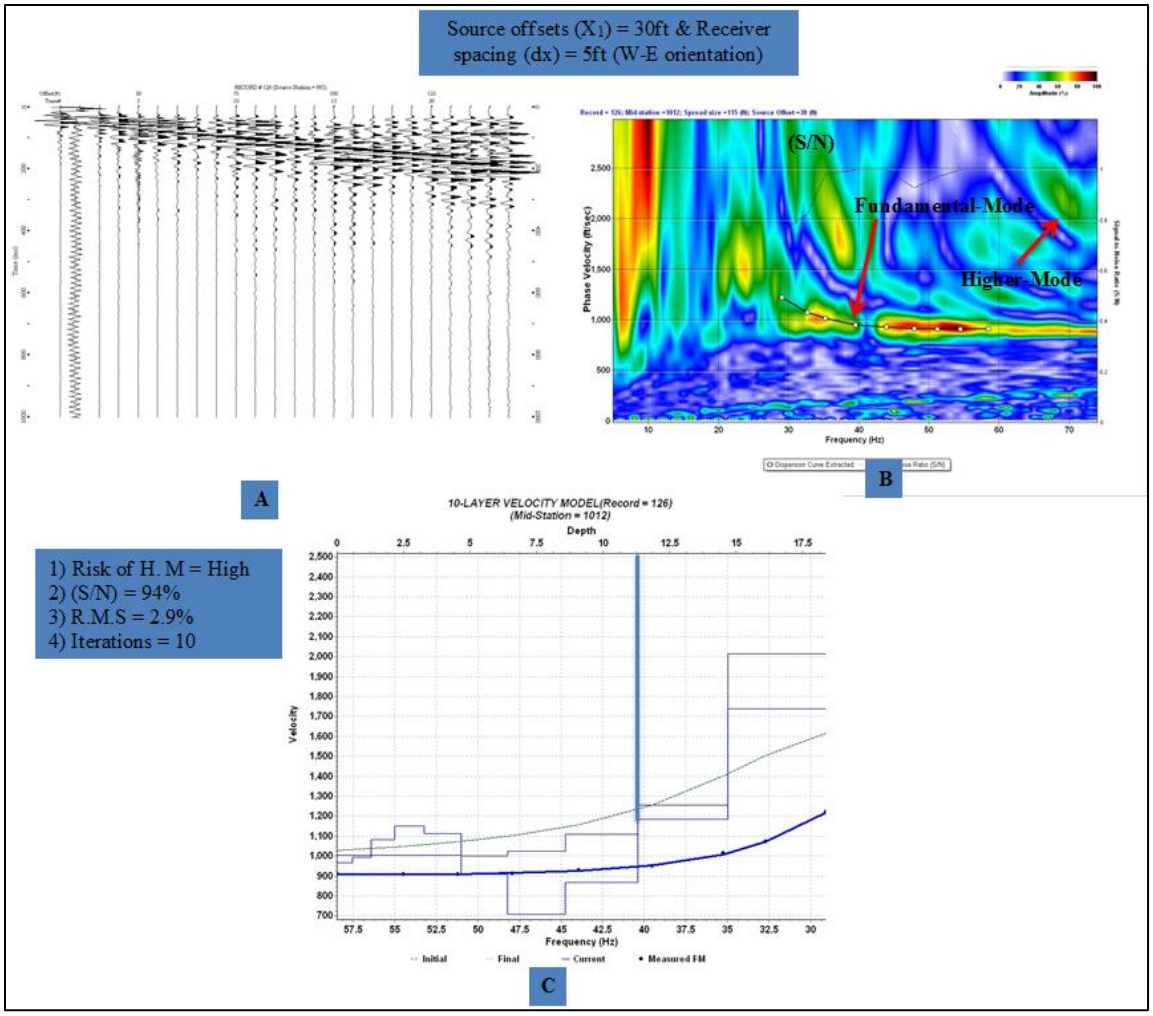

Figure 5.12. MASW survey data collected along Traverse No. 2 oriented west-east array. (A) The 24 channel record (shot gather); (B) The dispersion image (overtone) with superposed dispersion curve (phase velocity versus frequency); (C) The 1-D shear wave velocity profile, deduced from the inversion technique. 1) Risk of higher mode; 2) The signal-to-noise ratio (S/N); 3) R.M.S. error; 4) Iterations.

5.1.4. MASW Traverse No. 2 Oriented North-South. Figure 5.13A displays the MASW data collected along Traverse No.2 oriented north-south with source offset of 10ft. and geophone spacing of 2.5ft. Phase velocities were manually picked using 10 equally spaced points from the fundamental-mode dispersion curve in Figure 5.13B (represented by white dots) and used for an inversion process to generate a 1-D shear wave velocity model (Figure 5.13C).

The dispersion analysis shows that the data possesses dominant frequencies at approximately f_{min}= 29 Hz to f_{max} = 62 Hz. The phase velocity varied between V_{phmax} = 1,312ft/sec and V_{phmin} = 834ft/sec, corresponding to the Rayleigh waves wavelength of λ_{min} = 13ft. and λ_{max} = 55ft. The picked frequency and phase velocity ranges fall within the determined fundamental mode. With these values and the traverse length, the minimum and maximum penetration depths is Z_{max} = 15ft.

These parameters yielded the inverted Vs model that was obtained with the high signal-to-noise ratio (S/N) of 98 % and an RMS error of 2.7 % with ten iterations. The fundamental mode is clearly observable in the absence of higher mods. The dispersion curve is continuous and distinguishable at frequencies higher than 30 Hz. The theoretical dispersion curve matches the experimental curve at higher frequencies. These results can be due to the employed combination of the receiver spread length and the source offset.

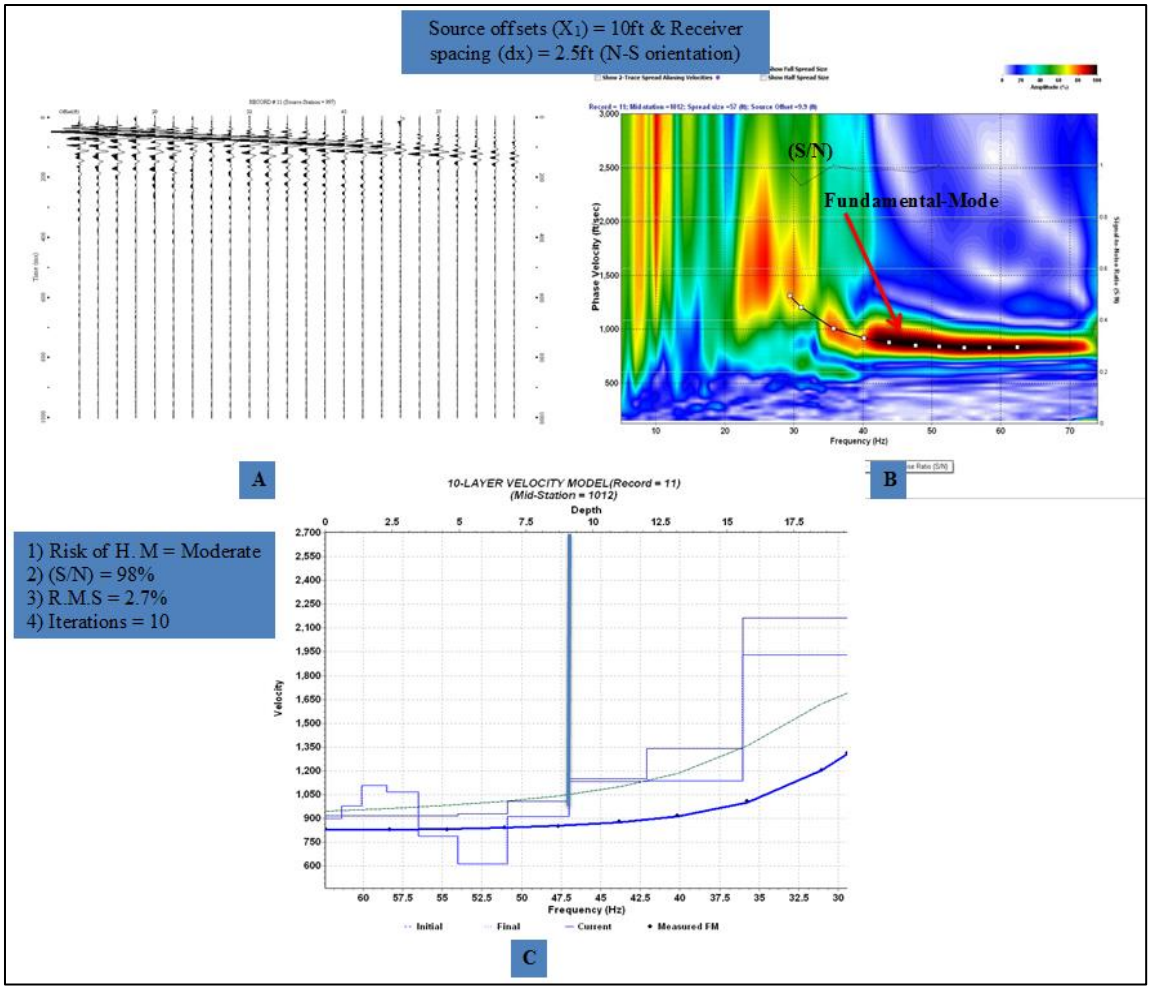

Figure 5.13. MASW survey data collected along Traverse No.2 oriented north to south array. (A) The 24 channel record (shot gather); (B) The dispersion image (overtone) with superposed dispersion curve (phase velocity versus frequency); (C) The 1-D shear wave velocity profile, deduced from the inversion technique. 1) Risk of higher mode; 2) The signal-to-noise ratio (S/N); 3) R.M.S. error; 4) Iterations.

Figure 5.14A displays the MASW data collected along Traverse No.2 oriented north-south with source offset of 10ft. and geophone spacing of 5ft. Phase velocities were manually picked using 9 equally spaced points from the fundamental-mode dispersion curve in Figure 5.14B (represented by white dots) and used for an inversion process to generate a 1-D shear wave velocity model (Figure 5.14C).

The dispersion analysis shows that the data possesses dominant frequencies at approximately f_{min}= 30 Hz to f_{max} = 58 Hz. The phase velocity varied between V_{phmax}

= 1,515ft/sec and V_{phmin} = 900ft/sec, corresponding to the Rayleigh waves wavelength of λ_{min} = 16ft. and λ_{max} = 51ft. The picked frequency and phase velocity ranges fall within the determined fundamental mode. With these values and the traverse length, the minimum and maximum penetration depths is Z_{max} = 17ft.

These parameters yielded the inverted Vs model that was obtained with the high signal-to-noise ratio (S/N) of 95 % and an RMS error of 10 % with ten iterations, the lowest of the eight trials. The fundamental mode is clearly observable in the absence of higher modes. The dispersion curve is continuous and distinguishable at frequencies higher than 30 Hz. The theoretical dispersion curve matches the experimental curve at higher frequencies. These results can be due to the employed combination of the receiver spread length and the source offset.

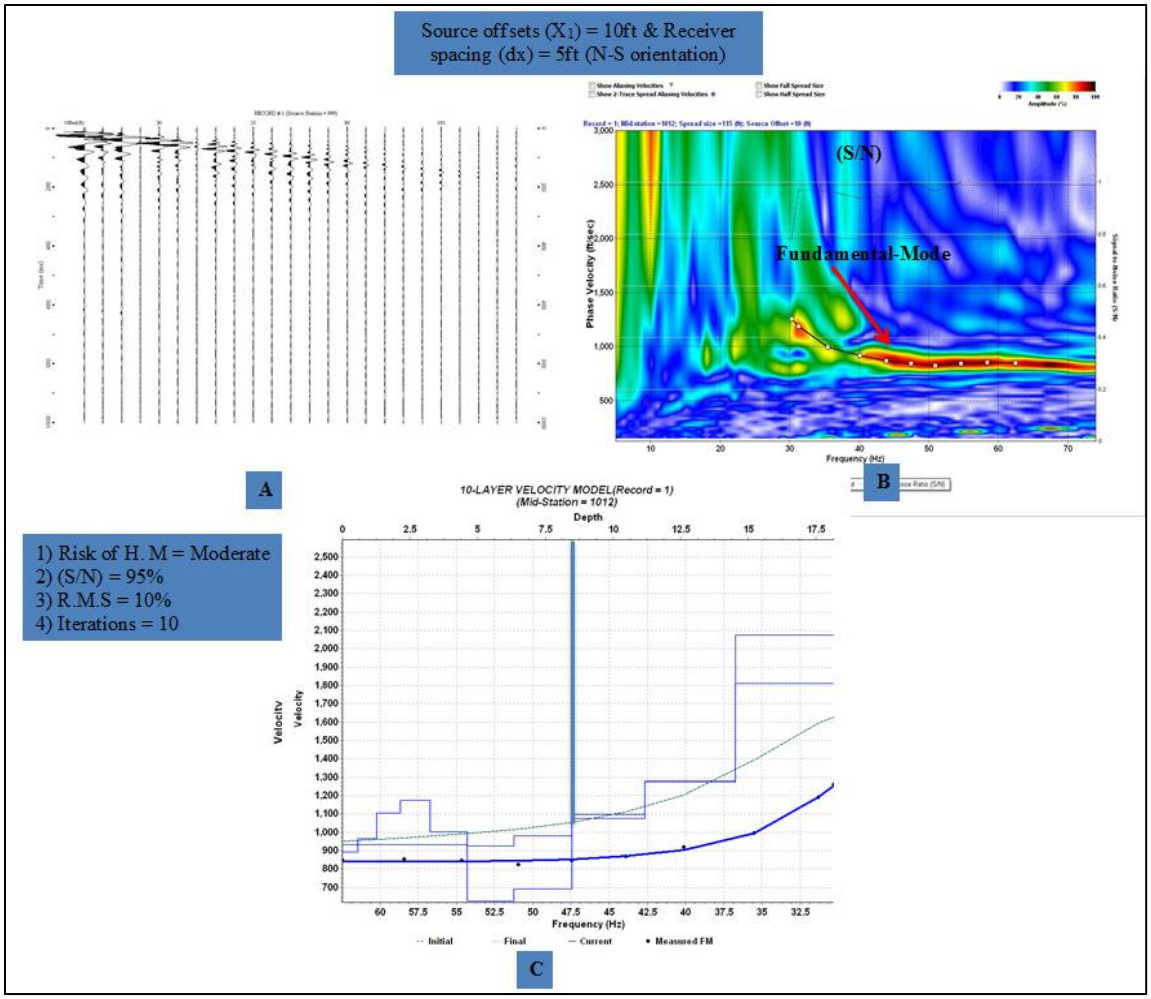

Figure 5.14. MASW survey data collected along Traverse No.2 oriented north to south array. (A) The 24 channel record (shot gather); (B) The dispersion image (overtone) with superposed dispersion curve (phase velocity versus frequency); (C) The 1-D shear wave velocity profile, deduced from the inversion technique. 1) Risk of higher mode; 2) The signal-to-noise ratio (S/N); 3) R.M.S. error; 4) Iterations.

Figures 5.15 and 5.16 display the MASW data collected along Traverse No.2 oriented north-south on the basis of the comparison between the MASW survey output for the employed source offset of 30ft. (9.14m) with a receiver spacing of 2.5ft. (0.76 m) and the source offset of 30ft. (9.14m) with a receiver spacing of 5ft. (1.52m), respectively. Figures 5.15 and 5.16 show how the various combinations of source offset

and geophone spacing can affect the resulting overtone images and extracted dispersion curves for the fundamental and higher modes.

Figure 5.15A displays the MASW data collected along Traverse No.2 oriented north-south with source offset of 30ft. and geophone spacing of 2.5ft. Phase velocities were manually picked using 10 equally spaced points from the fundamental-mode dispersion curve in Figure 5.15B (represented by white dots) and used for an inversion process to generate a 1-D shear wave velocity model (Figure 5.15C).

The dispersion analysis shows that the data possesses dominant frequencies at approximately f_{min}= 30 Hz to f_{max} = 62 Hz. The phase velocity varied between V_{phmax} = 1,346ft/sec and V_{phmin} = 854ft/sec, corresponding to the Rayleigh waves wavelength of λ_{min} = 14ft. and λ_{max} = 45ft. The picked frequency and phase velocity ranges fall within the determined fundamental mode. With these values and the traverse length, the minimum and maximum penetration depths is Z_{max} = 15ft.

These parameters yielded the inverted Vs model that was obtained with the high signal-to-noise ratio (S/N) of 99 % and an RMS error of 11 % with ten iterations. The fundamental mode is clearly observable in the absence of higher modes. The dispersion curve is continuous and distinguishable at frequencies higher than 30 Hz. The theoretical dispersion curve matches the experimental curve at higher frequencies. These results can be due to the employed combination of the receiver spread length and the source offset.

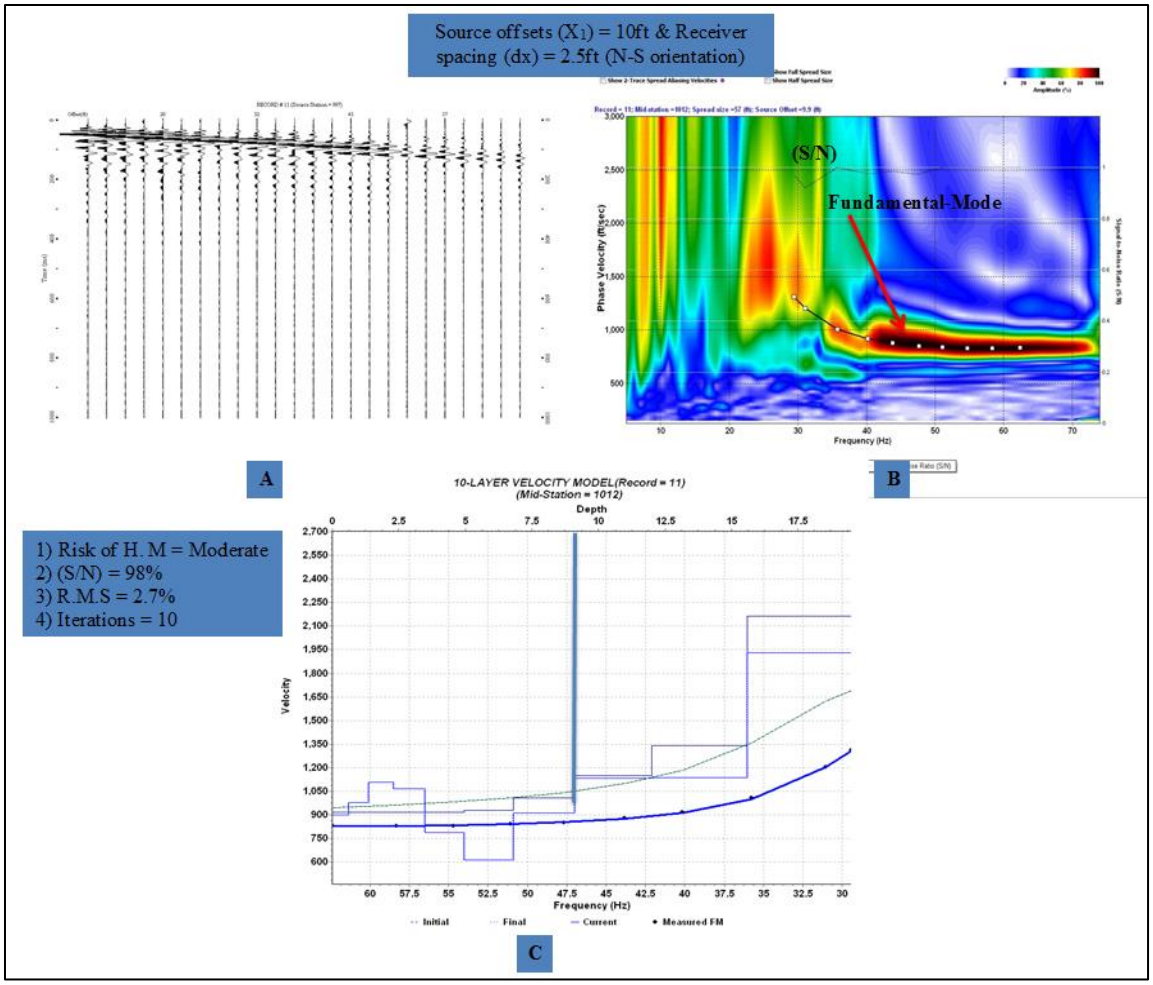

Figure 5.15. MASW survey data collected along Traverse No.2 oriented north to south array. (A) The 24 channel record (shot gather); (B) The dispersion image (overtone) with superposed dispersion curve (phase velocity versus frequency); (C) The 1-D shear wave velocity profile, deduced from the inversion technique. 1) Risk of higher mode; 2) The signal-to-noise ratio (S/N); 3) R.M.S. error; 4) Iterations.

Figure 5.16A displays the MASW data collected along Traverse No.2 oriented north-south with source offset of 30ft. and geophone spacing of 5ft. Phase velocities were manually picked using 9 equally spaced points from the fundamental-mode dispersion curve in Figure 5.16B (represented by white dots) and used for an inversion process to generate a 1-D shear wave velocity model (Figure 5.16C).

The dispersion analysis shows that the data possesses dominant frequencies at approximately f_{min}= 29 Hz to f_{max} = 62 Hz. The phase velocity varied between V_{phmax}

= 1,184ft/sec and V_{phmin} = 913ft/sec, corresponding to the Rayleigh waves wavelength of λ_{min} = 15ft. and λ_{max} = 41ft. The picked frequency and phase velocity ranges fall within the determined fundamental mode. With these values and the traverse length, the minimum and maximum penetration depths is Z_{max} = 14ft.

These parameters yielded the inverted Vs model that was obtained with the high signal-to-noise ratio (S/N) of 91 % and an RMS error of 17 % with ten iterations. The fundamental mode lacks separation from the higher mode (this overlap might be due to the similarities in phase velocities in that frequency ranges). The dispersion curve is non-coherent at frequencies higher than 30 Hz. The theoretical dispersion curve fairly matches the experimental curve at higher frequencies. Low quality survey results can be due to the employed combination of the receiver spread length and the source offset.

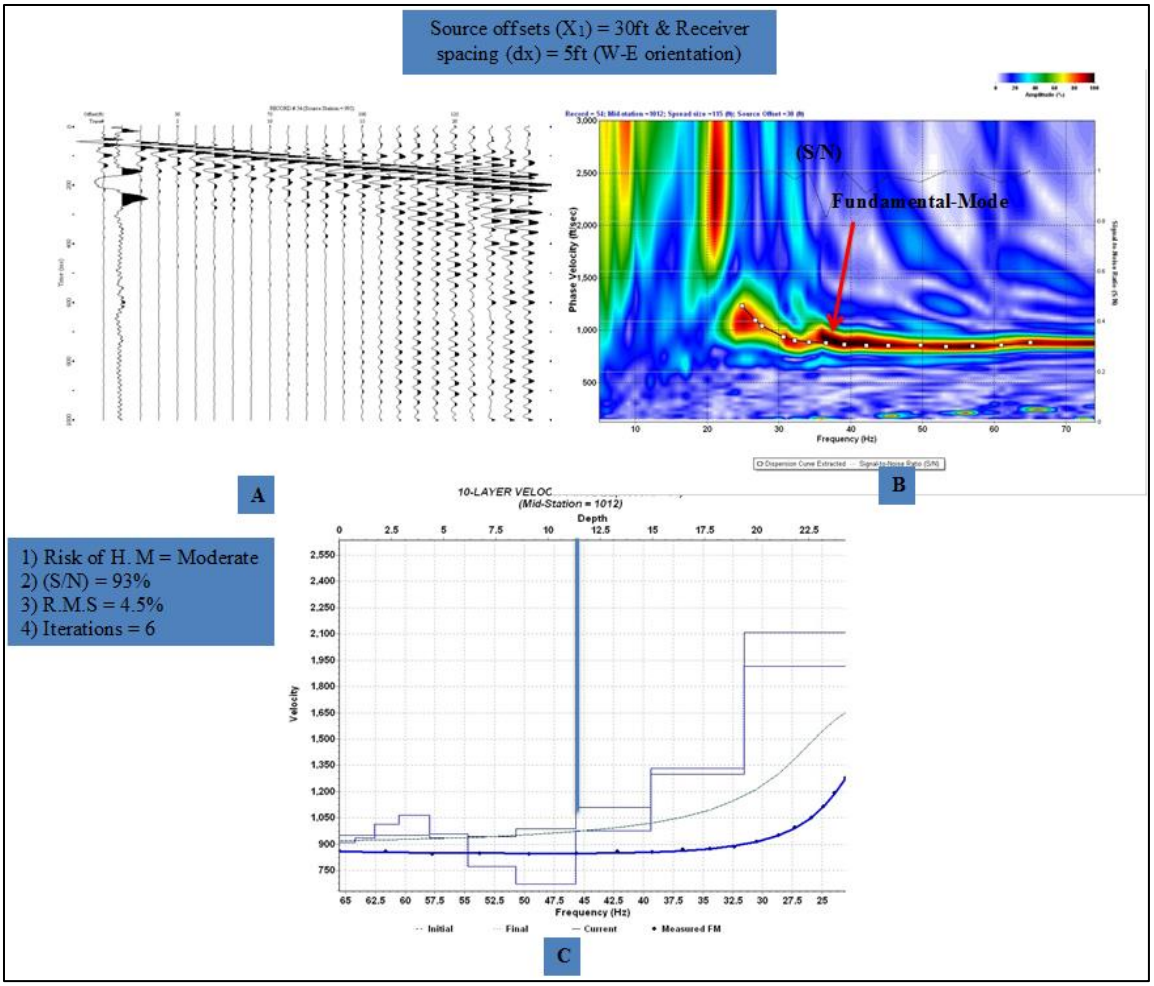

Figure 5.16. MASW survey data collected along Traverse No.2 oriented north to south array. (A) The 24 channel record (shot gather); (B) The dispersion image (overtone) with superposed dispersion curve (phase velocity versus frequency); (C) The 1-D shear wave velocity profile, deduced from the inversion technique. 1) Risk of higher mode; 2) The signal-to-noise ratio (S/N); 3) R.M.S. error; 4) Iterations.

Eight configurations of MASW survey setup were tested. An average dispersion curve was obtained by combining all 8 records using the frequency range from 29 to 62 Hz and the phase velocity range from 834 ft/s to 1,541 ft/s. This process was repeated for all of the receiver array types, with the dominant frequency of the surface waves varied from 30 to 53 Hz for the various array types. An excellent signal-to-noise ratio was obtained for all of the records until a satisfactory match was reached between the

experimental and the theoretical dispersion curves with a relative error of less than 10% to 15%.

The following conditions were common for all three inversions: 1) the 1-D shear-wave velocity profile geometry was defined by ten model blocks (layers) with fixed thicknesses increasing by 5% with depth, plus a model half-space; 2) the depth to the average model half-space was determined as 15ft., corresponding to approximately one-third of the maximum resolvable wavelength; 3) a maximum of 9.7 iterations is possible.

When a satisfactory match is reached between the experimental and the numerical dispersion curves (usually with a relative error of less than 10% to 15%), then the Vs profile has been found and the researcher can proceed with determining the seismic subsurface classification.

Generally, velocity values of less than 1,200ft/sec (366m/sec) are interpreted as sand and unconsolidated material, while velocity values greater than 1,200ft/s (366m/s) are interpreted as soft, weathered limestone.

5.2. DISPERSION OF RESOLUTION CURVE

Resolution of dispersion curve is another important factor in determining quality of MASW data. The resolution along the velocity axis defines the ability to discriminate a particular phase velocity from other velocities for a given frequency. The resolution along the frequency axis determines the ability to discriminate a particular frequency from other frequencies for a given velocity. The dispersion curve width is related to the relationship between the frequency and the velocity of the surface waves.

To determine the resolution of the dispersion image in the frequency-velocity domain (f-v), the length of the receiver spread needs to be increased (Park et al., 1998). Forbriger (2003a) provided an analytical result to assess the resolution of the dispersion image based on the Equation (5.1).

$$\Delta d = 1 / f D \tag{5.1}$$

where Δd is the half-width between the neighboring minimum of dispersion energy in the (f-v) domain, f is the frequency, and D is the length of the receiver array. However, then understand that the resolution of the dispersion image could vary with the algorithms that were used to generate the dispersion image in the frequency-velocity domain. A current comparison of several different algorithms can be found in (Dal Moro et al., 2003).

Three to five impacts generated by a 20 lb. sledgehammer were vertically stacked at each MASW location using SurfSeis software developed by KGS. A record length of 2,048 milliseconds at a 1-millisecond sampling rate interval was employed.

The influence of these factors on the analysis is highly dependent on the data quality such as high or low the signal-to-noise ratio, the confidence of dispersion curve extraction, the R.M.S. error and the maximum number of iterations. A “good” quality data set suggests the surface-wave energy is the most prominent seismic event in the seismic record (i.e., the highest S/N), whereas a “bad” quality data sets are usually contaminated by noise.

The quality of the acquired surface wave records can be evaluated in terms of the resolution of the phase velocity spectrum, i.e., the sharpness of the amplitude peaks

observed at each frequency, the extractable frequency range and the continuity of the fundamental mode high-amplitude band.

The quality of a dispersion curve is judged according to two criteria: the signal-to-noise ratio and the general dispersion curve direction. A high S/N indicates a high confidence in the obtained phase velocity. An S/N higher than 0.5 or more than 55% is considered acceptable.

The quality of the MASW data can also be affected by natural geologic conditions that may not produce well-defined dispersion curves and cannot be used to calculate reliable shear-wave velocity models, only on the basis of the comparison between the nearest source offset and variable receiver spacings. After that, the comparison between the farther source offset and variable receiver spacings.

Two configurations of MASW geophone array results were generated with the data Figure 5.17. The first nearest source offset was (X_1) = 10ft. with a receiver spacing of (dx) = 2.5ft., and the second nearest source offset was (X_1) = 10ft. with a receiver spacing of (dx) = 5ft.

The output of two different MASW array configurations are shown in Figure 5.17. Figure 5.17A and 5.17B show seismic field records collected using geophone spacing of 2.5ft. (0.76m) with corresponding dispersive image; Figures 5.17 C and 5.17D show seismic field records collected using geophone spacing of 5ft. (1.52m) with corresponding dispersive image. For the estimation of dispersion curve resolution, a double-ended arrow at frequencies of 30 Hz and 50 Hz is superposed over the dispersion image. The double-ended arrow at 30 Hz is twice as long as that at 50 Hz. This is determined by Equation (5.1) that indicates the resolution of the dispersion image is one-

half at 30 Hz compared with that at 50 Hz. For Figures 5.17C and 5.17D, the resolution reduction of one-half (Δd is doubled) as shown in Figure 5.17D was expected. The double-ended arrows in Figures 5.17A and 5.17B at 30 and 50 Hz are longer than 60%, not 100% like the arrows in Figure 5.17C and 5.17D at 30 and 50 Hz, respectively.

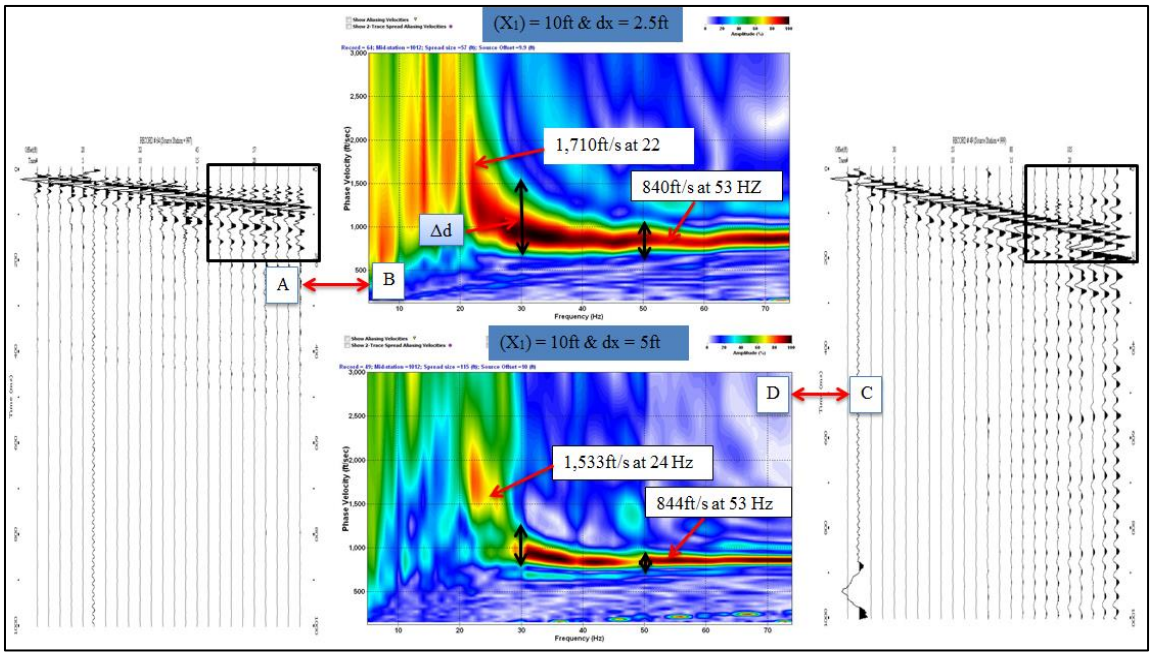

Figure 5.17. The multichannel seismic record; (B) Corresponding overtone image in which the fundamental mode dispersion is identified; (C) The multichannel seismic record collected with doubled receiver spacing; (D) Corresponding overtone image in which the fundamental mode dispersion is identified with noticeable discrepancies.

The third and fourth MASW array configurations are shown in Figure 5.18. The third farthest source offset was 30 ft. (9.14m) with a receiver spacing of 2.5 ft. (0.76m), and the fourth farthest source offset was 30 ft. (9.14m) with a receiver spacing of 5ft. (1.52m).

The output of the third and fourth MASW array configurations are shown in Figure 5.18. Figure 5.18A and 5.18B show seismic field records collected using geophone spacing of 2.5ft. (0.76m) with corresponding dispersive image; Figures 5.18C

and 5.18D show seismic field records collected using geophone spacing of 5ft. (1.52m) with corresponding dispersive image. For the estimation of dispersion curve resolution, a double-ended arrow at frequencies of 30 Hz and 50 Hz is superposed over the dispersion image. The double-ended arrow at 30 Hz is twice as long as that at 50 Hz. Both double-ended arrows in Figure 5.18C and Figure 5.18D at 30 and 50 Hz were the same length lengths, which also supports Equation (5.1) in that the resolution of the dispersion image is determined by the length of the receiver array and the receiver spacing. Also, the resolution (indicated by a double-ended arrow around the frequency of 30 Hz) of the dispersive energy from the data with the farther source offset of 30ft. (9.14m) is better than that of the data generated from seismic record collected with the nearest source offset of 10ft. (3.04m).

As demonstrated by previous examples, Equation (5.1) might work well as the frequency changes when the length of the receiver array is fixed. Furthermore, it is usually necessary to double the length of the receiver array for a given frequency, and the resolution increase is normally less than 90%. A comparison of the resolution of dispersion image generated from seismic record collected with the father source offset of 30 ft. (9.14m) at both Figures 5.18c and 5.18d is much better than in Figures 5.18a and 5.18B, and the double-ended arrow is 10% shorter than on the data acquired with the nearest source offset of 10ft. (3.04m) as it shown in Figure 5.18B and 5.18D.

Analytically, it can be shown that the width of a dispersion curve depends on the difference between the true phase velocity and the assumed phase velocity. If the integrative energy rapidly decreases with the difference in velocity, the bandwidth would be relatively narrow, giving a relatively well-defined velocity range that can be regarded

as the phase velocity. The relationship between the energy bandwidth and the phase range of the harmonic waves facilitates an understanding of how the bandwidth varies with phase velocity, frequency and source distance.

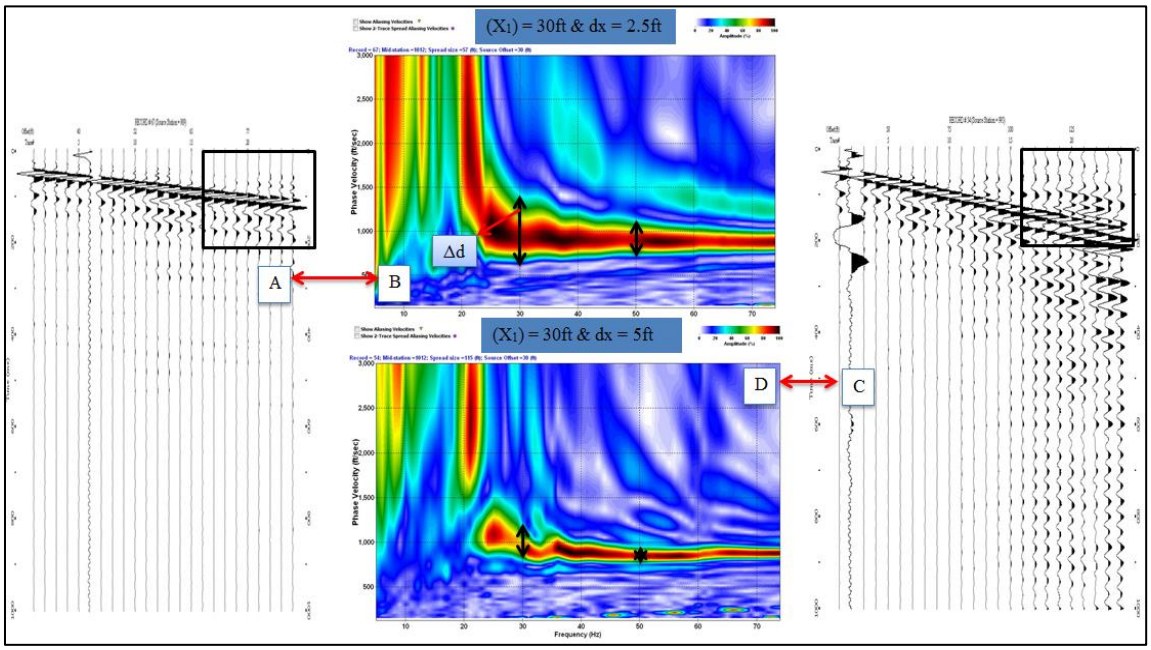

Figure 5.18. (A) The multichannel seismic record; (B) Corresponding overtone image in which the fundamental mode dispersion is identified; (C) The multichannel seismic record collected with doubled receiver spacing; (D) Corresponding overtone image in which the fundamental mode dispersion is identified with visible distortion.

Figure 5.19 displays 4 dispersion images (overtones) deduced from the surface wave records collected using various MASW array configurations. Figure 5.19A displays dispersion curve extracted from fundamental mode of overtone image generated for the seismic record collected with source offset of 10ft. (3.05m) and a receiver spacing of 2.5 ft. (0.76m), the longest Rayleigh wave wavelength of λmax = 1,663ft/sec/26 Hz = 64ft., the minimum phase velocity of $C_R min$ = 827ft/sec and a difference between the maximum and minimum phase velocities of Δ_{CR} = 1,663ft/sec - 827ft/sec = 836ft/sec. Therefore, the suggested optimum offset A would be 16ft.

Figure 5.19B displays dispersion curve extracted from fundamental mode of dispersion image generated for the seismic record collected with source offset of 10ft. (3.05m) and a receiver spacing of 5ft., the longest Rayleigh wavelength of λmax = 1,220ft/sec/31 Hz = 39ft., the minimum phase velocity of CRmin = 850 ft/sec and a difference between the maximum and minimum phase velocities of Δ_{CR} = 1,220ft/sec - 850ft/sec = 370ft/sec. Therefore, the suggested optimum offset A would be 22.3ft.

High level of Rayleigh waves coherency was noticed during comparison of Figures 5.19a and 5.19b. It was observed that the data acquired with a configuration of the first nearest offset of 10ft. (3.04m) and a receiver spacing of 2.5ft. (0.61m) considered a better quality than that from the second nearest offset of 10ft. and a receiver spacing of 5ft. (1.52m). The continuity is even clearer for data in a rectangular window (especially for frequencies lower than 30 Hz).

Figure 5.19C displays dispersion curve extracted from fundamental mode of dispersion image generated for the seismic record collected with source offset of 30ft. (9.14m) and a receiver spacing of 2.5ft. (0.61m), the longest Rayleigh wavelength of λmax = 1,699ft/sec/25 Hz = 68ft. (20.72m), a minimum phase velocity of C_{Rmin} = 855ft/sec and a difference between the maximum and minimum phase velocities of Δ_{CR} = 1,699ft/sec - 855ft/sec = 844ft/sec. Therefore, the suggested optimum offset A would be 17.2ft. (5.18m).

Figure 5.19D displays dispersion curve extracted from fundamental mode of dispersion image generated for the seismic record collected with source offset of 5ft. (1.52m), the longest Rayleigh wavelength of λmax = 1,546ft/sec/26 Hz = 59ft. (17.98 m), a minimum phase velocity of C_{Rmin} = 904ft/sec and a difference between the maximum

and minimum phase velocities of Δ_{CR} = 1,546ft/sec - 904ft/sec = 642ft/sec. Therefore, the suggested optimum offset A would be 20.7ft. (6.01m).

After comparing all of the results, high level of Rayleigh waves coherency was noticed in the data acquired from the nearest offset of 10ft. and a receiver spacing of 2.5ft. (0.61m) and the farthest offset of 30ft. (9.14m) and a receiver spacing of 2.5ft. (0.61m) than with the farther offset of = 30ft. (9.14m) This is the most reliable method of dispersion imaging with the lowest number of computational artifacts.

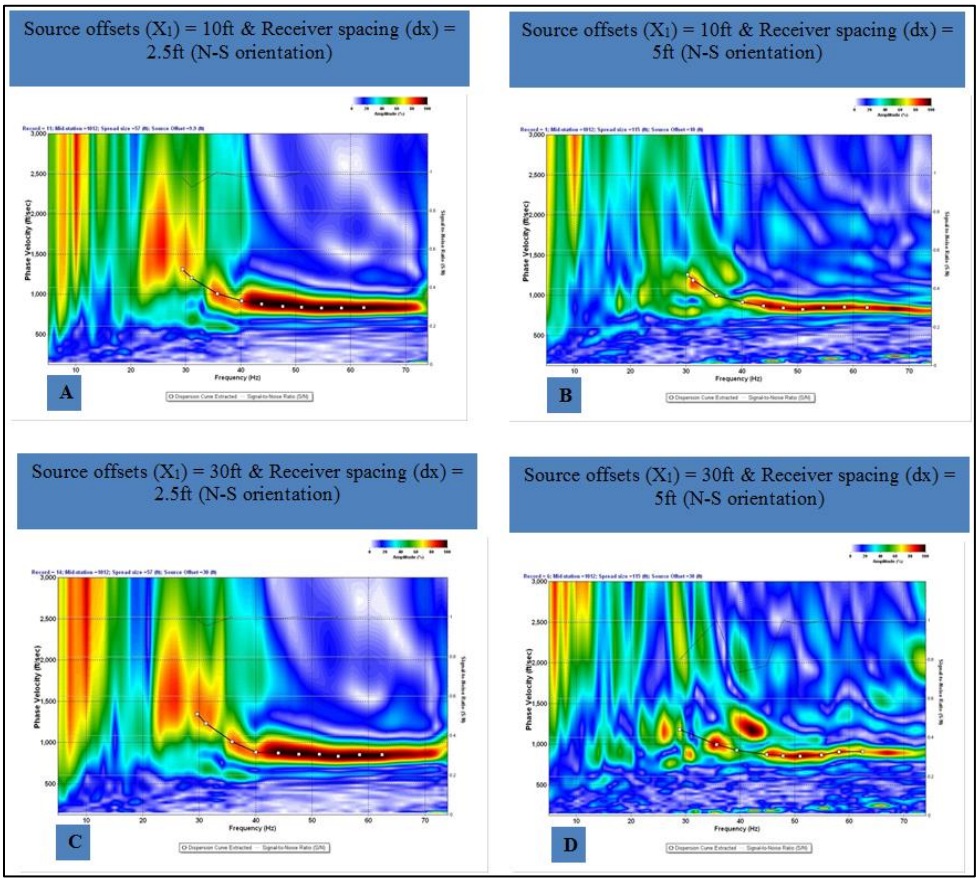

Figure 5.19. Dispersion images (overtones) deduced from the surface wave records collected using various MASW array configurations (north to south orientation).

Similar analysis was performed for W-E oriented arrays (Figure 5.20). It was also noticed that the overal quality of overtone images obtained by using west to east oriented arrays are slightly poorer in terms of continuity of dispersion curve. This can be attributed to the irregularity of the depth to top of rock. As the dominant solutuon widening joints trend north-south in the study area, qulity of MASW data acquired perpendicular to the structural trends is porrer due to the significant relief along the geophone array.

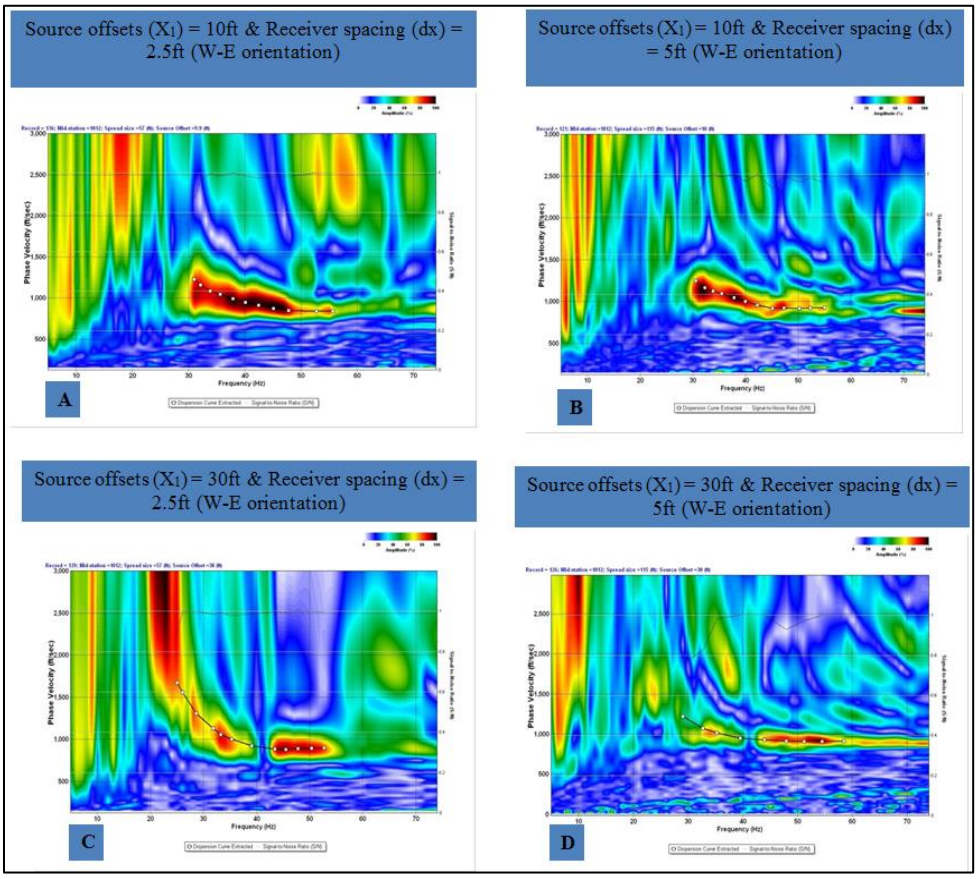

Figure 5.20. Dispersion images (overtones) deduced from the surface wave records collected using various MASW array configurations (west to east orientation).

5.3. COMPARISON OF 1-D SHEAR-WAVE VELOCITY PROFILES

The variable increases in shear-wave velocity with depth were attributed to fracturing of the limestone bedrock. Generally, high shear-wave velocities are indicative of limestone bedrock. Fracture zones and highly weathered bedrock are typically attributed to the shear-wave velocities between 1,200 and 2,500ft/sec. Burlington-Keokuk limestone in the study area has shear-wave velocities between 2,000 and 2,500 ft/sec, so observed velocities may also be relevant to another limestone type with similar lithology.

Data collected using four MASW array configurations were analyzed. The first and second data sets were acquired using the source offsets of 10ft. (3.04m) with a receiver spacing of 2.5ft. (0.76m) and 5ft. (1.52m), respectively. The third and fourth data sets were acquired using the source offset of 30 ft. (9.14m) with a receiver spacing of 2.5ft. (0.76m) and 5ft. (1.52m), respectively.

Figures 5.21 and 5.22 display the comparison of 1-D shear-wave velocity profiles, deduced using the inversion technique from the seismic data sets collected with various configurations of active MASW array. Table 5.3 lists the average Vs values for the top 4ft. (1.22m), 12.5ft. (3.81m), and 27.5ft. (8.38m) depths for one site.

Vs profiles were generated from seismic records acquired with different source offsets and receiver spacings that were oriented from west to east. The 1-D shear-wave velocity profiles obtained with different types of configuration of MASW array configurations are shown in Figure 5.21. The variation of the Vs velocities at all depths seems to be fairly consistent for all array configurations. The depth to the top of rock can be identified at a depth of around 12.5ft. (3.81m) from the data collected with all array configurations.

Table 5.3. Average Vs at ten 1-D shear-wave velocity profiles. No.1.

(X_1) (ft.)	dx (ft.)	D (ft.)	Orientation	Velocity (ft./s) 4ft.	Velocity (ft./s) 12.5ft.	Velocity (ft./s) 27.5ft.
10	2.5	57.5	W-E	1,134	1,334	2,066
10	5	115	W-E	1,446	1,049	1,522
30	2.5	57.5	W-E	852	1,376	2,154
30	5	115	W-E	1,526	1,241	1,172
10	2.5	57.5	N-S	1,320	1,188	1,404
10	5	115	N-S	1,034	1,523	1,550
30	2.5	57.5	N-S	659	1,260	1,221
30	5	115	N-S	1,270	949	1,306

A comparison of 1-D shear wave velocity profiles generated up to a depth of 32.5ft. (9.9m) shows the following results:

a) All of the profiles start with a thin layer (from 1 to 4ft. [0.3 – 1.22m] thick) and are characterized by average shear wave velocities between 1,070 and 1,240ft./s) for the data collected with all array configurations. This high-velocity layer is most probably observed due to the combination of stiff subsurface materials (reddish-brown clay with admixed chert fragments, alternating from fine to coarse grained with occasional stylolites and fossils).

b) There is a low velocity layer observed on depths of 11.5 - 12.5ft. (3.5 – 3.81m) with corresponding shear wave velocities range between 1,230 and 1,250ft./s which is confidently determined in the most profiles. This layer is attributed to the top of rock (represented by Burlington-Keokuk limestone).

c) At a depth of approximately 27.5ft. (8.38m), corresponding 1-D shear wave velocity values increase gradually until the depth of 32.5ft. (9.9m) from 1370ft/sec to 1729ft/sec in all MASW profiles.

d) It can also be observed from the Vs profiles that there is a slight decrease in the velocities for the data sets collected using the farthest source offset of 30ft. (9.14m) and longer receiver spacing of 5ft. (1.52m) at a depth of approximately 27.5ft. (8.38m). Decrease in velocities from 1,729ft/sec to 2,066ft/sec were observed for the data sets collected using the nearest offset of 10ft. (3.04m) for the data sets collected in west-east direction and approximately 1,370ft/sec to 1,404ft/sec for the data sets collected in north-south direction.

e) This decrease in velocity values may correspond to the presence of either clay or saprolite formation above the bedrock. Also, the highest velocity found in the inversion was around 1,200 to 2,500ft/sec which are indicative of bedrock, which is characterized by calcareous shale with some limestone interbeds. A reasonable correlation between the MASW data sets collected with opposite array orientation was observed. Generally, extraction of dispersion curves from the overtone images generated from seismic records collected in west-east or north-south direction provided results of similar quality. That can be explained by the heterogeneity of subsurface.

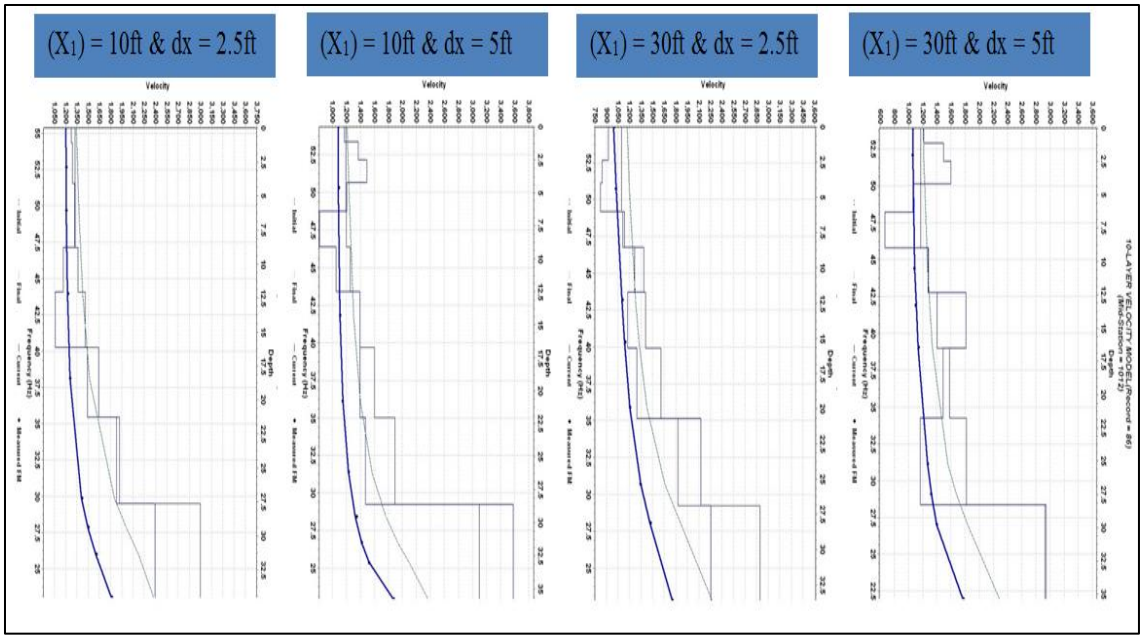

Figure 5.21. Comparison of 1-D shear wave velocity profiles, deduced using the inversion technique from the seismic data sets collected with various configurations of active MASW oriented west to east array.

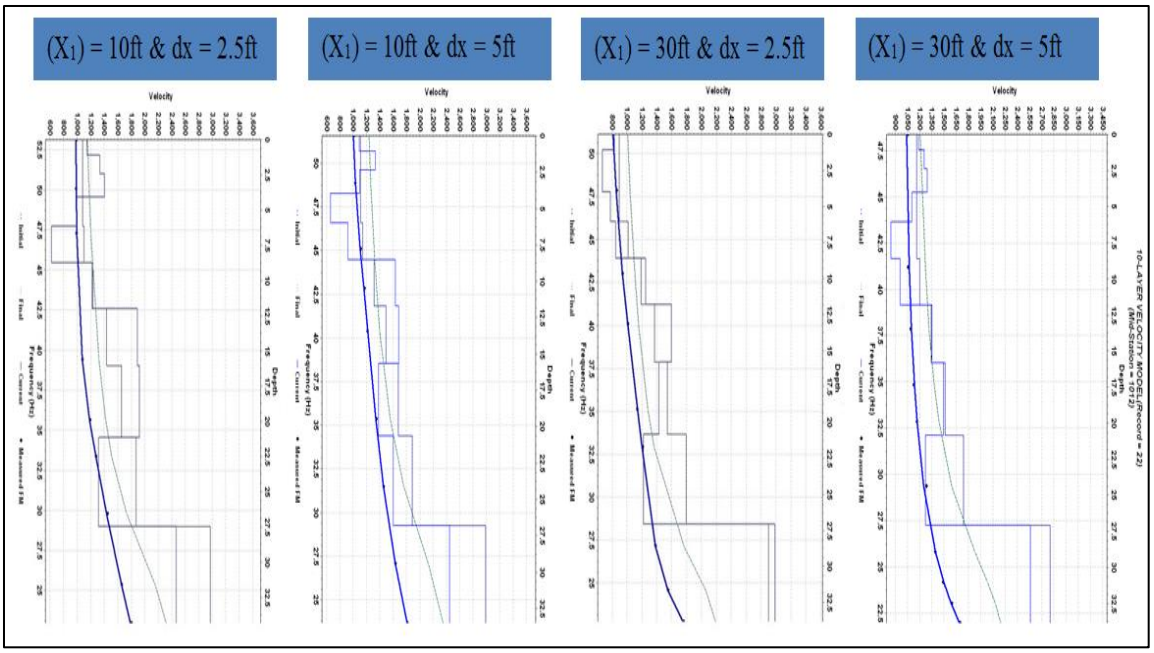

Figure 5.22. Comparison of 1-D shear wave velocity profiles, deduced using the inversion technique from the seismic data sets collected with various configurations of active MASW oriented north to south array.

5.4. QUANTITATIVE ANALYSES

As a first step of quantitative analysis, three criterias were chosen, and include continuity of dispersion curve, maximum depth of investigation, and reliability of the top of rock estimate. The rating categories are briefly summarized in Table 5.4.

Table 5.4. Encoded categories for three criterias.

Sensitivity of Dispersion Curve	Ranking		
Maximum Depth of 1-D shear-wave velocity profiles	≤ 20ft	20 to 30ft	≥ 30ft
	0	5	10
Difference between MASW- and ERT-determined depths to top of bedrock (%)	≤ 20 %	20 to 30 %	≥ 30 %
	10	5	0
Continuity of Dispersion Curve	High	Intermediate	Low
	30	15	0

The continuity was analyzed on the basis of visual assessment of overtone images and dispersion curves. The quality of the acquired surface wave records were evaluated in terms of the resolution of the phase velocity spectrum, i.e., the sharpness of the amplitude peaks observed at each frequency, the extractable frequency range and the continuity of the fundamental mode high-amplitude band. The continuity ratings “Good”, “Fair”, and “Poor” were assigned on the basis of visual assessment of overtone images and dispersion curves, as shown in Fig. 5.23. To ease quantitative data analysis, each rating was encoded numerically. Thus, number 30 was assigned to “good”, number 15 was assigned to “fair”, and number 0 was assigned to “poor”.

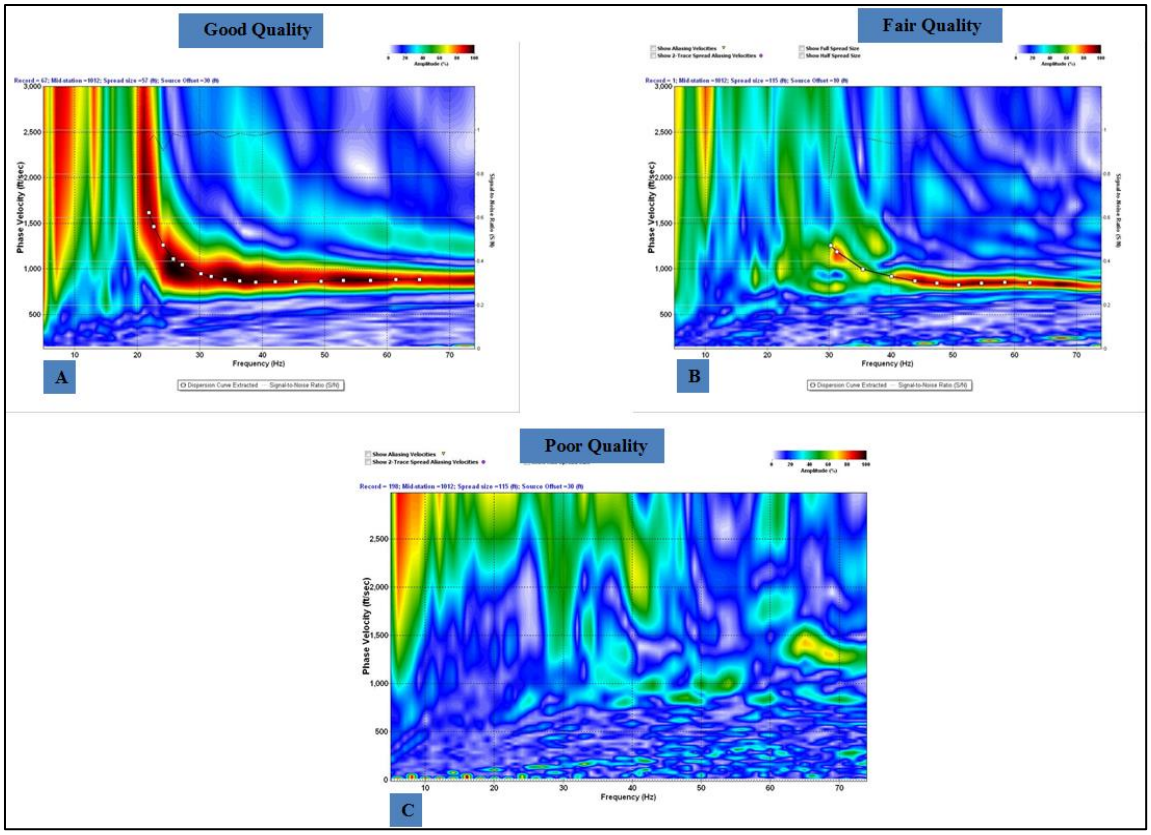

Figure 5.23 Overtone images obtained from MASW data of (A) good quality, (B) fair quality, and (C) poor quality.

Regarding to the maximum depth of MASW profiles, number 0 was assigned to profiles that do not extend to a depth of 20ft., number 5 was assigned to profiles that do extend to a depth of 30ft., and number 10 was assigned to profiles that extend to a depth greater than 30ft.

The analysis of reliability of the top of rock estimate was based on the comparison of ERT- and MASW-determined depth to top of bedrock. The difference between the two was calculated in percent. Number Zero was assigned to profiles that gave the difference more than 30%, number 5 was assigned to profiles that gave the difference in the interval of 20 to 30%, and number of 10 was assigned to profiles that had difference less than 20%.

The quantitative data analysis was performed by summing up the ratings of tree criterias. Thus, a number of 50 is the maximum possible number, and a number of Zero is the minimum number. The data quality categories were developed based on the numbers after summation. The categories are briefly summarized in Table 5.5. Using this approach, all MASW profiles were evaluated in order to assign the data quality ratings.

Table 5.5. Data quality categories.

Categories	Data quality
40 to 50	Good data quality. 1-D shear wave velocity profiles extend to a depth of 30ft.
30 to 39	Fair data quality. 1-D shear wave velocity profiles do not extend to a depth of 30ft.
20 to 29	Poor quality data. 1-D shear wave velocity profiles do not extend to a depth of 20ft.
≤ 20	Severe data quality. No meaningful interpretations.

In an attempt to identify the MASW array configuration that gives the better data quality, statistical analysis was performed. During the analysis, mean values were calculated for each group of MASW array configuration. Table 5.6 summarizes statistics for west to east direction arrays, and Table 5.7 summarizes statistics for north to south direction arrays. As seen in Table 5.6, the highest mean value (30.73) was observed for 10ft. source offset and 2.5ft.geophone spacing array. This implies that this configuration gave the better quality of MASW data. The lowest mean value (21.91) was observed for 30 ft. source offset and 5ft. receiver spacing array. It is interesting to note that according to the statistical analysis, the shortest geophone spread (10 x 2.5ft.) gave the better data quality, whereas the longer geophone spread (30 x 5ft.) gave the poorer quality. This

supports the previous statement about the effect of irregularity of the depth to top of rock along short and long geophone arrays. According to Table 5.7, mean values calculated for configurations direction north to south are slightly higher than those calculated for configurations direction west to east (Table 5.6).

Table 5.6. Quantitative analysis performed for 136 MASW profiles acquired in west to east direction.

Configuration: (source offset) x (receiver spacing) ft.	Sample Size (N)	Mean ($\bar{x}$)	Minimum	Maximum
10 x 2.5	34	30.73	0	50
10 x 5	34	28.52	0	40
30 x 2.5	34	28.38	0	50
30 x 5	34	21.91	0	35

Table 5.7. Quantitative analysis performed for 136 MASW profiles acquired in north to south direction.

Configuration: (source offset) x (receiver spacing) ft.	Sample Size (N)	Mean ($\bar{x}$)	Minimum	Maximum
10 x 2.5	34	32.64	0	50
10 x 5	34	28.38	0	50
30 x 2.5	34	32.79	0	50
30 x 5	34	28.38	0	50

To analyze the frequency of occurrence of MASW profiles with good, fair, poor, and severe quality, Figures 5.24 and 5.25 were generated. Figure 5.24 shows distribution of MASW data acquired by the array oriented in west to east direction and Figure 5.25 shows MASW data acquired by the array oriented in north to south direction. According

to Figure 5.24, the largest number of good quality MASW profiles was acquired using 10ft. source offset and 2.5ft. receiver spacing. In contrast, the smallest number of good quality MASW profiles was acquired by the configuration with 30 ft. source offset and 5ft. receiver spacing.

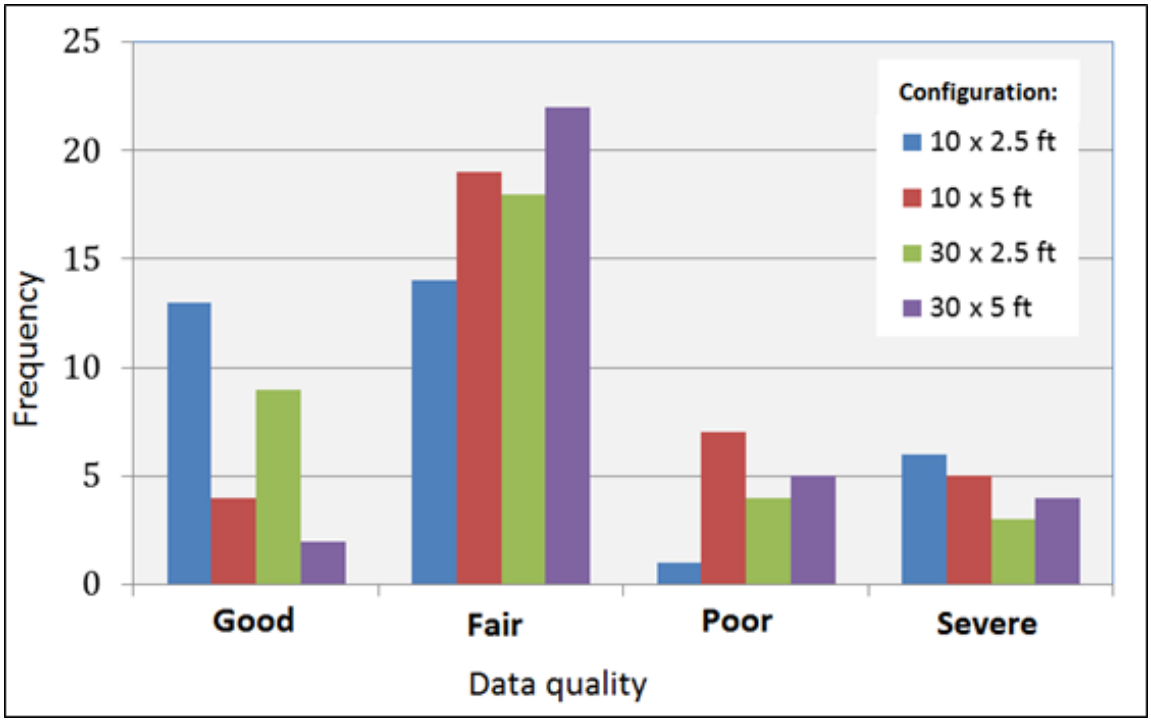

Figure 5.24 Histogram showing how often MASW data of good, fair, poor, and severe quality were acquired using a specific array configuration (west to east direction).

Regarding to the north to south oriented arrays, the largest number of MASW profiles with good data quality was acquired by the 10ft. source offset and 2.5ft. receiver spacing array. It is interesting to note that no MASW profiles with good data quality were acquired using the longest (30 x 5ft.) geophone spread. In contrast, this configuration (30 x 5ft.) gave the largest number of MASW profiles with severe data quality.

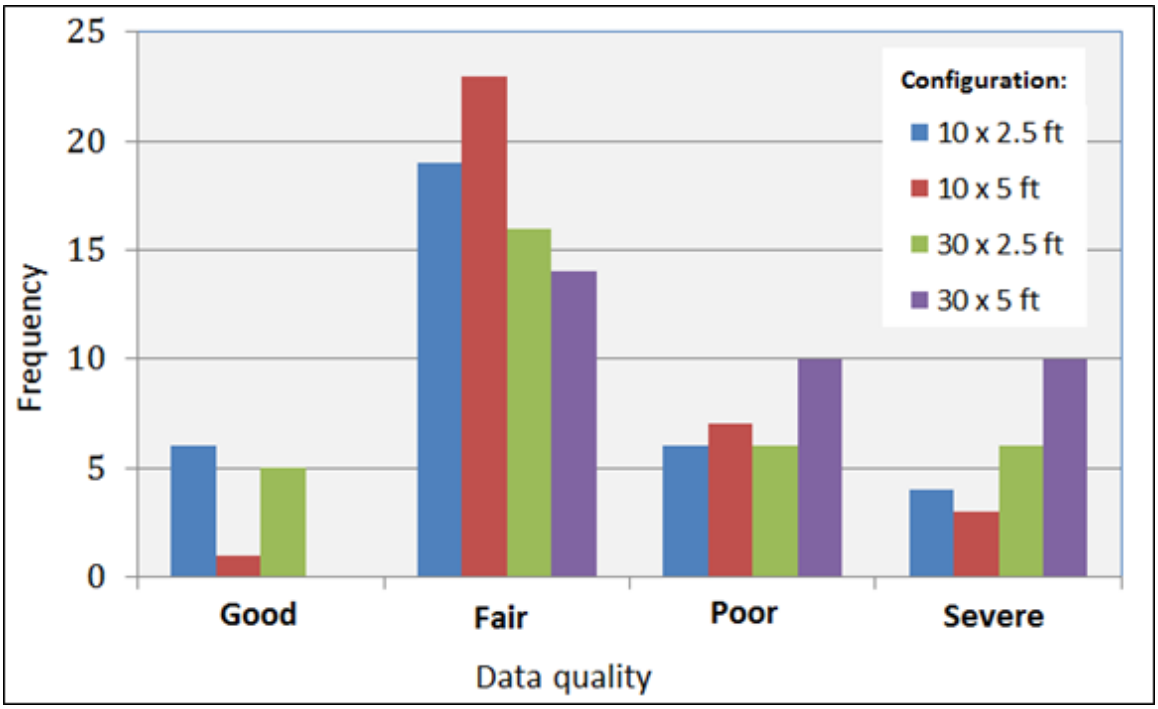

Figure 5.25 Histogram showing how often MASW data of good, fair, poor, and severe quality were acquired using a specific array configuration (north to south direction).

6. CONCLUSIONS

The main goal of this research was to develop optimum MASW configuration that can be used in karst terrain to image subsurface to a depth of 30ft. (9m). To accomplish the goal, MASW data were acquired with different parameters and in different directions. Qualitative and quantitative analyses were performed in this study to assess the performance of each configuration.

The following conclusions can be made on the basis of qualitative analysis:

- Continuity of dispersion curve must be the primary criteria in evaluating MASW data quality. The dispersion is more continuous over a broad range of frequency when MASW data are acquired parallel to the solution widened joints.
- As the solution widened joints trend north to south, MASW data acquired by the north to south oriented arrays are of a better quality.

The following conclusions can be made on the basis of quantitative analysis:

- In addition to the continuity of dispersion curve, two criterias – maximum depth of investigation and reliability to top of rock estimate – can be used to evaluate overall quality of MASW data. Using three criterias, it was determined that MASW data acquired by 10ft. source offset and 2.5ft. receiver spacing array configurations are of a better quality.

7. RECOMMENDATIONS

This research has enhanced the understanding of acquisition of MASW data in karst terrain. However, further studies are still required to improve acquisition, processing and interpretation of seismic data in karst terrain. The following studies are recommended:

- Choice of the method should be guided by the anticipated depth and size of target(s), the nature of the background materials or the maximum depth of rock surrounding the target(s), the reason for delineating the target(s), the desired resolution of the target(s), and the size of the investigation area and the sources of cultural interference in the investigation area.
- The values that are determined for optimum data acquisition and processing should be taken as guidelines for all other parameters (i.e., it is important to choose processing parameters that are appropriate for the depth target of the investigation).
- For impact sources, such as the drop weight or vibrator should be used to enhance the quality of the active MASW data in complex karst terrain.
- A quantitative evaluation of the resolution of surface wave methods should be conducted to clearly delineate the examination capabilities not only for researchers, but as well to associate engineers avoid error application of surface wave methods.
- In addition, calculation efforts should be made to improve the efficiency of intensive inversion algorithms using parallel programming and computing on GPS or GIS.

BIBLIOGRAPHY

Abbiss, C.P. (1981). Shear wave measurements of the elasticity of the ground. Geotechnique, 31, (1), pp91-104.

Advanced Geosciences, Incorporated. "Instruction Manual for the Super Sting with Swift Automatic Resistivity and IP System." Austin, January 2006.

Aki, K., & Richards, P. G. (1980). Quantitative seismology: Theory and methods (Vol. 1). San Francisco, CA: W. H. Freeman and Co.

Anderson, N. (2010). Lectures in: Ground Penetrating Radar Applications in Engineering and Environmental Studies. GE482. Rolla, Missouri, USA: Missouri University of Science and Technology.

Anderson, N., 2012, Determination of Optimum "Multi-Channel Surface Wave Method" Field Parameters: NUTC R292.

Auld, B. A., Acoustic Fields and Waves in Solids (Stanford University Press, 1973). EWING, W.M., JARDETZKY, W. S., and PRESS, F., Elastic Waves in Layered Media (McGraw-Hill, London, 1957), 380 pp.

Bacon, M., Simm, R and Redshaw, T. (2003): 3-D Seismic Interpretation; Cambridge University press.

Baechle, G.T., G.P. Eberli, R.J. Weger, and J.L. Massafero, 2009, Changes in dynamic shear moduli of carbonate rocks with fluid substitution: Geophysics, 74, E135-E147.

Ballard, R.F. & McLean, F.G. 1975. Seismic field methods for in situ moduli. Proc. Conf. on In Situ Measurement of Soil Properties. Spec. Conf. Geotech. Eng. Div., A.S.C.E., Vol 1, pp121-150.

Beaty, K. S., Schmitt, D. R., & Sacchi, M. (2002). Simulated annealing inversion of multimode Rayleigh wave dispersion curves for geological structure. Geophysical Journal International, 151(2), 622-631.

Boore, DM (2004). Estimating VS (30) (or NEHRP Site Classes) from shallow velocity models (depths < 30m), Bull. Seismo. Soc. Am., 94(2):591–597. http://parkseismic.com/SSC-Main.html.

Bolt, B. A. (1976). Nuclear Explosions and Earthquakes: The Parted Vail. San Francisco, CA: W. H. Freeman and Co.

British Geological Survey (c) NERC 2013.

Buettner, M., Ramirez, A. and Daily, W. “Electrical Resistance Tomography for Imaging the Spatial Distribution of Moisture in Pavement Sections” Structural Materials Technology: An NDT Conference, San Diego, Feb. 20-23 1996 [abstract], 1996, 342-347.

Bullen, K.E., 1963, an Introduction to the Theory of Seismology: Cambridge University Press, 381 p.

Cai, Y., Sangghaleh, A., & Pan, E. (April 01, 2015). Effect of anisotropic base/interlayer on the mechanistic responses of layered pavements. Computers and Geotechnics, 65, 2, 250-257.

Chambers, J. E., Wilkinson, P. B., Penn, S., Meldrum, P. I., Kuras, O., Loke, M. H., & Gunn, D. A. (June 01, 2013). River terrace sand and gravel deposit reserve estimation using three-dimensional electrical resistivity tomography for bedrock surface detection. Journal of Applied Geophysics, 93, 1, 25-32.

Choon B. Park, Richard D. Miller, and Hidetoshi Miura (2002). Optimum Field Parameters of an MASW Survey.

Choon B. Park, Richard D. Miller, Jianghai Xia, and Julian Ivanov (2007) “Multichannel Analysis of Surface Waves (MASW)-Active and Passive Methods”. The Leading Edge.

Coskun, N. “The effectiveness of electrical resistivity imaging in sinkhole investigations,” International Journal of Physical Sciences, 7(15), 2398 - 2405.

Coots, T. “Greene County Comprehensive Plan: Greene County Planning and Zoning,” http://www.greenecountymo.org/web/Public_Information/files/Comp.pdf, 2007.

Choon B. Park, Richard D. Miller, and Hidetoshi Miura (2002) “Optimum Field Parameters of an MASW Survey”.

Cornou, C., M. Ohrnberger, D. M. Boore, K. Kudo, and P.-Y. Bard, 2006, Derivation of structural models from ambient vibration array recordings: Results from an international blind test: Proceedings of the 3rd International Symposium on the Effects of Surface Geology on Seismic Motion, paper NBT.

Daniels F. and Alberty R.A., 1966. Physical Chemistry. John Wiley and Sons, Inc. de Groot-Hedlin, C. and Constable, S., 1990. Occam's inversion to generate smooth, two dimensional models form magneto telluric data. Geophysics, 55, 1613-1624.

Dal Moro, G., Pipan, M., Forte, E., & Finetti, I. (2003). Determination of Rayleigh wave dispersion curves for near surface applications in unconsolidated sediments. In SEG International Exposition and Seventy-Third Annual Meeting, 24-31 October 2003, Dallas, Texas (Vol. 22, pp. 1247–1250).

Dey A. and Morrison H.F. Resistivity modeling for arbitrary shaped two-dimensional structures. Geophysical Prospecting 27, 1979, 106-136.

Denizman, C., 2003, Morphometric and spatial distribution parameters of karstic depressions, lower Suwannee River basin, Florida: Journal of Cave and Karst Studies, 65, 29-35.

Donohue, S., Forristal, D., & Donohue, L. A. (2013). Detection of soil compaction using seismic surface waves. Soil and Tillage Research, 128, 54–60.

Doolittle, J.A., and M.E. Collins, 1998, Comparison of EM induction and GPR methods in areas of karst: Geoderma, 85, 83-102.

Duffy, B.G., 2008, Development of multichannel analysis of surface waves (MASW) for characterizing the internal structure of active fault zones as a predictive method of identifying to distribution of ground deformation, M.Sc. Thesis, University of Canterbury.

Elkrry, A., Nwokebuihe, S., Torgashov, E., Dera, A., Alotaibi, A., Anderson, N. (2015). Site Specific Pavement Condition Assessment. EEGS SAGEEP 28 (Environmental and Engineering Geophysical Society, the Symposium on the Application of Geophysics to Engineering and Environmental Problems). Austin, TX. March, 2015.

Everett, M. E. (2013). Near-Surface Applied Geophysics. Cambridge: Cambridge University Press.

Fellow, L. D., "Geology of Galloway Quadrangle Greene County Missouri," Missouri Geological Survey and Water Resources, 1970.

Forbriger, T., 2003a, Inversion of shallow-seismic wavefields: I. Wavefield transformation: Geophys. J. Int., 153, 720-734.

Foti, S. (2000). Multistation methods for geotechnical characterisation using surface waves. Ph.D. Thesis, Politecnico di Torino. 229p.

Gazetas, G. 1982. Vibrational characteristics of soil deposits with variable velocity. Int. Jour. Numerical and Analytical Methods in Geomech., Vol 6, pp 1-20.

Gibson, Paul J, and Dorothy M George. Environmental Applications of Geophysical Surveying Techniques. Hauppauge: Nova Science Publishers, 2003.

Gucunski, N., Woods, R.D., 1991. Instrumentation for SASW testing. In: Bhatia, S.K., Blaney, G.W. (Eds.), Recent Advances in Instrumentation, Data Acquisition and Testing in Soil Dynamics, Geotechnical Special Publication, vol. 29. American Society of Civil Engineers, pp. 1– 16.

Heisey, J. S., Stokoe II, K. H., Hudson, W. R., and Meyer, A. H. (1982), Determination of in situ Shearwave Velocity from Spectral Analysis of Surface Waves, Research Report No. 256-2, Center for Transportation Research. The University of Texas at Austin, December, 277 pp.

Ivanov, J., Park, C. B., et al. (2001). Modal separation before dispersion curve extraction by MASW method. SAGEEP Denver, Colorado.

Ivanov, J., Park, C. B., et al. (2005). "Analyzing and filtering surface wave energy by muting shot gathers." Journal of Environmental and Engineering Geophysics 10: 307-322.

Ivanov, J., R.D. Miller, P. Lacombe, C.D. Johnson, and J.W. Jr. Lane, 2006, Delineating a shallow fault zone and dipping bedrock strata using multichannel analysis of surface waves with a land streamer, Geophysics, 71, 5, p. A39-A42. doi: 10.1190/1.2227521.

Ivanov, Julian, Choon Park, and Jianghai Xia. "MASW/Surfseis 2 Workshop." Fort Worth: Kansas Geologic Survey, March 28, 2009.

Ivanov, J., R.D. Miller, S. Peterie, C. Zeng., J. Xia, and T. Schwenk, 2011, Multi-channel analysis of surface MASW (MASW) of models with high shear-wave velocity contrast, 2011 SEG Annual Meeting, September 18 - 23, 2011 , San Antonio, Texas.

Jones, R.B. 1958 In-situ measurement of the dynamic properties of soil by vibration methods. Geotechnique, vol. 8 (1), pp. 1-21.

Kearey, Philip, Micheal Brooks, and Ian Hill. An Introduction to Geophysical Exploration. Williston: Blackwell Publishing, 2002.

Kansas Geological Survey “Multichannel Analysis of Surface Waves”, 2013 http:/www.masw.com/index.html

Keller G.V. and Frischknecht F.C., 1966. Electrical methods in geophysical prospecting. Pergamon Press Inc., Oxford.

Kramer, S. L. (1996). Geotechnical Earthquake Engineering. Upper Saddle River, NJ: Prentice-Hall.

Lin, C.-P., Chang, C.-C., & Chang, T.-S. (2004), the use of MASW method in the assessment of soil liquefaction potential. Soil Dynamics and Earthquake Engineering, 24 (9–10), 689–698.

Loke, M.H., "Electrical imaging surveys for environmental and engineering studies," in http://www.abem.se/support/downloads/case-studies/practical-guide-to-2d-3dsurveys. 1999.

Loke, M.H. "Electrical Imaging Survey for Environmental and Engineering Studies." 2000.

Loke, M.H., 2011. Electrical resistivity surveys and data interpretation, in Gupta, H (ed.), Solid Earth Geophysics Encyclopaedia (2nd Edition) "Electrical & Electromagnetic" Springer-Verlag, 276-283.

Macfarlane, P.A., Healey, J.M., and Wilson, B.W., 2005 THE SOUTHEAST KANSAS OZARK AQUIFER WATER SUPPLY PROGRAM PHASE 1 PROJECT RESULTS, Kansas Geological Survey Open File Report 2005-15 15p. (http://www.kgs.ku.edu/Hydro/Publications/2005/OFR05_15/aquifer.pdf. (Date accessed: May 13, 2008).

Miller, R.D., Xia, J., and Park, C.B., 1999, Estimation of near-surface shear-wave velocity by inversion of Rayleigh waves: Geophysics, v. 64, no. 3, p. 691-700. (XIA-99-04)

Miller, R., Xia, J., Park, C., Davis, J., Shefchik, W., and Moore, L., 1999a, Seismic techniques to delineate dissolution features in the upper 1000 ft at a power plant; Technical Program with biographies, SEG, 69th Annual Meeting, Houston, Texas, 492-495.

Miller, R., Xia, J., Park, C., Ivanov, J., and Williams, E., 1999b, Using MASW to map bedrock in Olathe, Kansas; Technical Program with biographies, SEG, 69th Annual Meeting, Houston, Texas, 874-877.

Miller, R.D., J. Xia, and C.B. Park, 2005, Seismic techniques to detect dissolution features (karst) at a proposed power-plant site, in, D.K. Butler, ed., near surface geophysics: Society of Exploration Geophysicists, 663-679.

Milson, John. Field Geophysics. New York: John Wiley & Sons, 1996.

Missouri Department of Conservation 2005. Wildlife Code of Missouri, Rules of the Conservation Commission. Issued March 1, 2005. Missouri Department of Conservation, Jefferson City, MO.

Monroe, Watson H. A Glossary Karst Terminology. Geological Survey Water Paper 1899-K, 1970.

Muchaidze, I., “Imaging Karst Terrain Using Electrical Resistivity Tomography.” In https://mospace.umsystem.edu/xmlui/bitstream/handle/10355/26344/Muchaidze_2008. Pdf? Sequence =1. 2008.

Muchaidze, I., 2009, Imaging in Karst Terrain Using Electrical Resistivity Tomography. Master’s Thesis, Missouri Science and Technology University, 2009.

Myat, M., Wamweya, A., Kovin, O., Anderson, N., and Robison, J., 2008a, Application of Electrical Resistivity Method in Steeply Dipping Karst Terrain: 11th Multidisciplinary Conference on Sinkholes and the Engineering and Environmental Impacts of Karst: Integrating Science and Engineering to Solve Karst Problems, September 22-26, 2008, Ramada Conference Center Tallahassee, Tallahassee, FL. 224.

Myat, M., Muchaidze, Y., Wamweya, A., Anderson, N., and Robison, J., 2008b, Assessment of Karst Activity at Springfield Route 60 Study Site: 11th Multidisciplinary Conference on Sinkholes and the Engineering and Environmental Impacts of Karst: Integrating Science and Engineering to Solve

Nakano, M., Fuji, K., and Takeuchi, S. (1988), Rayleigh wave scatteringat wedge corners with major wedge angles. In Scattering and Attenuation of Seismic Waves, Part I (eds. Aki, K. and Wu R. S.), Pure Appl. Geophys. 128, 119–132.

Neidell, N.S., and Taner, M.T., 1971, Semblance and other coherency measures for multichannel data: Geophysics, 36, 482–497.

Odum, J.K., R.A. Williams, W.J. Stephenson, D.M. Worley, C. von Hillebrandt-Andrade, E. Asencio, H. Irizarry, and A. Cameron, 2007, Near-surface shear wave velocity versus depth profiles, Vs 30, and NEHRP classifications for 27 sites in Puerto Rico: USGS Open-File Report 2007-1174.

Okada, H. 2003. The microtremor survey method. Geophysical Monograph Series. No. 12. Society of Exploration Geophysicists, Tulsa, Oklahoma, USA.

O’Neill, A., 2003, Full-waveform reflectivity for modeling, inversion and appraisal of seismic surface wave dispersion in shallow site investigations, Ph.D. thesis, The University of Western Australia, Australia.

Park, C.B., Miller, R.D., and Xia, J., 1997, Multi-channel analysis of surface waves (MASW) “A summary report of technical aspects, experimental results, and perspective”: Kansas Geological Survey Open-file Report 97-10.

Park, C. B., R. D. Miller, and J. Xia, 1998, imaging dispersion curves of surface waves on multi-channel record: 68th Annual International Meeting, SEG, Expanded Abstracts, 1377–1380.

Park, C.B., XIA, J. and Miller, R.D. (1998b) Imaging dispersion curves of surface waves on multichannel record: 68th Ann.

Park, C.B., R.D. Miller, and J. Xia, 1999, Multichannel Analysis of Surface Waves: Geophysics, 64, 800-808.

Park, C.B., Miller, R.D., and Xia, J., 1999a, Multi-channel analysis of surface waves: Geophysics, 64(3), 800-808.

Park, C.B., Miller, R.D., and Xia, J., 1999b, Detection of near-surface voids using surface wave: Proceedings of the Symposium on the Application of Geophysics to Engineering and Environmental Problems (SAGEEP 99), Oakland, CA, March 14-8, 281-286.

Park, C.B., R.D. Miller, and J. Xia, 2000, Detection of higher mode surface waves over unconsolidated sediments by the MASW method: Proceedings of the Symposium on the Application of Geophysics to Engineering and Environmental Problems (SAGEEP 2000), Arlington, Va., February 20-24, p. 1-9. (PAR-00-01).

Park, Choon B, Richard D Miller, Jianghai Xia, and Julian Ivanov. "Multichannel Seismic Surface-Wave Methods for Geotechnical Applications." First International Conference on the Application of Geophysical Methodologies to Transportation Facilities and Infrastructure. St. Louis, 2000.

Park, C. B., Miller, R. D., & Xia, J. (2001). Offset and resolution of dispersion curve in multichannel analysis of surface waves (MASW). In Proceedings of the Symposium on the Application of Geophysics to Engineering and Environmental Problems 2001 (p. SSM4). Denver, CO: Environment and Engineering Geophysical Society.

Park, C.B., Miller, R.D., and Miura, H., 2002, Optimum field parameters of an MASW survey [Exp. Abs.]: SEG-J, Tokyo, May 22-23, 2002. (PAR-02-03).

Park, Choon B. MASW - Horizontal Resolution in 2D Shear-Velocity (Vs) Mapping. Open-File Report, Lawrence: Kansas Geologic Survey, 2005.

Park, C. B., Miller, R. D., Ryden, N., Xia, J., and Ivanov, J., 2005, Combined use of active and passive surface waves: Journal of Engineering and Environmental Geophysics (JEEG), 10, (3), 323-334.

Park, C. B., Miller, R. D., Xia, J., & Ivanov, J. (2007). Multichannel analysis of surface waves (MASW) active and passive methods. The Leading Edge, 26 (1), 60–64.

Park, C. B., & Shawver, J. B. (2009). MASW Survey Using Multiple Sources Offsets. In D. K. Butler (Ed.), Proceedings of the Symposium on the Application of Geophysics to Engineering and Environmental Problems 2009 (pp. 15–19). Denver, CO: Environment and Engineering Geophysical Society.

Park, C. B., & Carnevale, M. (2010). Optimum MASW survey—Revisit after a Decade of Use. In D. O. Fratta, A. J. Puppala, & B. Muhunthan (Eds.), GeoFlorida 2010: Advances in Analysis, Modeling & Design (pp. 1303–1312). Reston, VA: American Society of Civil Engineers.

Park, C., 2013, MASW for geotechnical site investigation: The Leading Edge, June 2013, v. 32, p. 656-662.

Park, C. B. (2015). Data acquisition. Retrieved 23 June, 2015, from http://www.masw.com/DataAcquisition.html.

Press, F., 1966, Seismic velocities: in Handbook of physical constants, revised edition, Clark, S.P., Jr. (ed.), Geological Society of America Memoir, 97, 97–173.

Richart, F. E., Hall, J. R., and Woods, R. D., 1970, Vibrations of soils and foundations: Prentice-Hall, Inc.

Rix, G.J., and Leipski, A.E., 1991, Accuracy and resolution of surface wave inversion: Recent Advances in Instrumentation, Data Acquisition and Testing in Soil Dynamics: Geotechnical Special Publication No. 29, ASCE, 17-23.

Robinson, E.S. & Çoruh, C. (1988) Basic Exploration Geophysics. Wiley, New York.

Robison, J. and Anderson, N., Geophysical Investigation of the Delaware Avenue Sinkhole, Nixa, Missouri: 11th Multidisciplinary Conference on Sinkholes and the Engineering and Environmental Impacts of Karst: Integrating Science and Engineering to Solve Karst Problems, September 22-26, 2008, Ramada Conference Center Tallahassee, Tallahassee, FL, 2008.

Rosenblad, B. L. and Cheng- Hsuan, L. (2011). Influence of Poisson's Ratio on Surface Wave Near- Field Effects. Geo- Frontiers 2011: Advances in Geotechnical Engineering, ASCE.

Ryden, N. and Mooney, M. (2009). Analysis of surface waves from the light weight deflectometer: Soil Dynamics and Earthquake Engineering, 29: 1134-1142.

Rene P, Maros N, Ivan D, David K (2012) “Determination of Cavities Using Electrical Resistivity Tomography”. Contributions to Geophysics and Geodesy, 42:201-211.

Socco, L.V., and Strobia, C., 2004, Surface-wave method for near-surface characterization: a tutorial: Near Surface Geophysics, 2, 165-185.

Socco, L. V., Foti, S., & Boiero, D. (2010). Surface-wave analysis for building near-surface velocity models - Established approaches and new perspectives. Geophysics, 75 (5), 75A83–75A102.

Stokoe II KH, Wright GW, James AB, Jose MR. Characterization of geotechnical sites by SASW method. In: Woods RD, Ed. Geophysical characterization of sites, A. A. Balkema/Rotterdam, 1994. p. 15-25.

Shade, K.A., 2003, Temporal analysis of floodplain deposition using urban pollution 153 stratigraphy, Wilson Creek, SW Missouri. Masters of Science Thesis, Department of Geography, Geology, and Planning, Southwest Missouri State University, Springfield, Missouri.

Silvester, P.P. and Ferrari R.L. Finite elements for electrical engmeers. 2nd. ed. Cambridge University Press, 1990.

Sudha, K., M., Mittal, S., & Rai, J. (January 01, 2009). Soil characterization using electrical resistivity tomography and geotechnical investigations. Journal of Applied Geophysics, 67, 1, 74-79.

Sheriff, R. E., & Geldart, L. P. (1995): Exploration Seismology, Cambridge University Press.

Shishay T. Kidanu, Evgeniy V. Torgashov, Aleksandra V. Varnavina, Neil L. Anderson (May 23, 2016). ERT-based Investigation of a Sinkhole in Greene County, Missouri. Journal of Geosciences, 2 (2): 99-115.

Schrott, L. and O. Sass, 2008, Application of field geophysics in geomorphology: Advances and limitations exemplified by case studies: Geomorphology, 93, 55-73.

Shuang X, Lung, and Jianghal (2004). The Selection of Field Acquisition Parameters for Dispersion Images from Multichannel Surface Wave Data: Pure and Applied Geophysics, 161 (2004) 185–201.

Steeples, Don. "Near-Surface Seismology: A Short Course." Lawrence: Society of Exploration Geophysicist, 1998.

Steeples, D. W., Baker, G. S., Schmeissner, C., 1999. Toward the Autojuggie: Planting 72 Geophones in 2 Sec. Geophysical Research Letters, 26(8): 1085–1088.

Surf-Seis. Multi-Channel Analysis of Surface Waves. 2006. Retrieved February 3, 2010 from: http://www.kgs.ku.edu/software/surfseis/masw.html. Steeples, Don. "Near-Surface Seismology: A Short Course." Lawrence: Society of Exploration Geophysicist, 1998.

Telford, W.M., Geldart, L.P., and Sheriff, R.E., 1990, Applied Geophysics, second edition: Cambridge, Cambridge University Press, 770 p.

Tian, G. (April 01, 2003). Multichannel analysis of surface wave method with the autojuggie. Soil Dynamics and Earthquake Engineering, 23, 3, 61-65.

Torgashov, E., Anderson, N., Li, M., Ismail, A., & Elkrry, A. (2012). Imaging in Karst Terrain Using Electrical Resistivity Tomography and Subsurface Wave Method; EEGS SAGEEP 25 (Environmental and Engineering Geophysical Society, the Symposium on the Application of Geophysics to Engineering and Environmental Problems. Tucson, AZ, 2012.

Tseng, Y. H., Kang, S. C., Chang, J. R., & Lee, C. H. (December 01, 2011). Strategies for autonomous robots to inspect pavement distresses. Automation in Construction, 20, 8, 1156-1172.

Thierry, P., N. Debeblia, and A. Bitri, 2005, Geophysical and Geological characterization of karst hazards in urban environments: application to Orleans (France): Bulletin of Engineering Geology and the Environment, 64, 139-150.

Unklesbay, A.G. and Jerry D. Vineyard. Missouri Geology: Three Billion Years of Volcanoes, Seas, Sediments, and Erosion. University of Missouri Press Columbia and London, 1992.

United States Corps of Engineers. "EM 1110-1-1802: Geophysical Exploration for Engineering and Environmental Investigations." Engineering Manual, Washington D.C., 1995.

United States Corps of Engineers. "Geotechnical Investigations." Engineering Manual No. 1110-1-1804, Washington D.C., 2001.

Vandike, James E., 1993, Groundwater Level Data for Missouri, Water Year 1991-1992: Missouri Division of Geology and Land Survey, Water Resources Report No. 42, 96 p.

Vandike, James. Karst in Missouri, an Overview. Part 1. Missouri Department of Natural Resources, 1997.

Veni, G., DuChene, H., Crawford, N.C., Groves, C.G., Huppert, G.H., Kastning, E.H., Olson, R. & Wheeler, B.J., 2001, Living with karst: a fragile foundation. Environmental awareness series, American Geological Institute, 64 pp. + 1 pl.

Veni, George. Revising the karst map of the United States. Journal of Cave and Karst Studies 64(1), 45-50, 2001.

Wadati, K. (1933). On the Travel Time of Earthquake Waves, Part II. Geophysical Magazine, 7, 101–111.

What is Karst? http://water.usgs.gov/ogw/karst/pages/whatiskarst, 2012.

Xia, J., R.D. Miller, and C.B. Park, 1998, Construction of vertical seismic section of near-surface shear wave velocity from ground roll [Exp. Abs.]: Soc. Explor. Geophys./AEGE/CPS, Beijing, 29-33.

Xia, J., Miller, R.D., and Park, C.B., 1999, Estimation of near-surface shear-wave velocity by inversion of Rayleigh wave: Geophysics, 64, 691-700.

Xia, J., Miller, R.D., and Park, C.B., 2000a, Advantage of calculating shear-wave velocity from surface waves with higher modes: Technical Program with Biographies, SEG, 70th Annual Meeting, Calgary, Canada, 1295-1298.

Xia, J., Miller, R.D., Park, C.B., Hunter, J.A., and Harris, J.B., 2000b, Comparing shear-wave velocity profiles from MASW technique with borehole measurements in unconsolidated sediments of the Fraser River Delta: Journal of Environmental and Engineering Geophysics, v. 5, no. 3, 1-13.

Xia, J., Miller, R. D., Park, C. B., Hunter, J. A., Harris, J. B., & Ivanov, J. (2002). Comparing shear-wave velocity profiles inverted from multichannel surface wave with borehole measurements. Soil Dynamics and Earthquake Engineering, 22 (3), 181–190.

Xia, J., Miller, R. D., Park, C. B., & Tian, G. (2003). Inversion of high frequency surface waves with fundamental and higher modes. Journal of Applied Geophysics, 52 (1), 45–57.

Xia, J., Chen, C., Li, P.H., and Lewis, M.J., 2004a, Delineation of a collapse feature in a noisy environment using a multichannel surface wave technique: Geotechnique, 54(1), 17-27.

Xia, J. (2014). Estimation of near-surface shear-wave velocities and quality factors using multichannel analysis of surface-wave methods. Journal of Applied Geophysics, 103, 140–151.

Xu, Y., J. Xia, and R. D. Miller, 2006, Quantitative estimation of minimum offset for multichannel surface-wave survey with actively exciting source: Journal of Applied Geophysics, 59, 117–125.

Yuan, D., & Nazarian, S. (1993). Automated Surface Wave Method: Inversion Technique. Journal of Geotechnical Engineering, 119 (7), 1112–1126.

Yilmaz, Ö. (1987). Seismic Data Processing. Tulsa, OK: Society of Exploration Geophysicists.

Yoon, S. and Rix, G.J. (2009). Near-field effects on array-based surface wave methods with active sources: J. Geotech. Geoenviron. Eng., 135(3), 399-406.

Yixian Xu a, Jianghai Xia b, Richard D. Miller (2006). Quantitative estimation of minimum offset for multichannel surface-wave survey with actively exciting source. Journal of Applied Geophysics 59 (2006) 117–125.

Zeng, C., Xia, J., Miller, R. D., Tsoflias, G. P., & Wang, Z. (2012). Numerical investigation of MASW applications in presence of surface topography. Journal of Applied Geophysics, 84, 52–60.

Zhang, S. X., & Chan, L. S. (2003). Possible effects of misidentified mode number on Rayleigh wave inversion. Journal of Applied Geophysics, 53 (1), 17–29.

Zhang, S.X., Chan, L.S., and Xia, J. (2004). The selection of field acquisition parameters for dispersion images from multichannel surface wave data: Pure and Applied Geophysics, 161: 1–17.

Zhou W, Beck BF, Stephenson JB (1999), "Investigation of ground water flow in karst areas using component separation natural potential measurements". Journal of Environmental Geology, 37: 19-25.

VITA

Ghassan Alsulaimani was born in 1976, in Taif city, Saudi Arabia. Mr. Alsulaimani began his collegiate studies in 1994 and received a Bachelor of Science in Geological Engineering in 1998 from King Abdul-Aziz University (KAU) in Saudi Arabia. He has worked for the Saudi Geological Survey since 1999 as an Engineer Geologist. Meanwhile, he was involved in some projects related in the exploration of industrial minerals and rocks. He also worked in the geohazard department for more than four years on a project involving the stability analysis of rock slopes and rock falls.

In May 2014 he received his Master of Science from the Geological Engineering from Missouri University of Science and Technology. Mr. Alsulaimani started the Ph.D. program in Geological Engineering with an emphasis in Geophysics at Missouri University of Science and Technology during the fall semester of 2014.

During his Ph.D. program, Mr. Alsulaimani worked as a research assistant. He has been involved in several subsurface shallow geophysical projects. The geophysical methods he has used include resistivity, seismic, electromagnetic, GPR, and metal detector. Ghassan is interested in shallow-applied geophysics. He has presented at a number of conferences as a primary author and as a co-author, and he has published two scientific papers. He has also been involved in professional societies such as SEG, GSA, AEG, EEGS and SCE. Mr. Alsulaimani has held several elected positions in student organizations at Missouri University of Science and Technology, including vice president of the Saudi Student Association (SSA) in 2013-2016, and ICRM in 2014.

In May 2017 Mr. Alsulaimani received his Ph.D. in Geological Engineering from Missouri University of Science and Technology.